Supporting information

Halide-triggered assembly and selective bisulfate recognition in a quadruply interlocked coordination cage

Jemma I. Virtue, Steven Tsoukatos, Martin R. Johnston, and Witold M. Bloch*

Institute for Nanoscale Science and Technology, College of Science and Engineering, Flinders University, Bedford Park, South Australia, 5042, Australia.

Table of contents

1. Experimental section

1.2. Materials and measurements

Unless otherwise stated, all chemicals were obtained from commercial sources and used as received. Electrospray ionization (ESI) mass spectra were recorded on an Agilent 6230 TOF LCMS. Infrared spectra were collected on a Perkin-Elmer Spectrum 100 using a UATR sampling accessory.

NMR spectra were recorded using an Agilent 500MHz or Bruker UltraShield Avance III 600 MHz NMR spectrometer. Residual solvent peaks were used as an internal reference for ^{1}H NMR spectra [CD_3CN δ 1.94 ppm and DMSO-d_6 δ 2.50 ppm] and ^{13}C NMR spectra [CD_3CN δ 118.26 ppm, DMSO-d_6 δ 39.52 ppm]. Coupling constants (J) are quoted to the nearest 0.1 Hz. The following abbreviations, or combinations thereof, were used to describe ^{1}H NMR multiplicities: s = singlet, d = doublet, t = triplet, q = quartet, m = multiplet, ap. = apparent, br. = broad). ESI-MS was performed on an Agilent HRMS Mass Spectrometer or a Waters Synapt HDMS.

*1.2.1. Synthesis of bis(4-(pyridin-3-ylethynyl)-1H-pyrazol-1-yl)methane (**L**)*

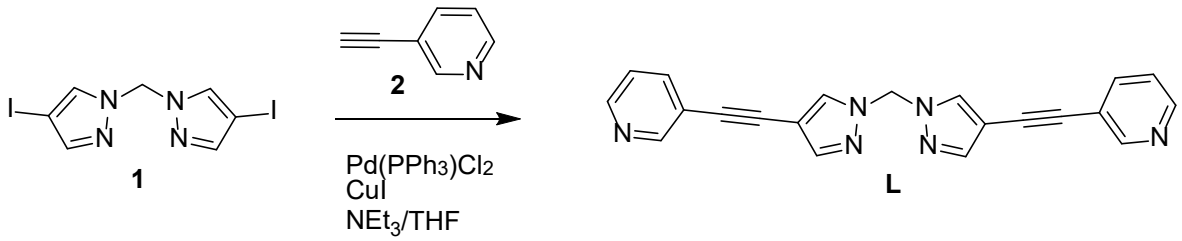

Scheme 1

Bis(4-iodo-1H-pyrazol-1-yl)methane (2.01 g, 5.03 mmol) and 3-ethynylpyridine (1.56 g, 15.13 mmol) were combined in triethylamine (22 mL) and tetrahydrofuran (35 mL). After the mixture was degassed with argon (30 mins), $Pd(PPh_3)_2Cl_2$ (0.070 g, 0.10 mmol, 0.02 equiv.) and CuI (0.010 g, 0.053 mmol, 0.01 equiv.) were added. The mixture was further degassed for 30 minutes and then heated at 75 °C for 18 h. Upon cooling to room temperature, a precipitate formed and was collected by vacuum filtration and washed with ethyl acetate. The crude product was dissolved in chloroform, (30 mL) and washed with water (3 x 30 mL) and brine (1 x 30 mL), then dried over $MgSO_4$. The solvent was removed under reduced pressure to afford **L** as a pale-yellow powder (0.70 g, 40%). ν_{max} (neat, cm^{-1}): 3118 (w), 3082 (m), 3019 (m), 1587 (m), 1566 (m), 1553 (m), 1474 (s), 1415 (s); ^{1}H NMR (500 MHz, CD_3CN): δ 8.67 (s, 1H), 8.52 (d, J = 4.9 Hz, 1H), 8.07 (s, 1H), 7.82 (d, J = 7.9 Hz, 1H), 7.70 (s, 1H), 7.35 (dd, J = 7.9, 4.9 Hz, 1H), 6.30 (s, 2H); ^{13}C NMR (150 MHz, DMSO-d6) δ 151.3, 148.7, 142.8, 138.2, 134.3, 123.7, 119.7, 102.4, 86.9, 83.94, 64.5; ESI-MS: $C_{21}H_{14}N_6$ $[M+H]^+$ calc. 351.1362; found: 351.1352.

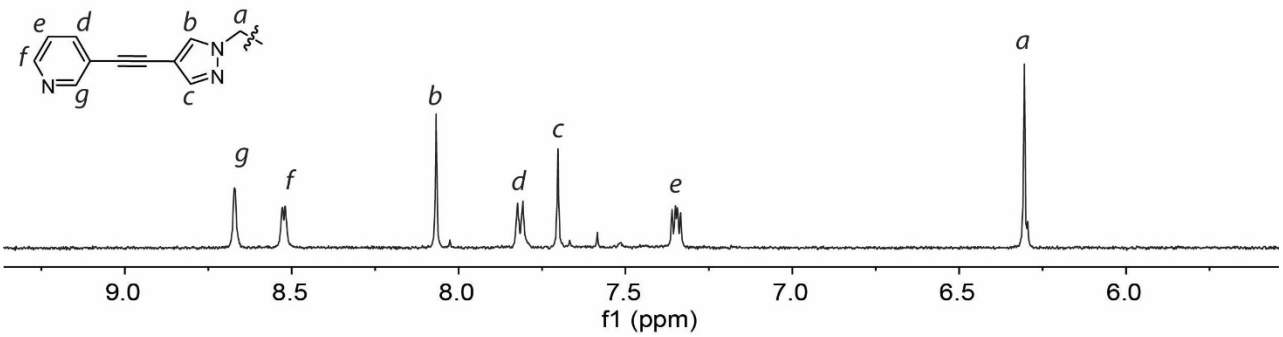

Figure S1. ^{1}H NMR spectrum (400 MHz, CD_3CN, 25 °C) of **L**.

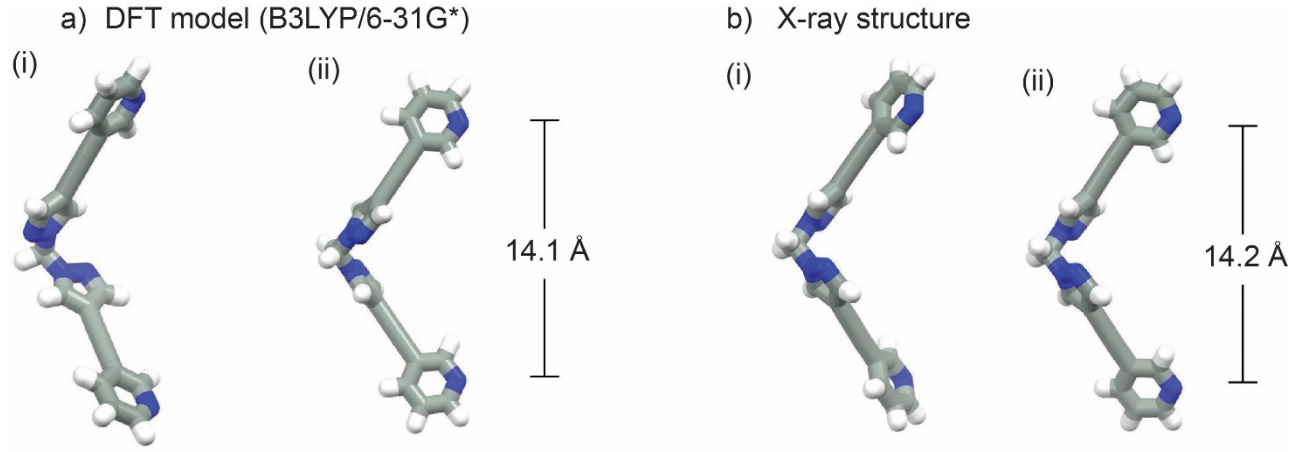

Figure S2. a) DFT model of **L** (i) energy minimized structure; (ii) the same model with pyridine ring rotated manually to be as close to co-planar as possible; b) X-ray structure of **L** (i) X-ray structure; (ii) the same structure with pyridine rings rotated manually to be as close to co-planar as possible. Distance between pyridine nitrogen donors is shown.

*1.2.2. Assembly of the monomeric cage **1** in CD_3CN*

A solution of $[Pd(CH_3CN)_4(BF_4)_2]$ (0.476 mL, 15 mM/CD_3CN, 7.13 µmol) was combined with a hot solution of **L** (5 mg, 14.27 µmol) in CD_3CN (4.62 mL) and continued to heat at 70 °C for 5 minutes to afford **1**. The cage crystallizes in CD_3CN over 72 hours. ^{1}H NMR (500 MHz/CD_3CN): δ 6.31 (s, 8H, CH_2), 7.55 (dd, 8H), 7.74 (s, 8H), 8.03 (dt, 8H), 8.13 (s, 8H), 8.74 (dd, 8H), 8.86 (s, 8H).

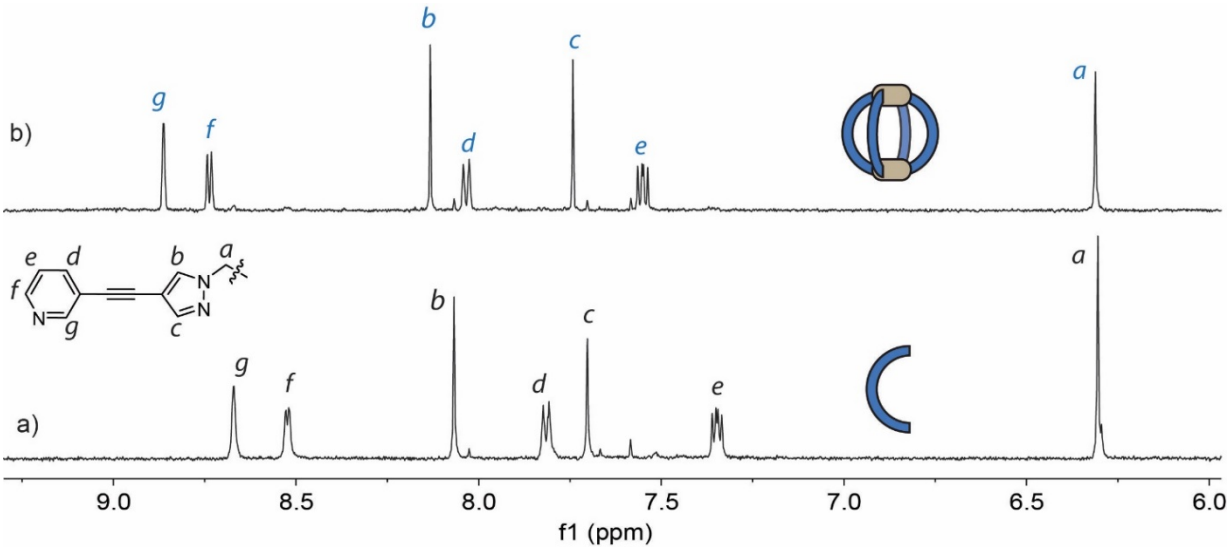

Figure S3. ^{1}H NMR spectrum (500 MHz, CD_3CN, 25 °C) of a) **L**; b) **1.**

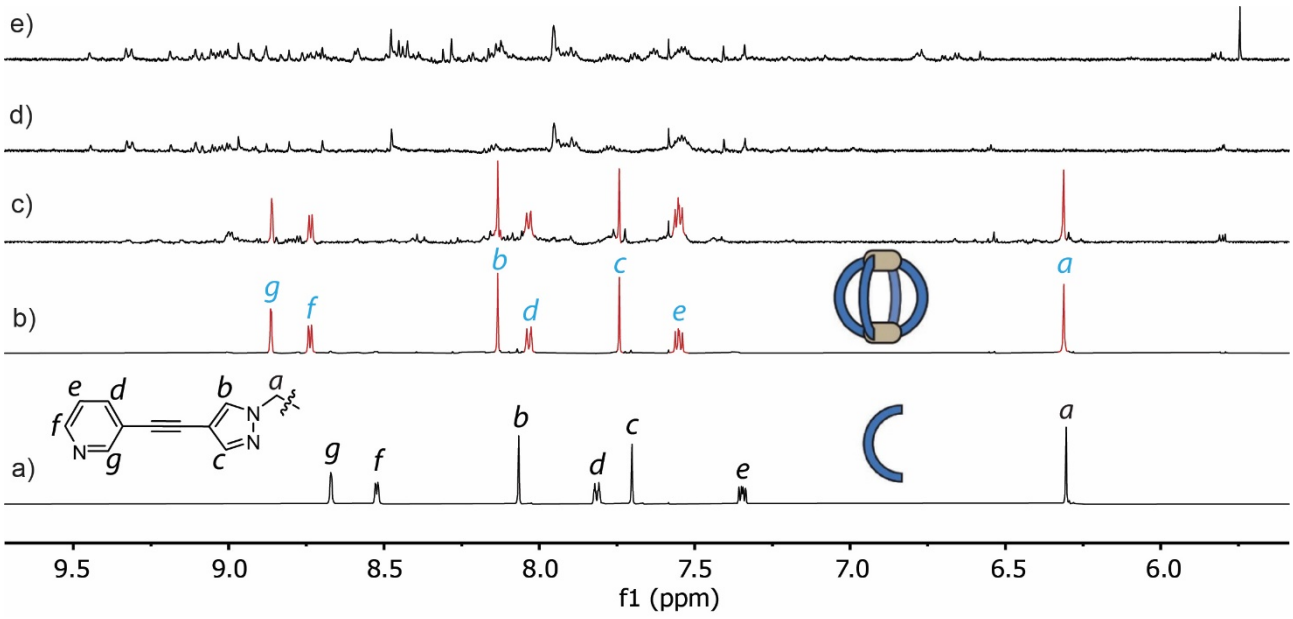

Figure S4. ^{1}H NMR spectra (600 MHz, CD_3CN, 25 °C) of a) **L**; b) **1**; C) **1** + 3 equivalents of $[Pd(CH_3CN)_4](BF_4)_2$, heated at 70 °C for 5 min; d) **1** + 4 equivalents of $[Pd(CH_3CN)_4](BF_4)_2$, heated at 70 °C for 5 min; e) **1** + 6 equivalents of $[Pd(CH_3CN)_4](BF_4)_2$, heated at 70 °C for 5 min.

*1.2.3. Assembly of the monomeric cage **1** in DMSO*

A solution of $[Pd(CH_3CN)_4(BF_4)_2]$ (0.476 mL, 15 mM/DMSO, 7.13 µmol) was combined with a solution of **L** (5 mg, 14.27 µmol) in DMSO-d_6 (4.62 mL) at room temperature to afford **1**. ^{1}H NMR (500 MHz/DMSO-d_6): δ 9.32 (d, J = 1.9 Hz, 1H), 9.18 (dd, J = 6.0, 1.4 Hz, 1H), 8.49 (d, J = 0.7 Hz, 1H), 8.21 (dt, J = 8.1, 1.5 Hz, 1H), 7.88 (d, J = 0.7 Hz, 1H), 7.75 (dd, J = 8.0, 5.8 Hz, 1H), 6.49 (s, 1H); ^{13}C NMR (151 MHz, DMSO-d_6) δ 155.47, 153.38, 146.28, 145.78, 138.10, 125.73, 121.17, 104.30, 90.06, 87.68, 67.50; ESI-MS ($C_{84}H_{56}N_{24}Pd_2$) calc. 403.5780 $[Pd_2L_4]^{4+}$, 567.1064 $[BF_4+Pd_2L_4]^{3+}$, 894.1424 $[2BF_4+Pd_2L_4]^{2+}$; found: 403.5781 $[Pd_2L_4]^{4+}$, 567.1093 $[BF_4+Pd_2L_4]^{3+}$, 894.1436 $[2BF_4+Pd_2L_4]^{2+}$.

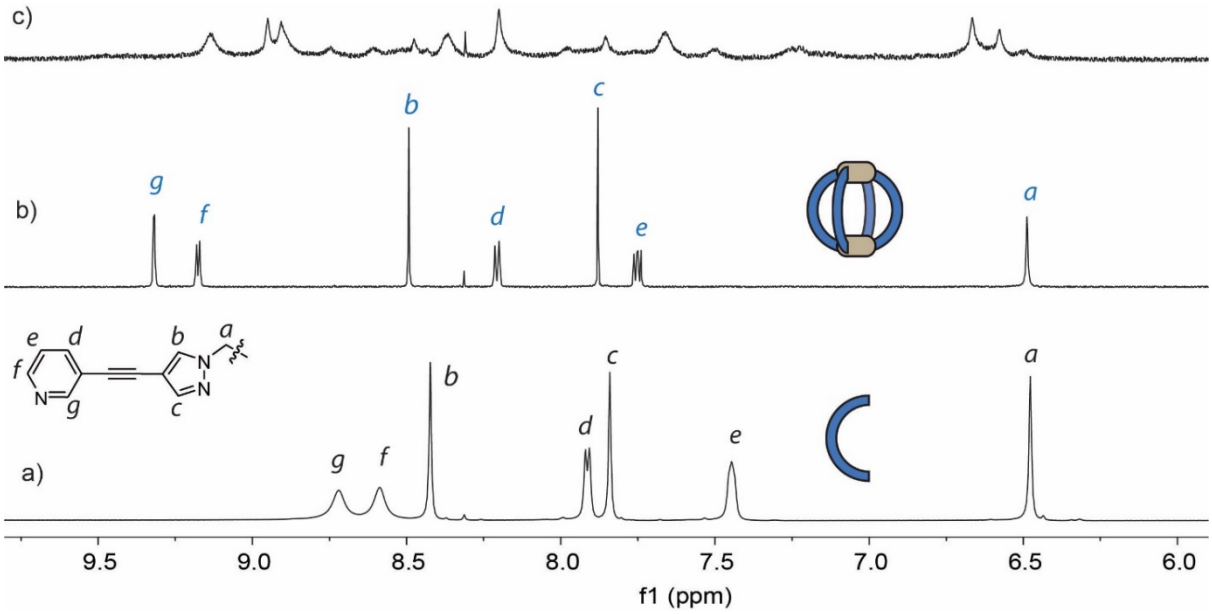

Figure S5. ^{1}H NMR spectrum (600 MHz, DMSO-d_6, 25 °C) of a) **L**; b) **1**; c) **1** heated at 70 °C for 16 h.

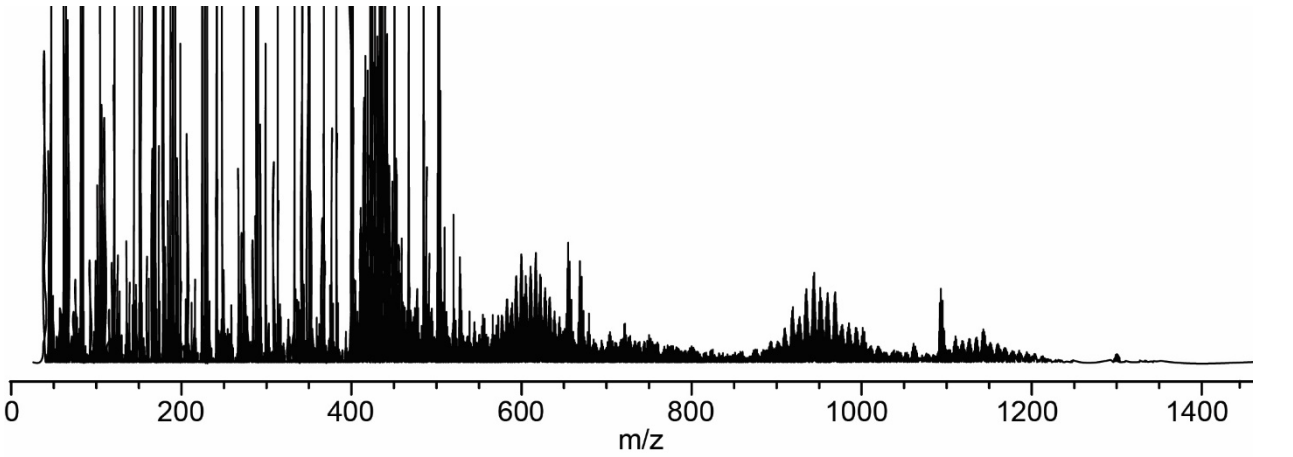

Figure S6. ESI-MS spectrum of **1** formed a complex mixture of species by heating to 70 °C in DMSO-d_6 for 16 h.

*1.2.4. Assembly of dimeric cage [Cl@**2**](BF$_4$)$_7$ (Cl@**2**)*

A solution of [Pd(CH$_3$CN)$_4$(BF$_4$)$_2$] (0.476 mL, 15 mM/CD$_3$CN, 7.13 µmol) was combined with a hot solution of **L** (5 mg, 14.27 µmol) in CD$_3$CN (4.62 mL) and heated at 70 °C for 5 minutes with stirring. To the hot solution, a solution of tetrabutylammonium chloride (0.112 mL, 17.5 mM/CD$_3$CN, 1.96 µmol) was added and heated at 70 °C for 16 h to afford Cl@**2**. Note: the synthesis was also performed in MeCN on larger scales (e.g., 20 mg of **L**); after the heating period (70 °C for 16 h), Cl@**2** was precipitated from MeCN with diethyl ether. The solid was centrifuged and washed successively with ether, before being dried under vacuum at 50 °C. ^{1}H NMR (600 MHz/CD$_3$CN): δ 9.79 (d, J = 1.8 Hz, 1H), 9.49 (s, 1H), 8.91 (d, J = 5.8 Hz, 1H), 8.37 (d, J = 5.8 Hz, 1H), 8.07 (s, 1H), 7.98 (d, J = 8.0 Hz, 1H), 7.81 (s, 1H), 7.67 (s, 1H), 7.61 – 7.50 (m, 2H), 7.19 (s, 1H), 6.07 (s, 2H), 6.02 (dd, J = 7.9, 5.9 Hz, 1H); ^{13}C NMR (151 MHz, CD$_3$CN) δ 157.16, 155.46, 152.45, 152.37, 146.30, 145.53, 144.80, 144.20, 136.30, 136.21, 130.04, 127.24, 126.83, 125.65, 105.20, 104.73, 89.27, 89.21, 88.04, 87.39, 74.84, 67.42, 63.68; ^{19}F NMR (565 MHz, CD$_3$CN) δ -151.62; ESI-MS (C$_{168}$H$_{112}$N$_{48}$Pd$_4$ClB$_2$F$_8$) calc. 687.5221 [Cl@Pd$_4$L$_8$ + 2BF$_4$]$^{5+}$; found: 687.5231 [Cl@Pd$_4$L$_8$ + 2BF$_4$]$^{5+}$.

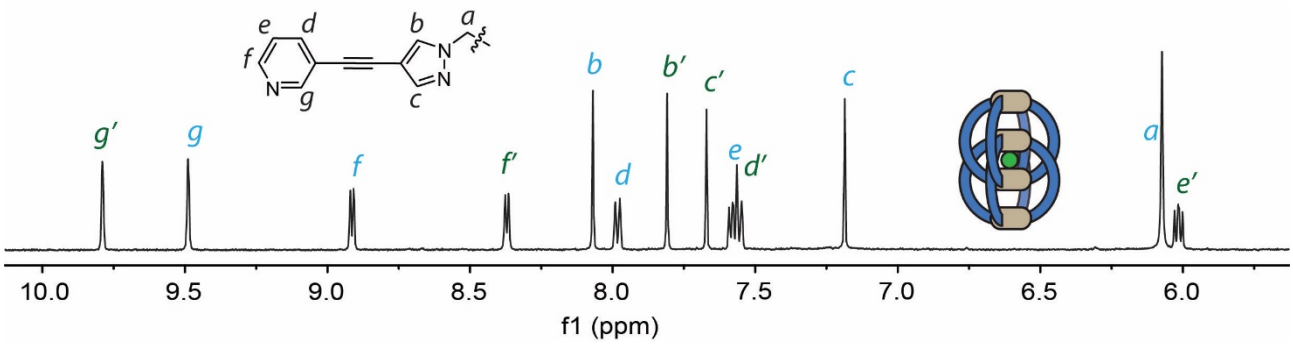

Figure S7. ^{1}H NMR spectrum (600 MHz, CD$_3$CN, 25 °C) of Cl@**2**.

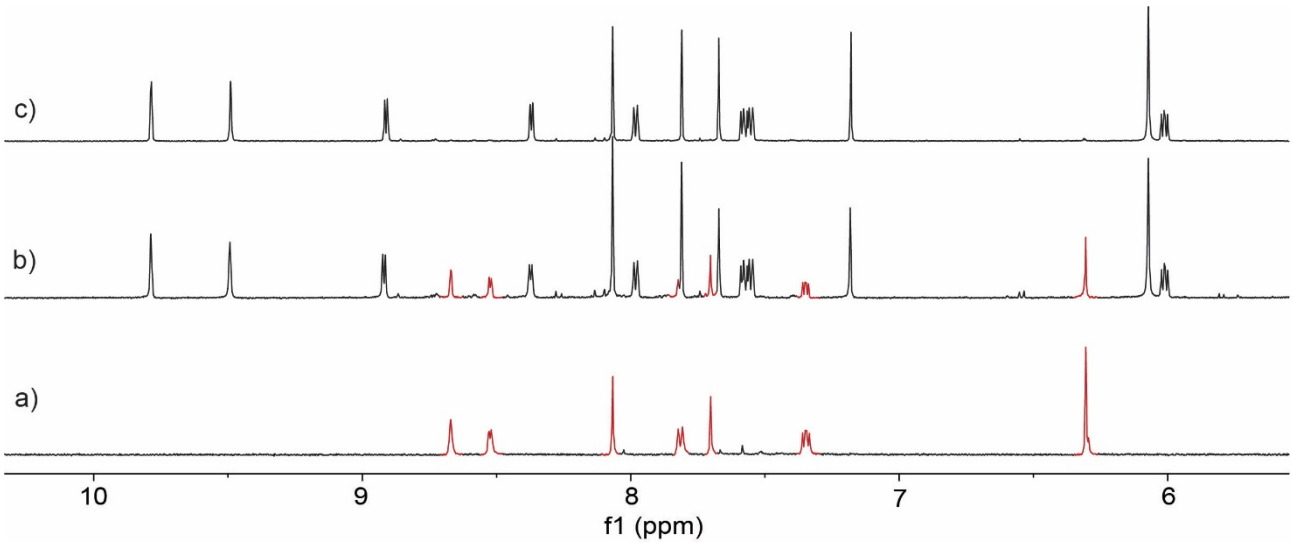

Figure S8. ^{1}H NMR spectrum (600 MHz, CD_3CN, 25 °C) of a) **L**; b) **1** + 1.1 equivalents of TBACl, heated at 70 °C for 24 h; c) **1** + 0.52 equivalents of Cl^-, heated at 70 °C for 24 h.

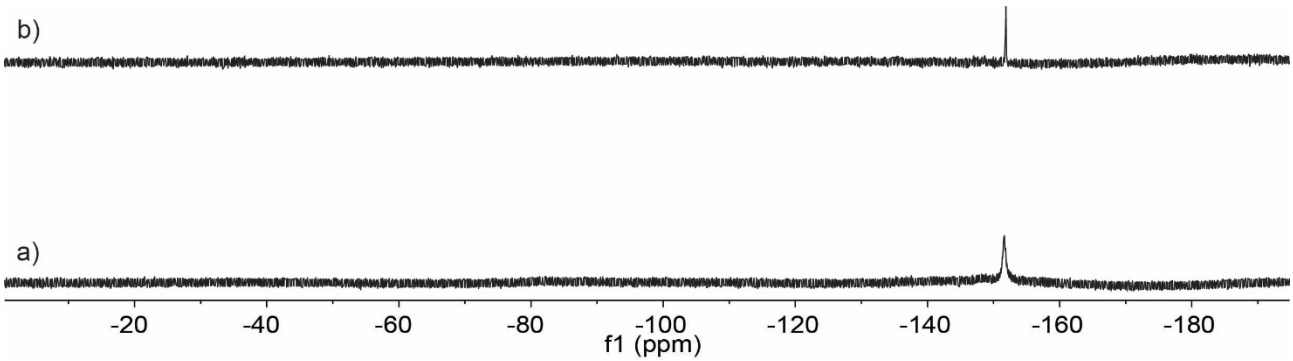

Figure S9. ^{19}F NMR spectrum (565 MHz, CD_3CN, 25 °C) of a) Cl@**2**; b) Cl@**2** measured at -35 °C.

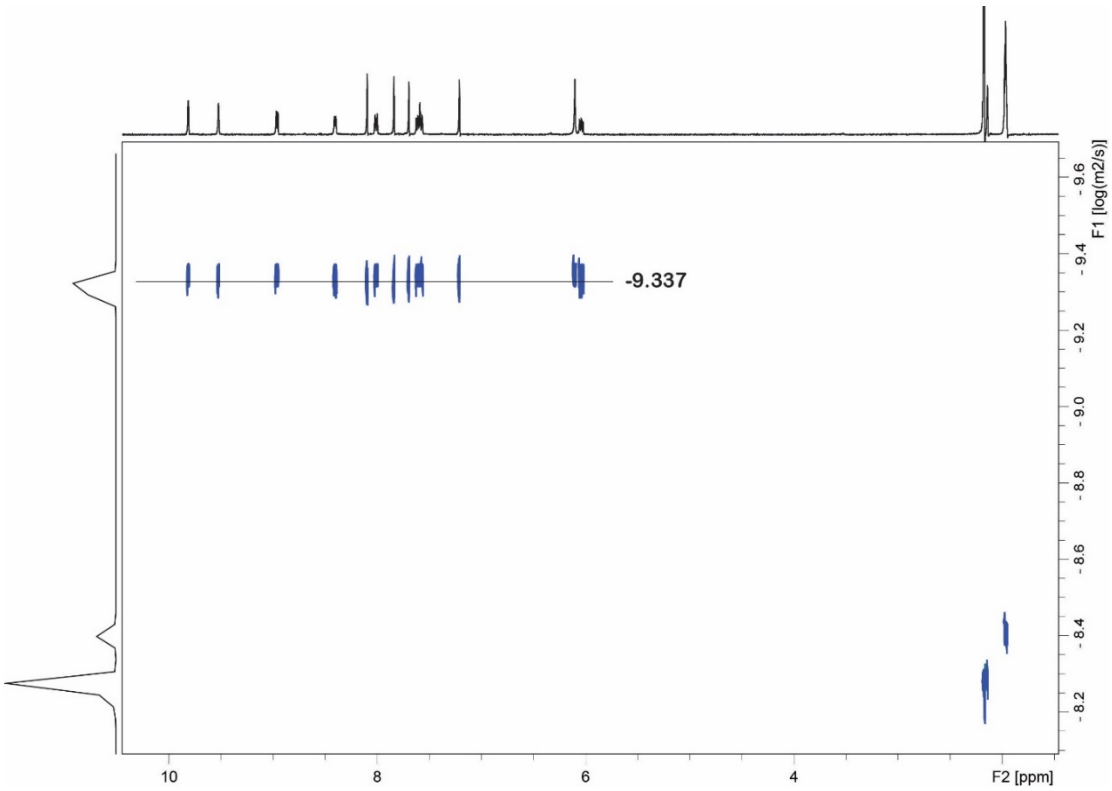

Figure S10. ^{1}H NMR DOSY spectrum (400 MHz, CD_3CN, 25 °C) of Cl@**2**. The interpenetrated cage diffuses at 4.60×10^{-10} m^2/s, log D = –9.337.

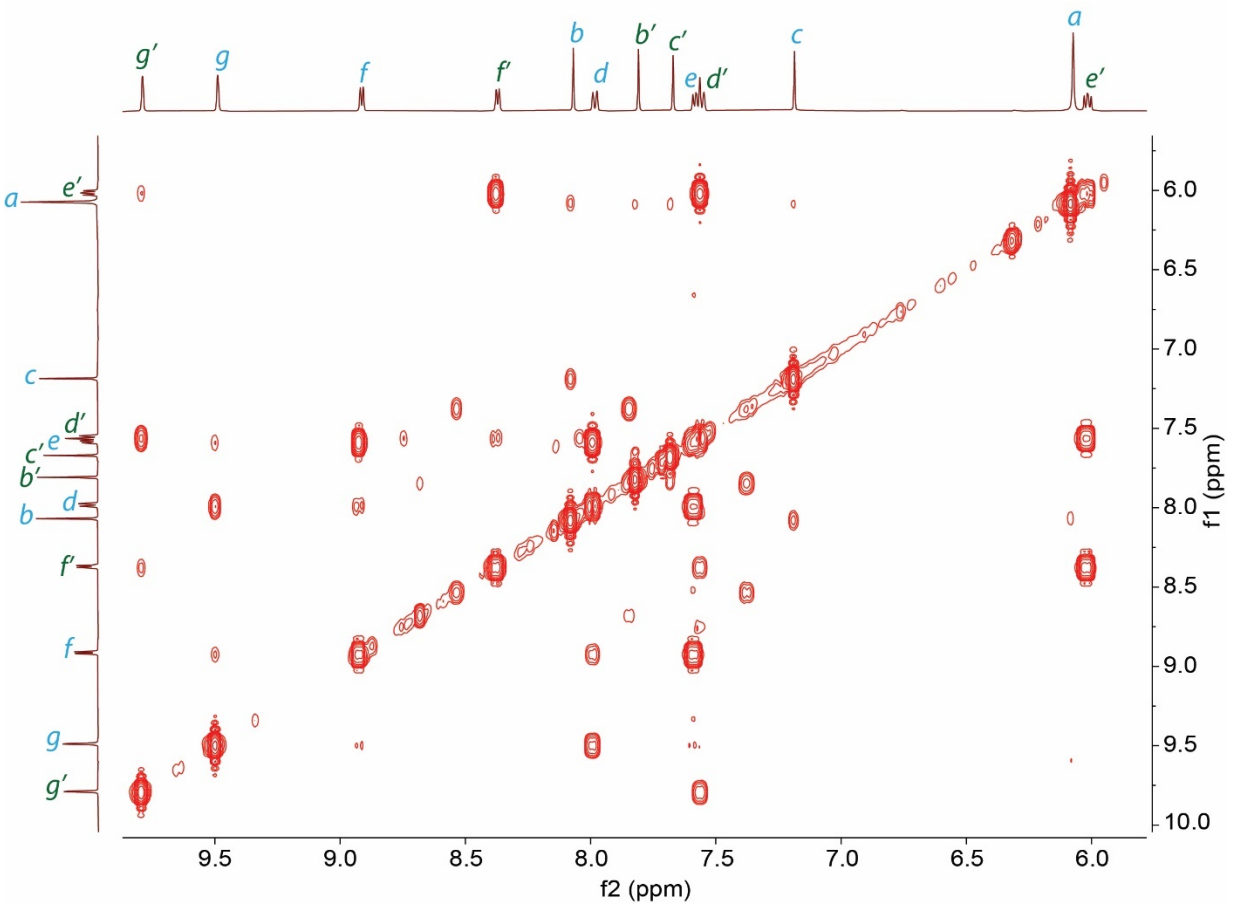

Figure S11. ^{1}H-^{1}H COSY NMR spectrum (500 MHz, CD_3CN, 25 °C) of Cl@**2**.

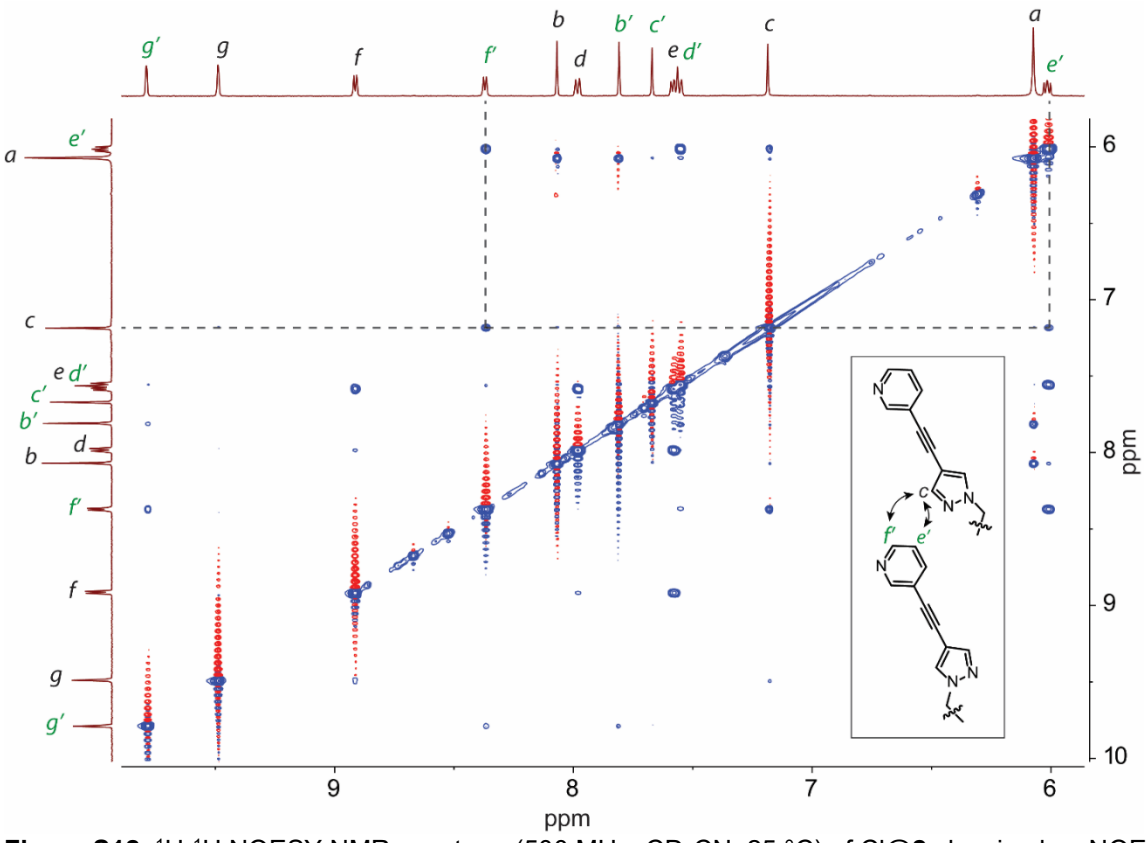

Figure S12. ^{1}H-^{1}H NOESY NMR spectrum (500 MHz, CD_3CN, 25 °C) of Cl@**2** showing key NOE contacts.

*1.2.5. Assembly of dimeric cage [Br@**2**](BF₄)₇* (Br@**2**)

A solution of $[Pd(CH_3CN)_4(BF_4)_2]$ (0.476 mL, 15 mM/CD_3CN, 7.13 µmol) was combined with a hot solution of **L** (5 mg, 14.27 µmol) in CD_3CN (4.62 mL) and heated at 70 °C for 5 minutes with stirring. To the hot solution, a solution of tetrabutylammonium bromide (>99%, 0.112 mL, 17.5 mM/CD_3CN, 1.96 µmol) was added and heated at 70 °C for 16 h to afford Br@**2**. Note: the synthesis was also performed in MeCN on larger scales (e.g., 20 mg of **L**); after the heating period (70 °C for 16 h), Br@**2** was precipitated from MeCN with diethyl ether. The solid was centrifuged and washed successively with ether, before being dried under vacuum at 50 °C. ^{1}H NMR (600 MHz/CD_3CN): δ 9.74 (s, 1H), 9.54 (s, 1H), 8.91 (d, J = 5.8 Hz, 1H), 8.35 (d, J = 5.8 Hz, 1H), 8.07 (s, 1H), 7.97 (d, J = 8.0 Hz, 1H), 7.85 (s, 1H), 7.83 (s, 1H), 7.57 (dd, J = 7.9, 6.0 Hz, 1H), 7.49 (d, J = 8.0 Hz, 1H), 6.96 (s, 1H), 6.06 (s, 2H), 6.00 (t, J = 7.0 Hz, 1H); ^{19}F NMR (565 MHz, CD_3CN) δ -146.88, -151.51; ESI-MS ($C_{168}H_{112}N_{48}Pd_4BrB_2F_8$) calc. 696.3140 $[2BF_4+Br@Pd_4L_8]^{5+}$, 892.1493 $[3BF_4+Br@Pd_4L_8]^{4+}$, 1218.5385 $[4BF_4+Br@Pd_4L_8]^{3+}$, 1871.2987 $[5BF_4+Br@Pd_4L_8]^{2+}$; found: 696.1431 $[2BF_4+Br@Pd_4L_8]^{5+}$, 892.1500 $[3BF_4+Br@Pd_4L_8]^{4+}$, 1218.6178 $[4BF_4+Br@Pd_4L_8]^{3+}$, 1871.3250 $[5BF_4+Br@Pd_4L_8]^{2+}$.

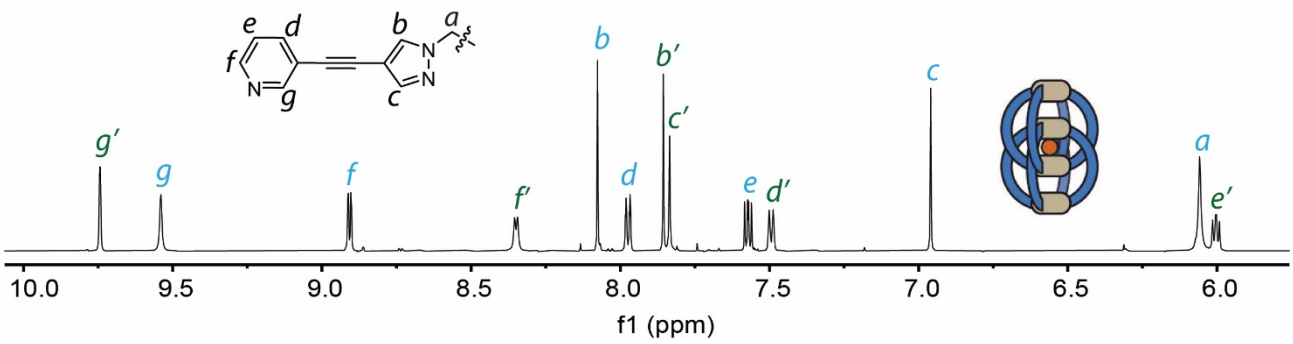

Figure S13. ^{1}H NMR spectrum (600 MHz, CD_3CN, 25 °C) of Br@**2**.

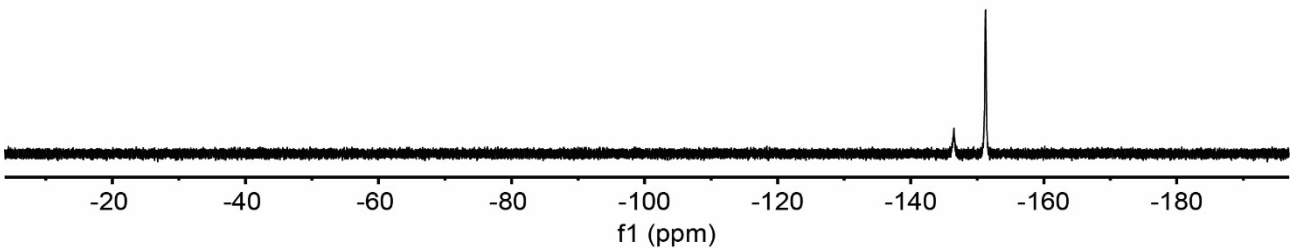

Figure S14. ^{19}F NMR spectrum (565 MHz, CD_3CN, 25 °C) of Br@**2** showing free BF_4^- (-151.5 ppm) and bound BF_4^- (-146.8 ppm).

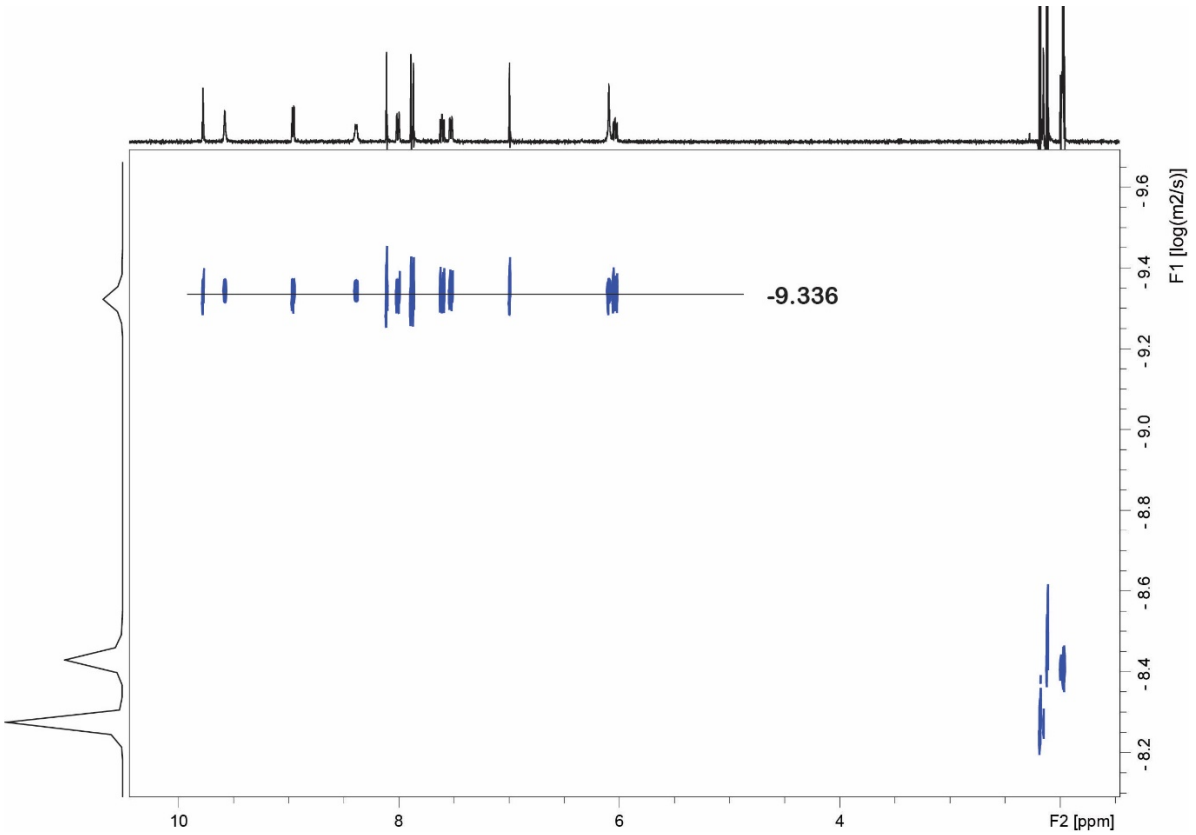

Figure S15. ^{1}H NMR DOSY spectrum (400 MHz, CD_3CN, 25 °C) of Br@**2**. The interpenetrated cage diffuses at 4.61 × 10^{-10} m^2/s, log *D* = –9.336.

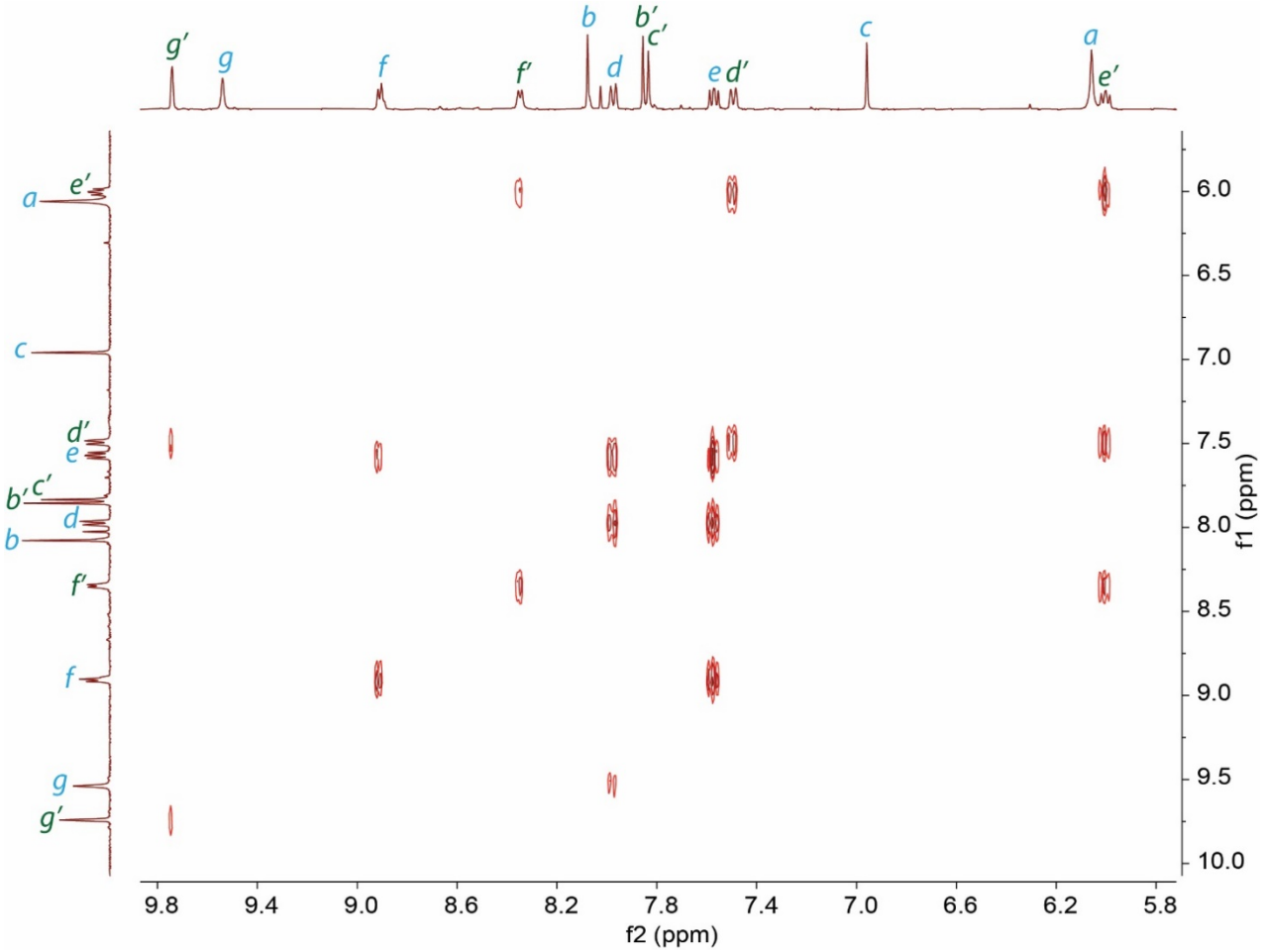

Figure S16. ^{1}H-^{1}H COSY NMR spectrum (600 MHz, CD_3CN, 25 °C) of Br@**2**.

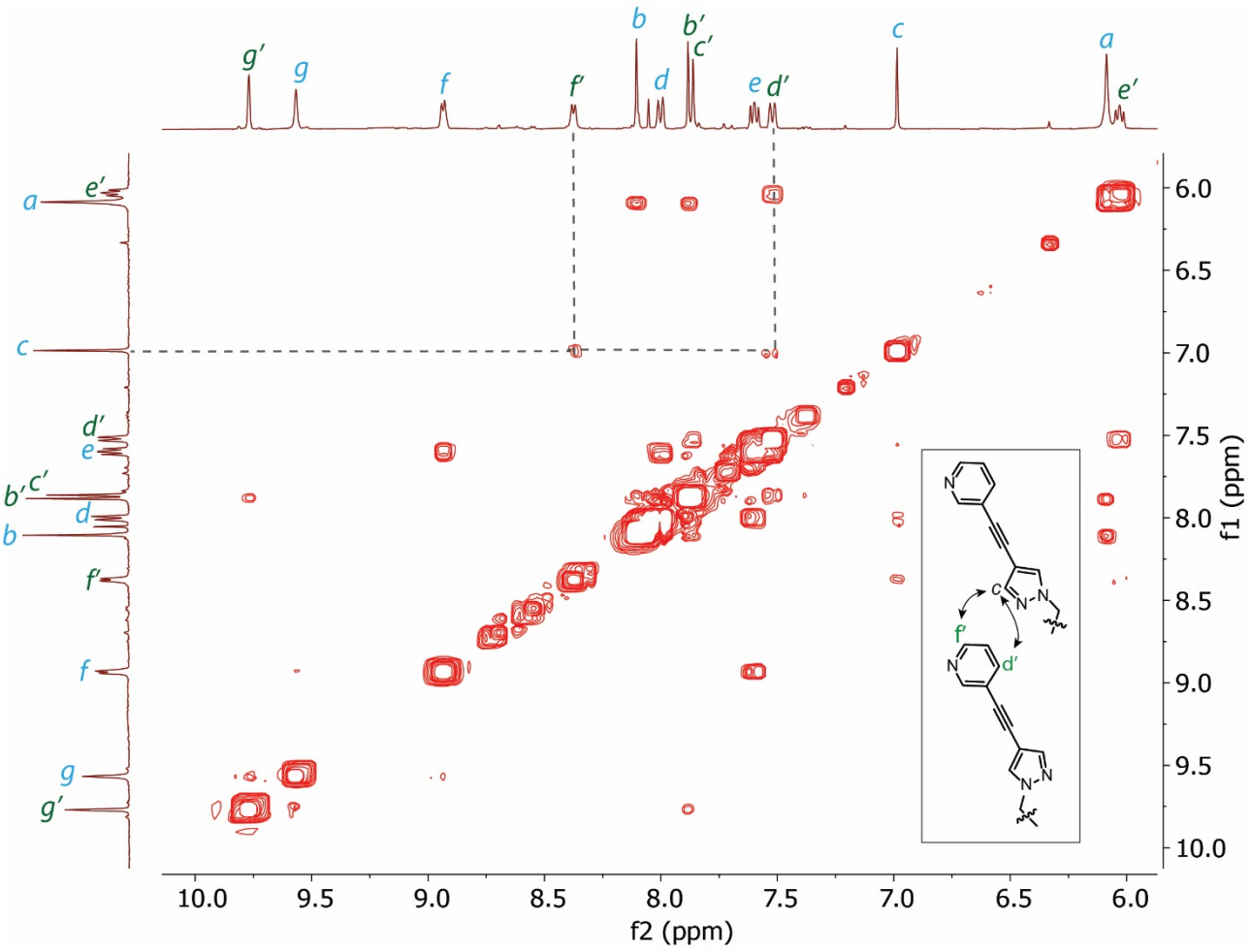

Figure S17. ^{1}H-^{1}H NOESY NMR spectrum (600 MHz, CD_3CN, 25 °C) of Br@**2** showing key NOE contacts.

*1.2.6. Assembly of dimeric cage [3NO_3@**2**](NO_3)$_5$* (3NO_3@**2**)

A solution of [Pd(NO_3)$_2$]2H_2O (0.476 mL, 15 mM/CD_3CN, 8.56 µmol) was combined with a hot solution of **L** (5 mg, 14.27 µmol) in CD_3CN (4.62 mL) and heated at 70 °C for 3 hours with stirring. A mixture of 3NO_3@**2** and free ligand was afforded. ^{1}H NMR (600 MHz/CD_3CN): δ 9.82 (s, 1H), 9.17 (m, 2H), 8.48 (d, J = 5.7 Hz, 1H), 8.07 (s, 1H), 7.98 (d, J = 8.0 Hz, 1H), 7.90 (s, 1H), 7.80 (s, 1H), 7.58 (t, J = 6.1 Hz, 1H), 7.34 (d, J = 8.3 Hz, 1H), 6.84 (s, 1H), 6.20 (t, J = 6.3 Hz, 1H), 6.11 (s, 2H); ESI-MS ($C_{168}H_{112}N_{48}Pd_4BrB_2F_8$) calc. 682.9245 [3$NO_3$@$Pd_4L_8$]$^{5+}$, found: 682.8931 [3$NO_3$+$Pd_4L_8$]$^{5+}$.

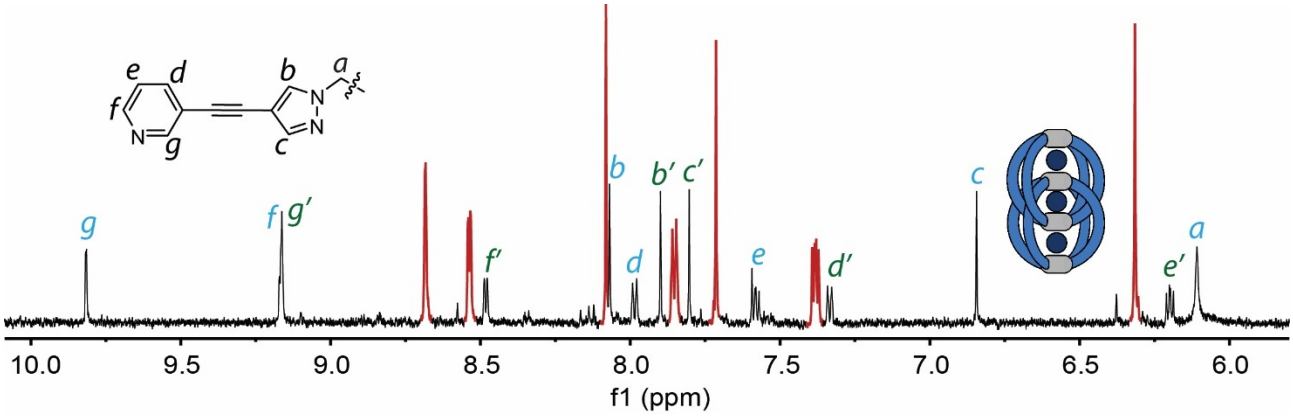

Figure S18. ^{1}H NMR spectrum (600 MHz, CD_3CN, 25 °C) of 3NO_3@**2**, red shows free ligand.

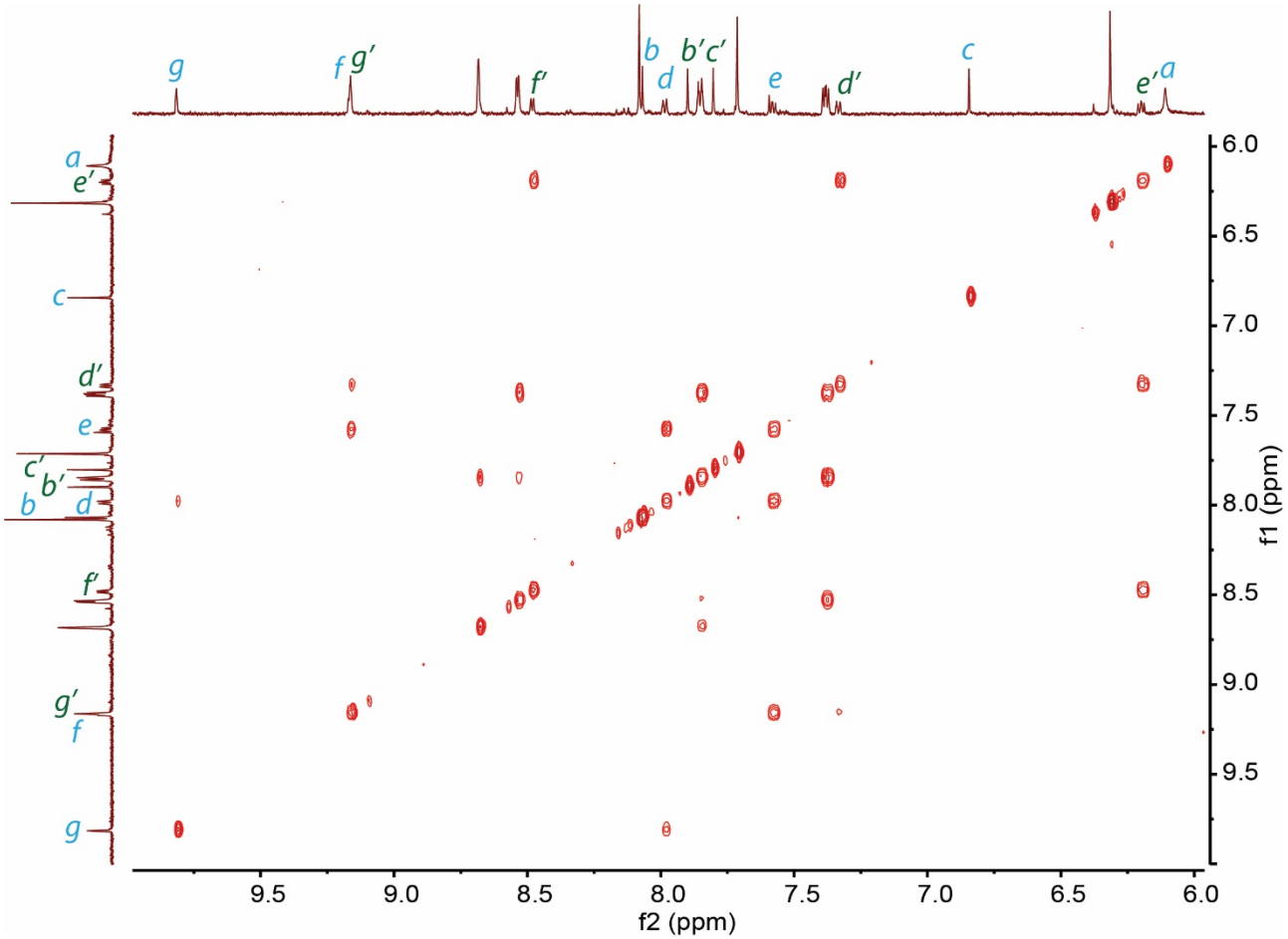

Figure S19. ^{1}H-^{1}H COSY NMR spectrum (600 MHz, CD_3CN, 25 °C) of 3NO_3@**2**.

2. Host-guest studies by ^{1}H NMR

2.1 Cl@2 titrations

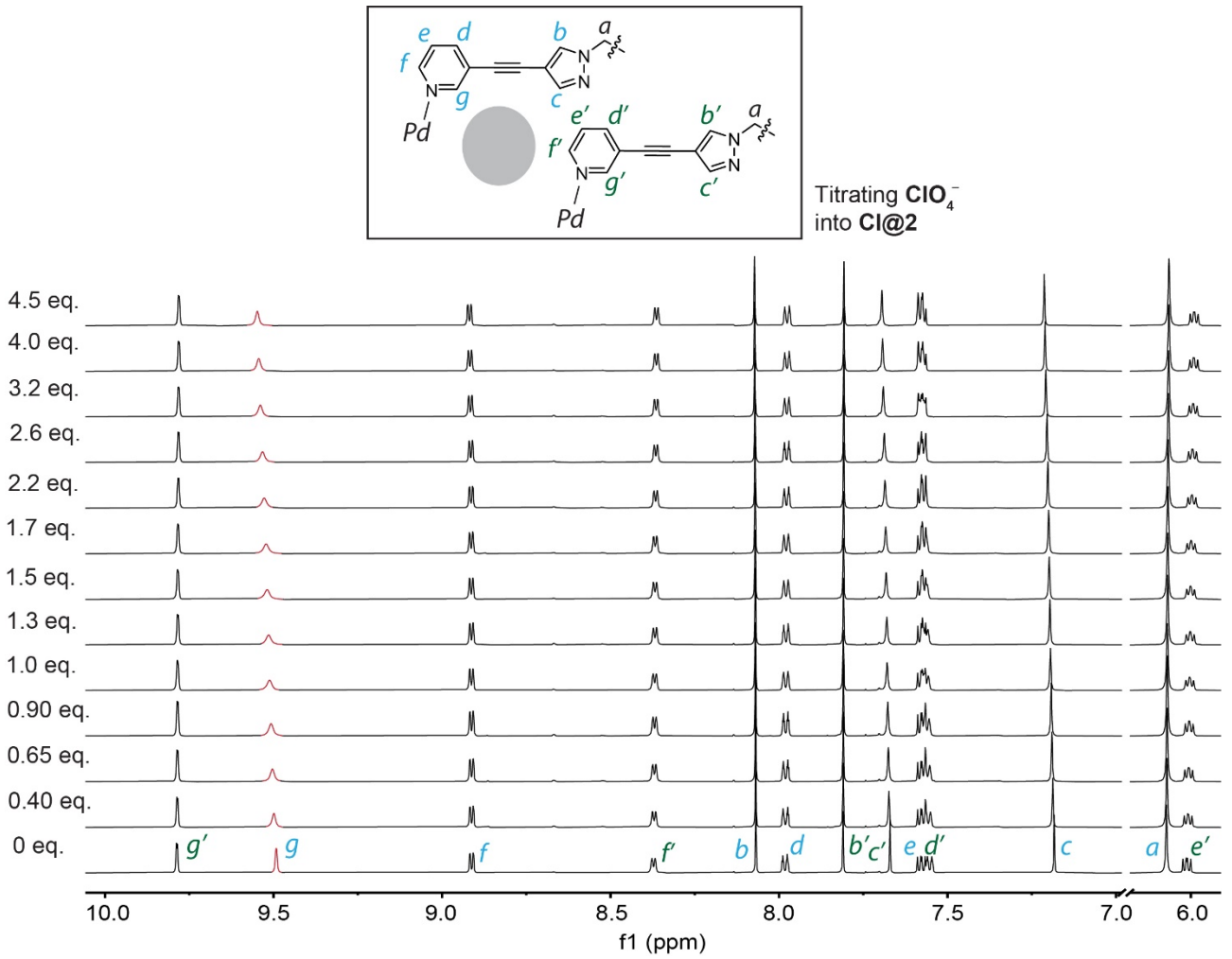

Figure S20. ^{1}H NMR spectra (600 MHz, CD_3CN, 25 °C): titration of $TBAClO_4$ into a 0.27 mM solution of Cl@**2**. Shifts in g (inside pointing proton) are observed, indicating ClO_4^- binds inside of the cage cavity (grey).

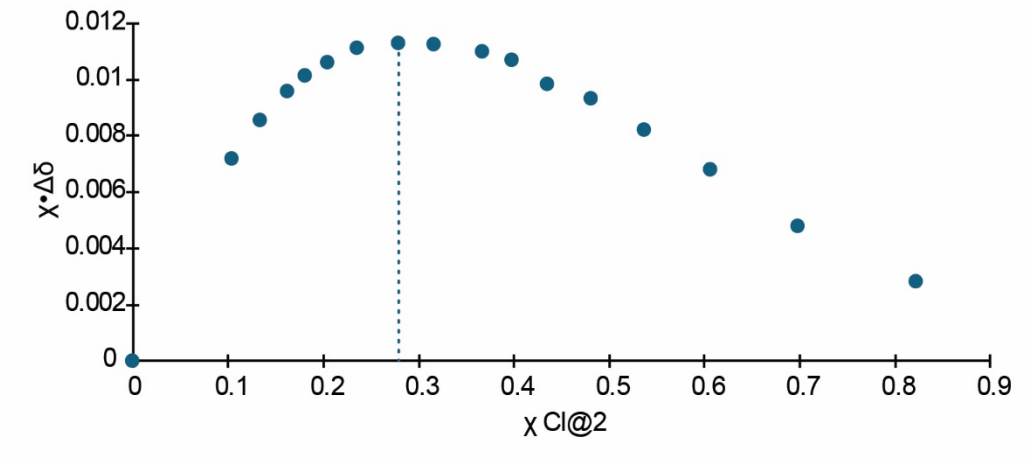

Figure S21. Job-plot following g (inside pointing proton) from H:G titration of $TBACIO_4$ into 0.27 mM solution of Cl@**2**. The maximum intercept is close to the expected H:G ratio of 1:2.

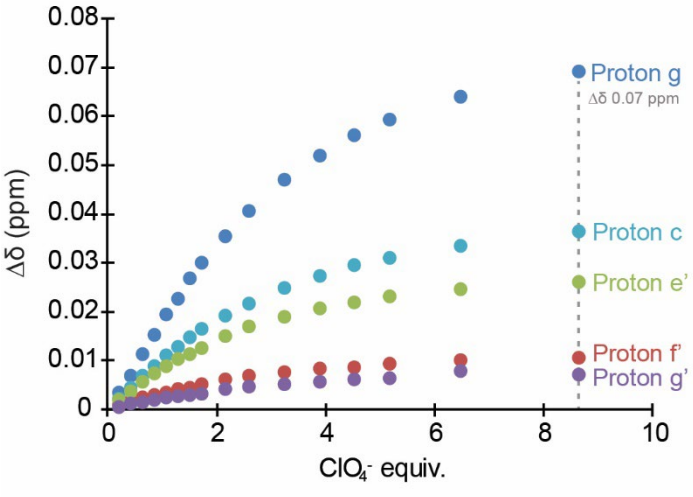

Figure S22. $TBACIO_4$ change in chemical shift graph following Cl@**2** protons g, f' e' and c (inside pointing protons, outer pocket) and g' (inside pointing proton, inner pocket). g has an overall change in chemical shift of 0.07 ppm.

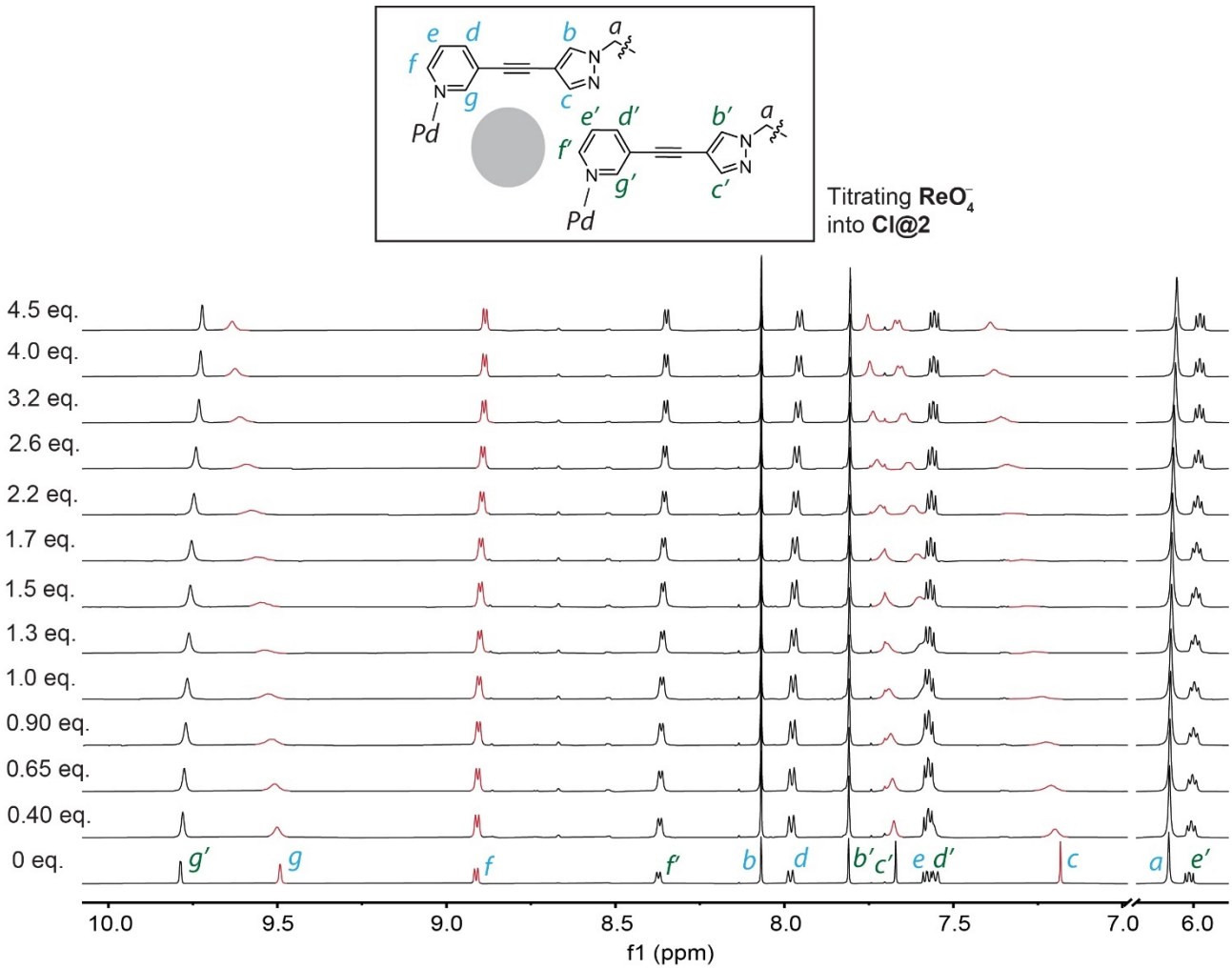

Figure S23. ^{1}H NMR spectra (600 MHz, CD_3CN, 25 °C): titration of TBAReO_4 into a 0.27 mM solution of Cl@**2**. Shifts and broadening in g and c (inside pointing protons) are observed, indicating ReO_4^- binds inside of the cage cavity (grey). Whilst, shifts in f, c', and e (outside pointing protons) are observed indicating that ReO_4^- binds not directly between the Pd(II) centers.

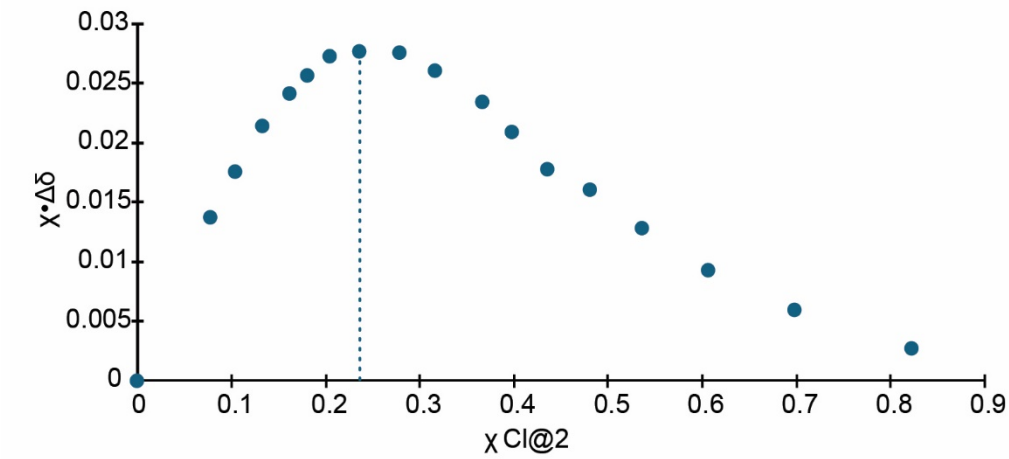

Figure S24. Job-plot following g (inside pointing proton) from H:G titration of $TBAReO_4$ into 0.27 mM solution of Cl@**2**. The maximum intercept is close to the expected H:G ratio of 1:2.

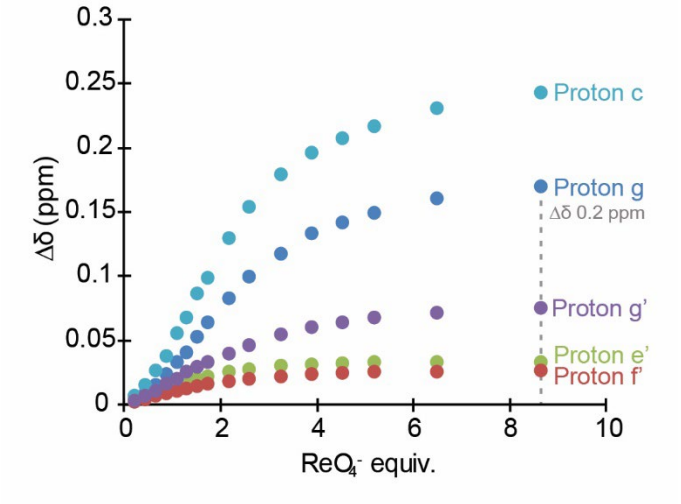

Figure S25. $TBAReO_4$ change in chemical shift graph following Cl@**2** protons g, f' e' and c (inside pointing protons, outer pocket) and g' (inside pointing proton, inner pocket). g has an overall change in chemical shift of 0.2 ppm.

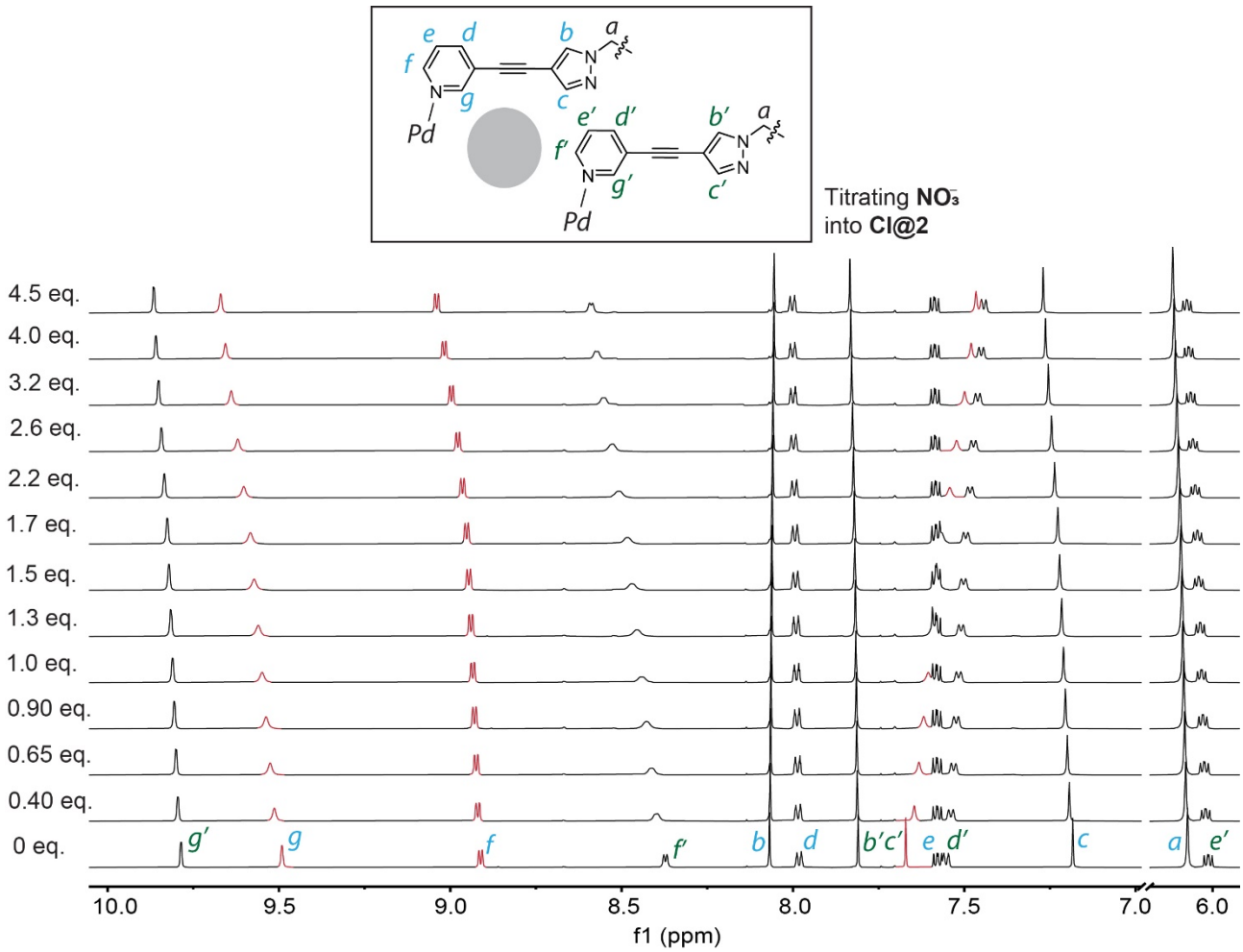

Figure S26. ^{1}H NMR spectra (600 MHz, CD_3CN, 25 °C): titration of $TBANO_3$ into a 0.27 mM solution of Cl@**2**. Shifts in g (inside pointing proton) are observed, indicating NO_3^- binds inside of the cage cavity (grey). Shifts in f, e and c' indicate that NO_3^- also may also bind on the outside of the cage cavity (grey).

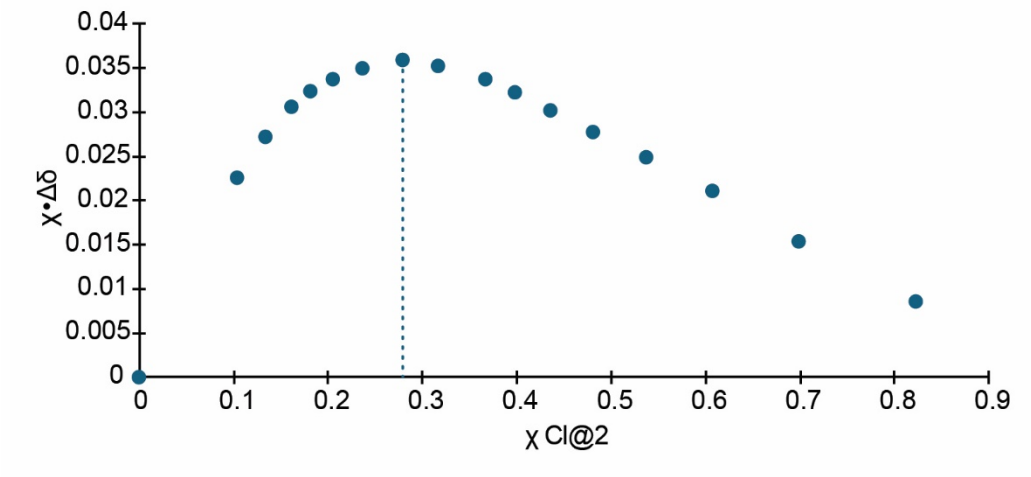

Figure S27. Job-plot following g (inside pointing proton) from H:G titration of $TBANO_3$ into 0.27 mM solution of Cl@**2**. The maximum intercept is close to the expected H:G ratio of 1:2.

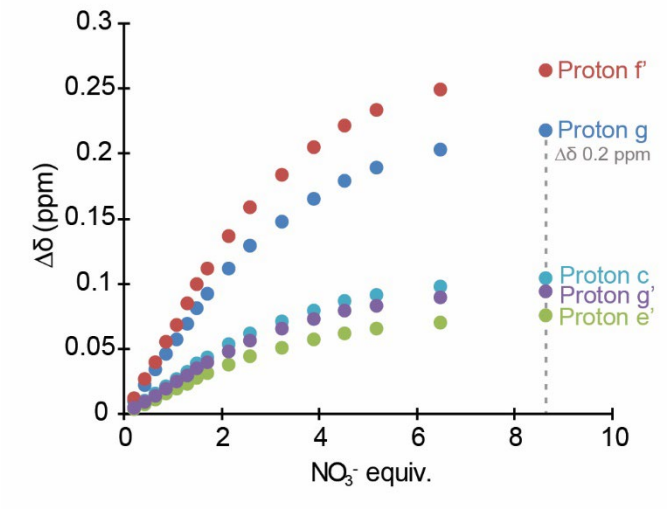

Figure S28. $TBANO_3$ change in chemical shift graph following Cl@**2** protons g, f' e' and c (inside pointing protons, outer pocket) and g' (inside pointing proton, inner pocket). g has an overall change in chemical shift of 0.2 ppm.

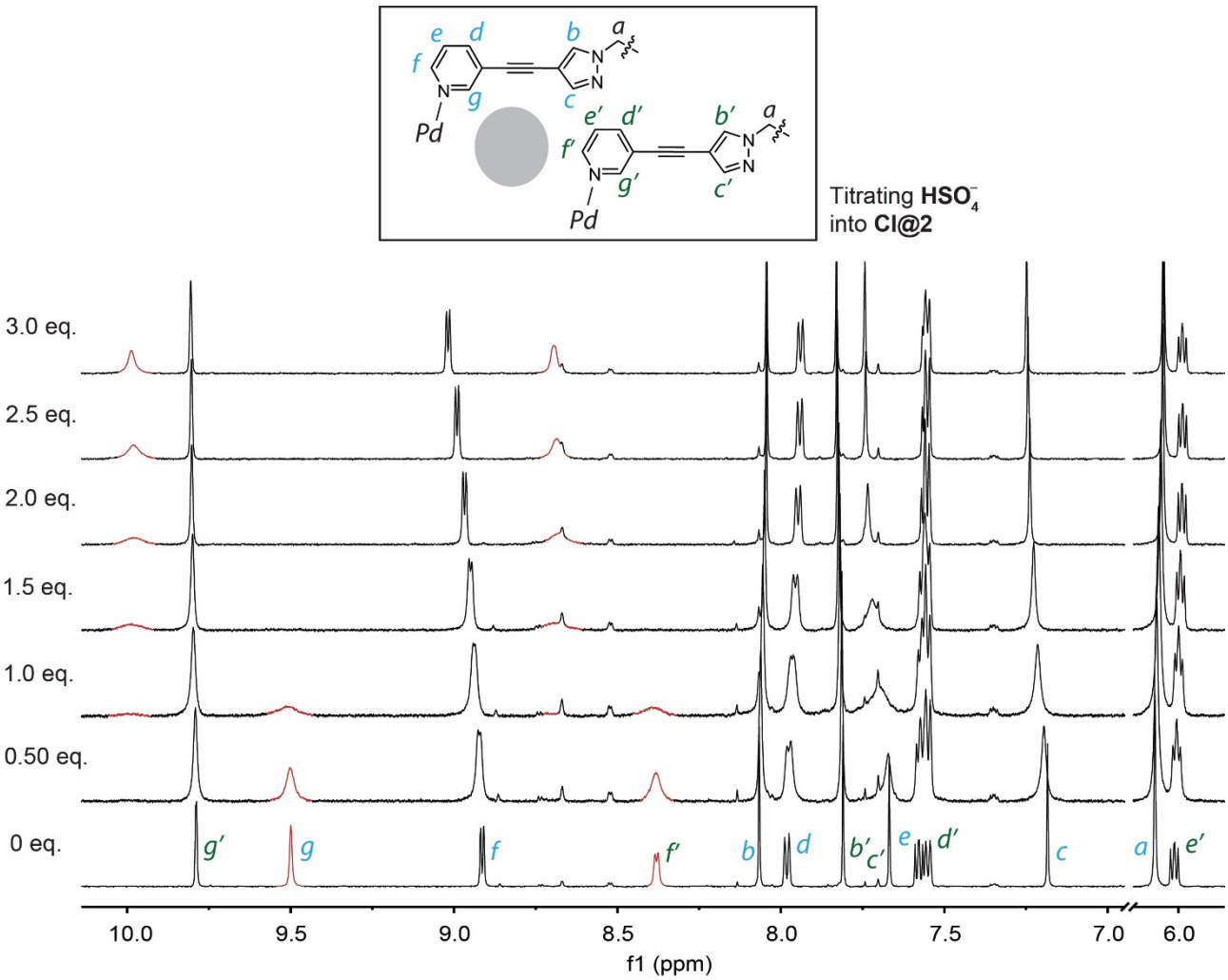

Figure S29. ^{1}H NMR spectra (600 MHz, CD_3CN, 25 °C): titration of $TBAHSO_4$ into a 0.30 mM solution of Cl@**2**. Shifts in g and f' (inside pointing protons) are observed in slow exchange and indicate HSO_4^- binds inside of the cage cavity (grey). Precipitation was observed at 3.0 equivalents.

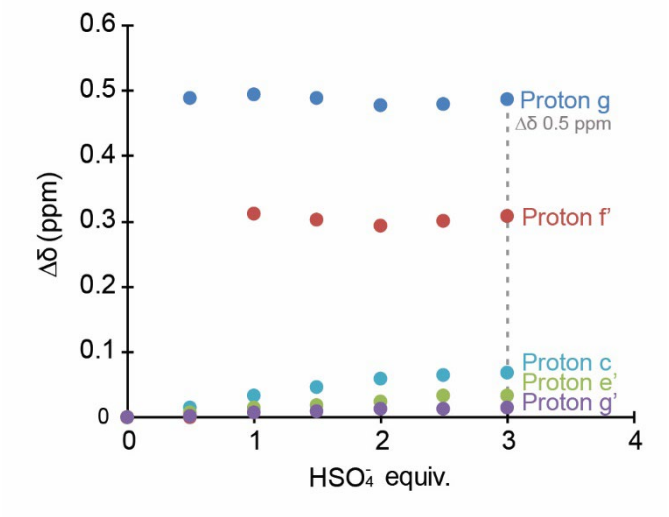

Figure S30. $TBAHSO_4$ change in chemical shift graph following Cl@**2** protons g, f' e' and c (inside pointing protons, outer pocket) and g' (inside pointing proton, inner pocket). g has an overall change in chemical shift of 0.5 ppm.

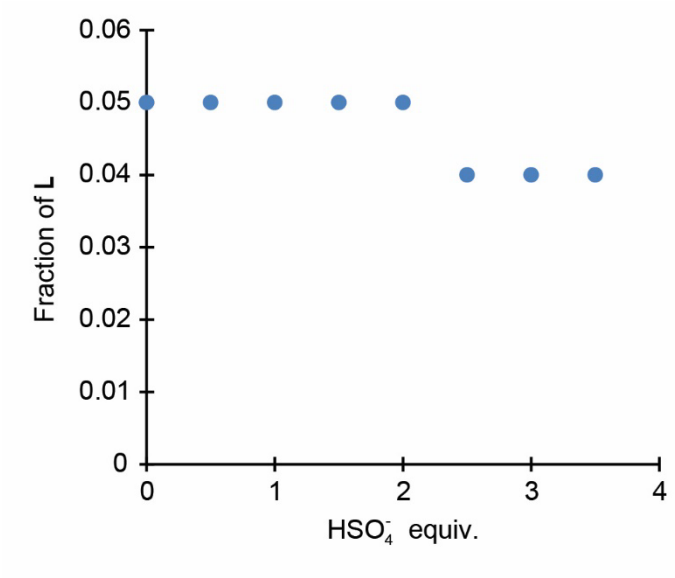

Figure S31. Fraction of residual **L** based on Cl@**2** proton a integration. The integration of residual **L** does not increase with higher equivalents of $TBAHSO_4$ indicating no presence of Cl@**2** decomposition.

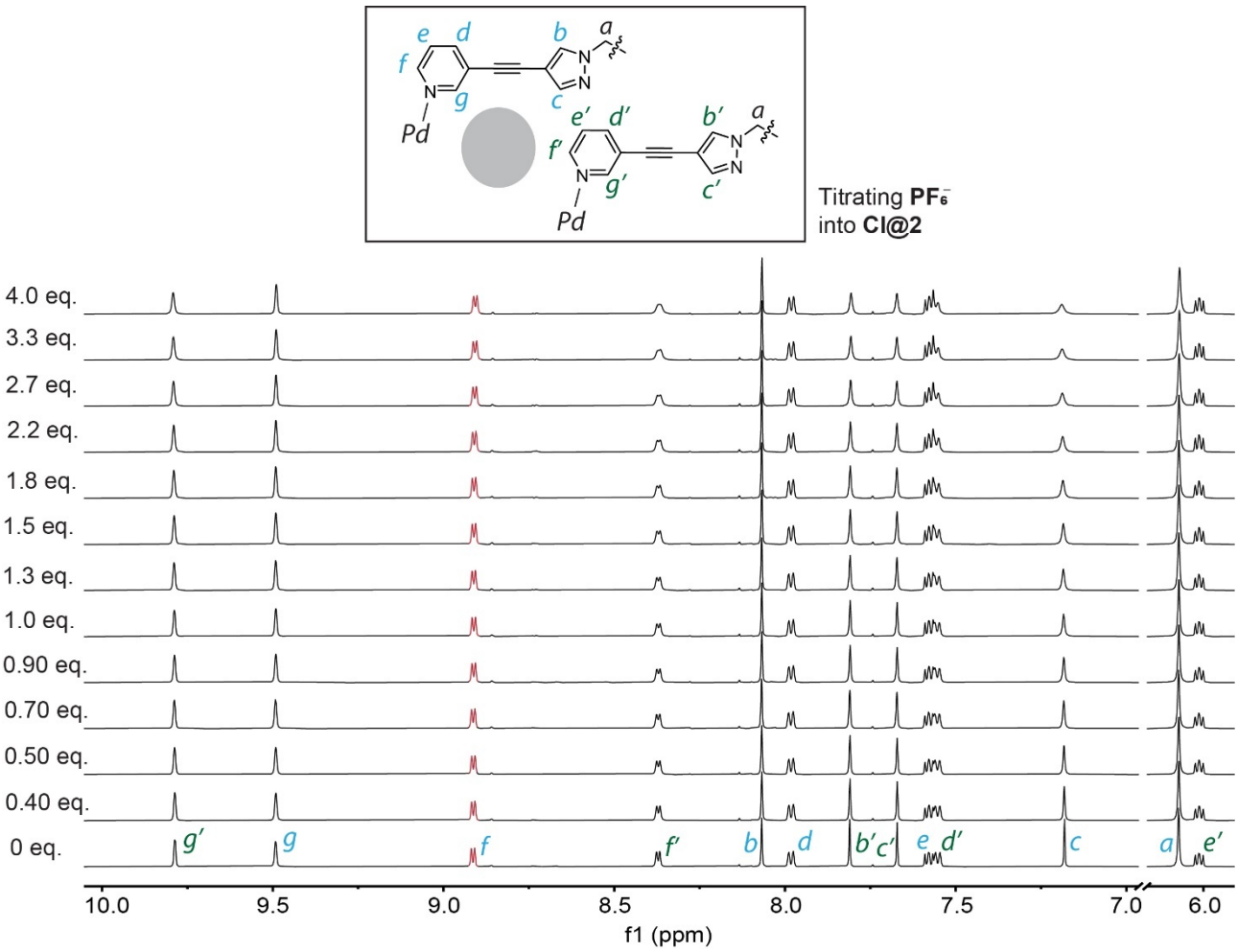

Figure S32. ^1H NMR spectra (600 MHz, CD_3CN, 25 °C): titration of $TBAPF_6$ into a 0.32 mM solution of Cl@**2**. Shifts in f (outside pointing proton) are observed, and at higher equivalents. As protons g and f' (which point directly into the cavity) do not shift, the data indicates PF_6^- binds outside of the cage cavity (grey).

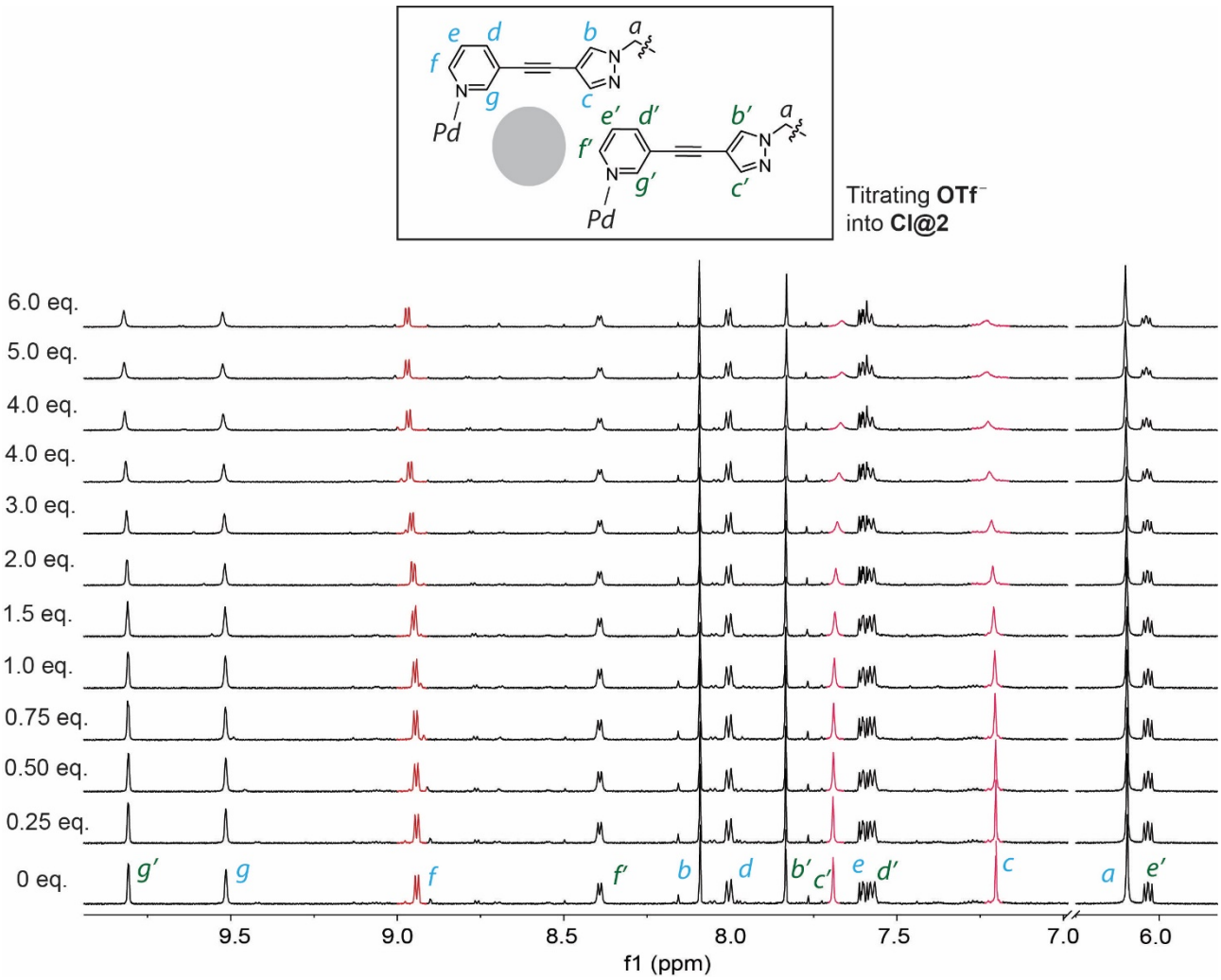

Figure S33. ^{1}H NMR spectra (600 MHz, CD_3CN, 25 °C): titration of TBAOTf into a 0.12 mM solution of Cl@**2**. Shifts in f (outside pointing proton) are observed, and at higher equivalents, shifting and broadening of protons c and c' occurs. As protons g and f' (which point directly into the cavity) do not shift, the data indicates OTf^- binds outside of the cage cavity (grey).

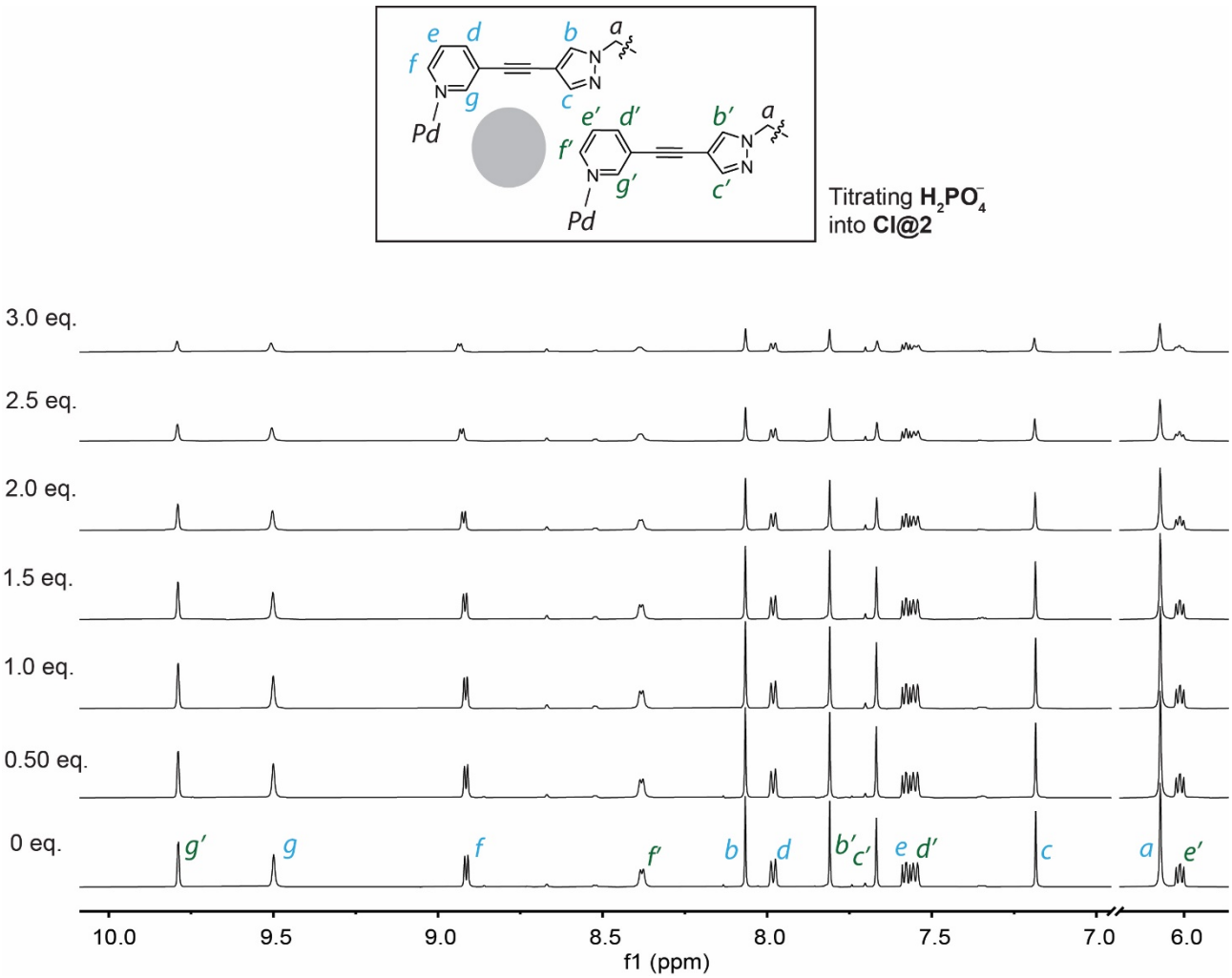

Figure S34. ^{1}H NMR spectra (600 MHz, CD_3CN, 25 °C): titration of $TBAH_2PO_4$ into a 0.30 mM solution of Cl@**2**. No prominent proton shifts indicate no binding. Precipitation was observed at 2.0 equivalents.

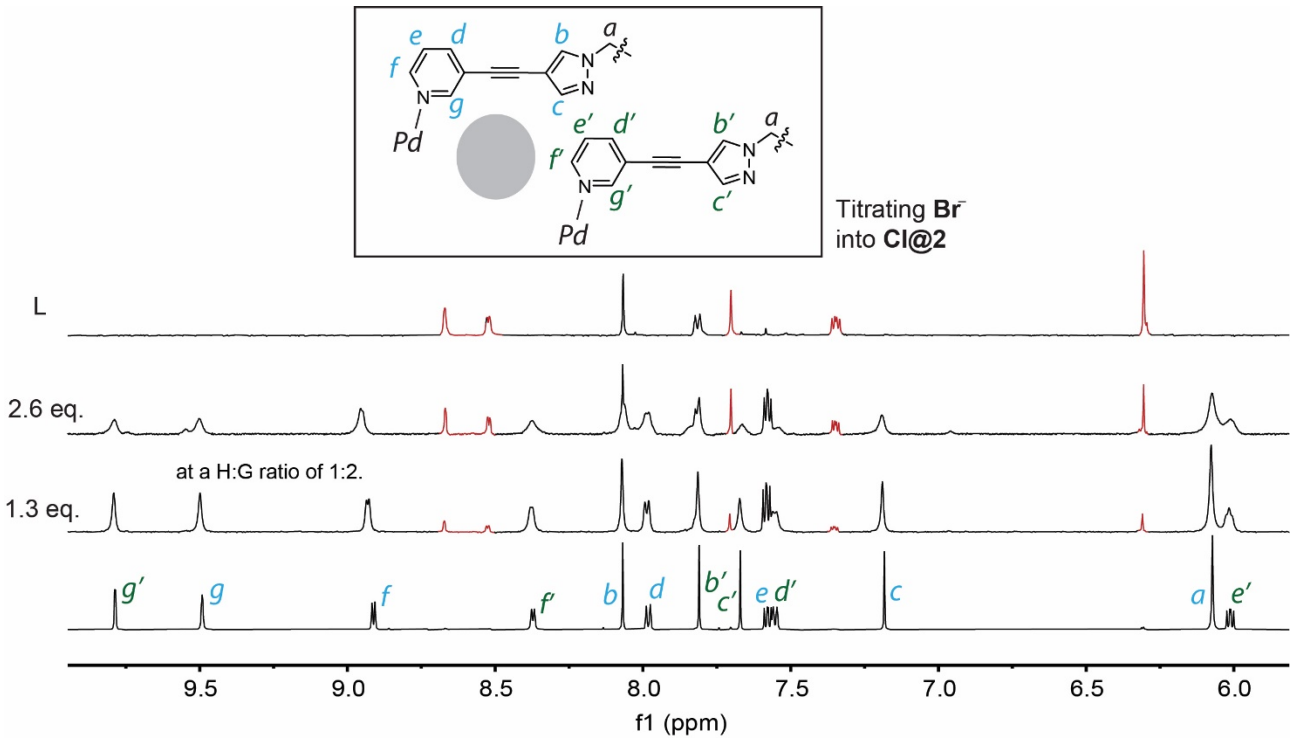

Figure S35. ^{1}H NMR spectra (600 MHz, CD_3CN, 25 °C): titration of TBABr into a 0.27 mM solution of Cl@**2**. Cage decomposition occurs as free ligand peaks (red) increase at higher equivalents. Precipitation was observed at 1.3 equivalents.

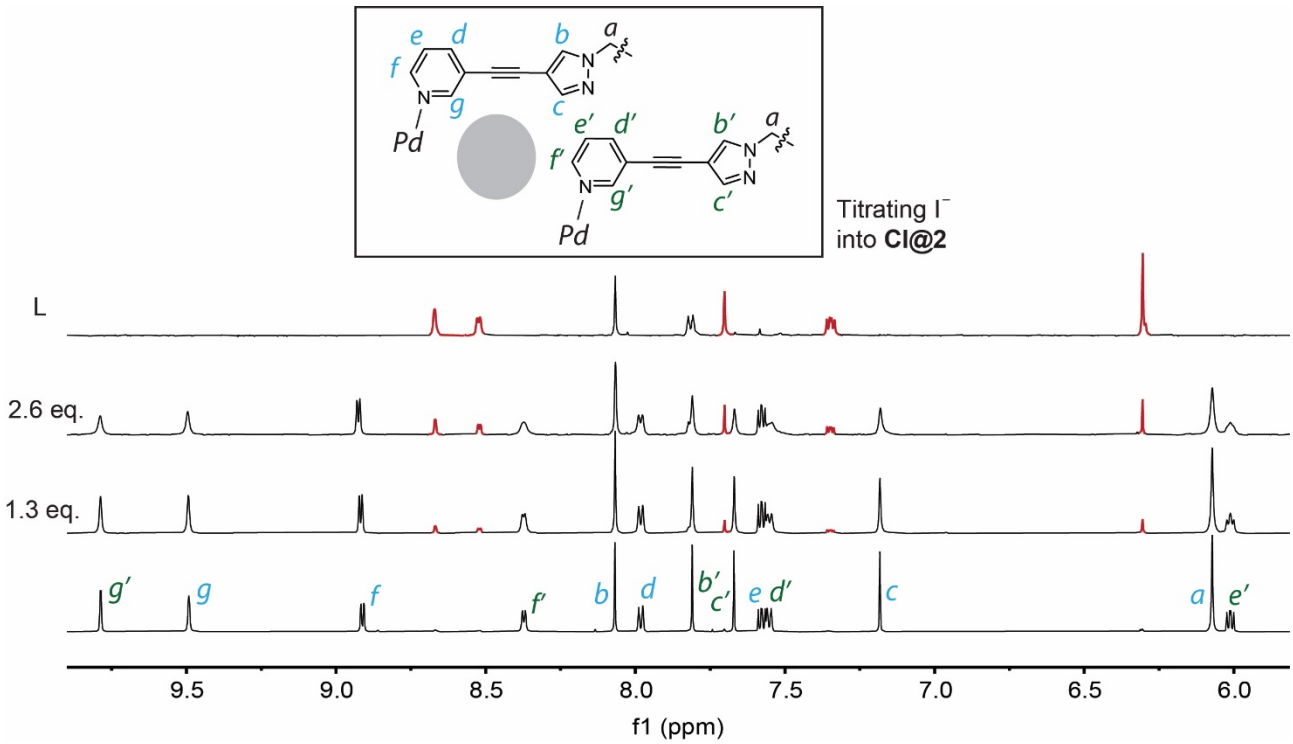

Figure S36. ^{1}H NMR spectra (600 MHz, CD_3CN, 25 °C): titration of TBAI into a 0.27 mM solution of Cl@**2**. Cage decomposition occurs as free ligand peaks (red) increase at higher equivalents. Precipitation was observed at 1.3 equivalents.

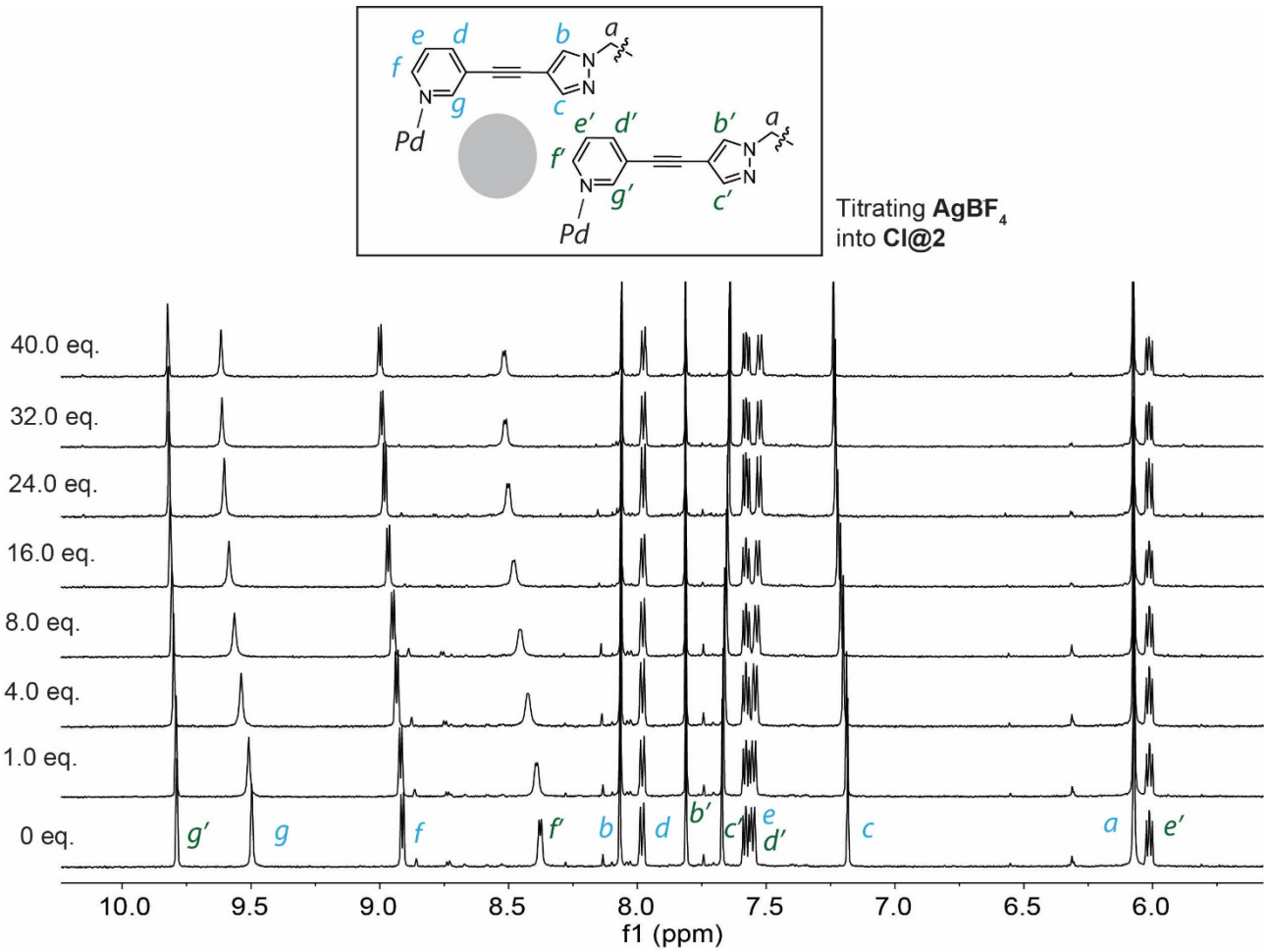

Figure S37. ^{1}H NMR spectra (600 MHz, CD_3CN, 25 °C): titration of $AgBF_4$ into a 0.35 mM solution of Cl@**2**. Shifts in g (inside pointing proton) are observed, indicating a shift toward the $(BF4)_2$Cl@**2** cage complex. Precipitation was observed 24 equivalents, which is assumed to correspond to AgCl and monomeric cage **1**.

2.2 Br@2 titrations

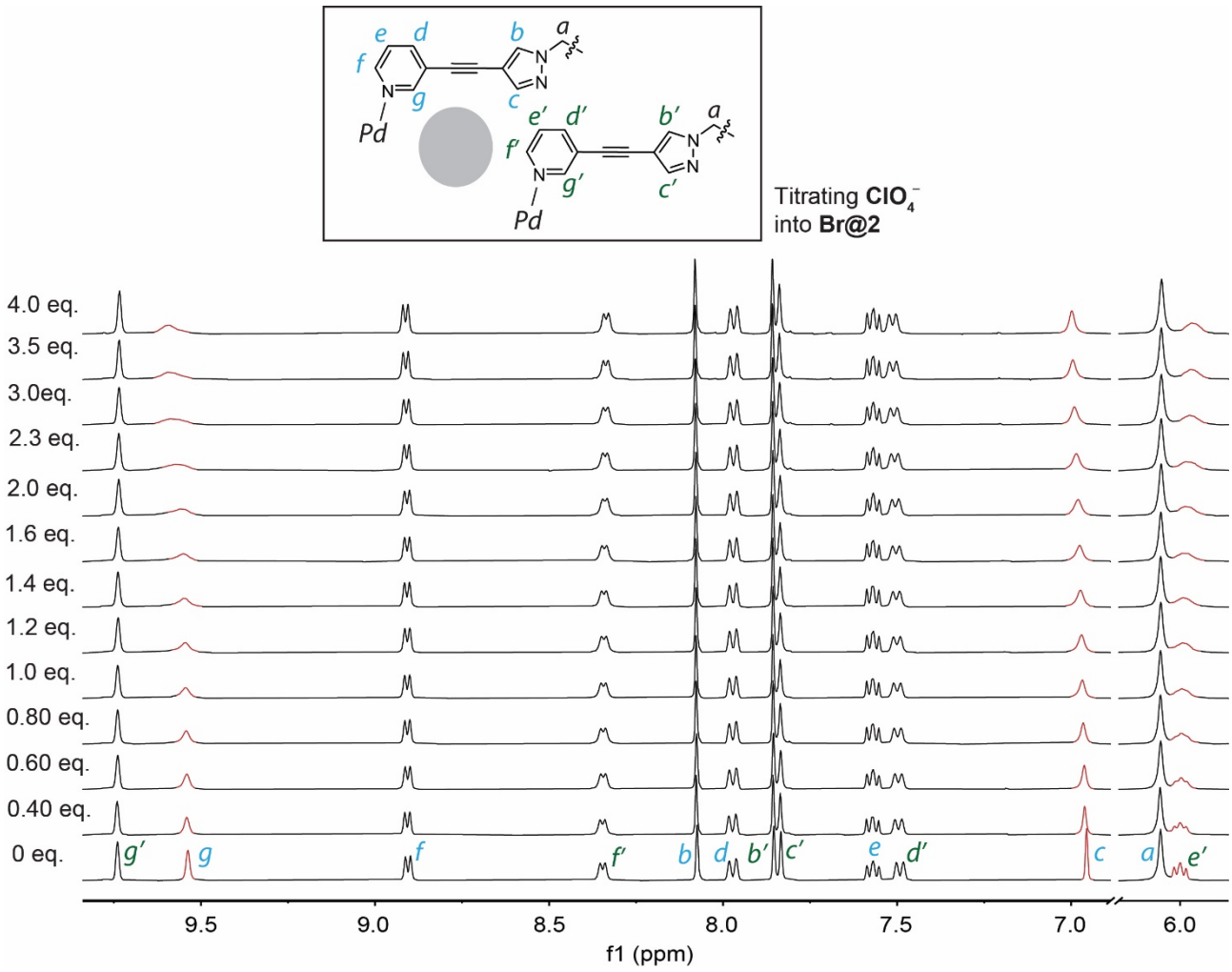

Figure S38. ^{1}H NMR spectra (600 MHz, CD_3CN, 25 °C): titration of $TBAClO_4$ into a 0.35 mM solution of Br@**2**. Shifts in g, c and e' (inside pointing protons) are observed, indicating ClO_4^- binds inside of the cage cavity (grey).

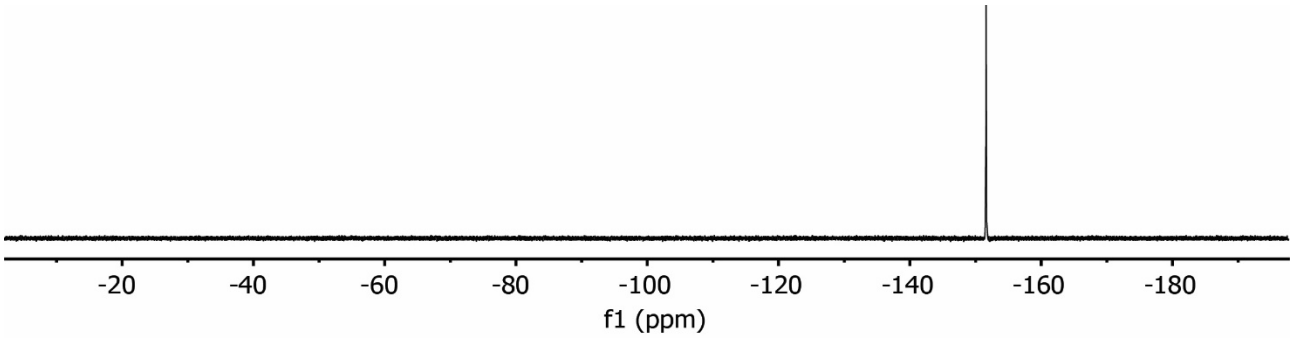

Figure S39. ^{19}F NMR spectrum (565 MHz, CD_3CN, 25 °C) titration of $TBAClO_4$ (8 equiv.) into Br@**2**. Only free BF_4^- (-151.5 ppm) was observed.

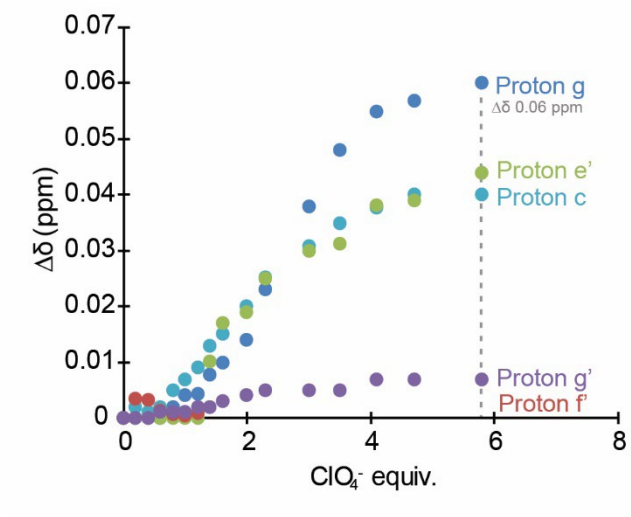

Figure S40. $TBACIO_4$ change in chemical shift graph following Br@**2** protons g, f' e' and c (inside pointing protons, outer pocket) and g' (inside pointing proton, inner pocket). g has an overall change in chemical shift of 0.06 ppm.

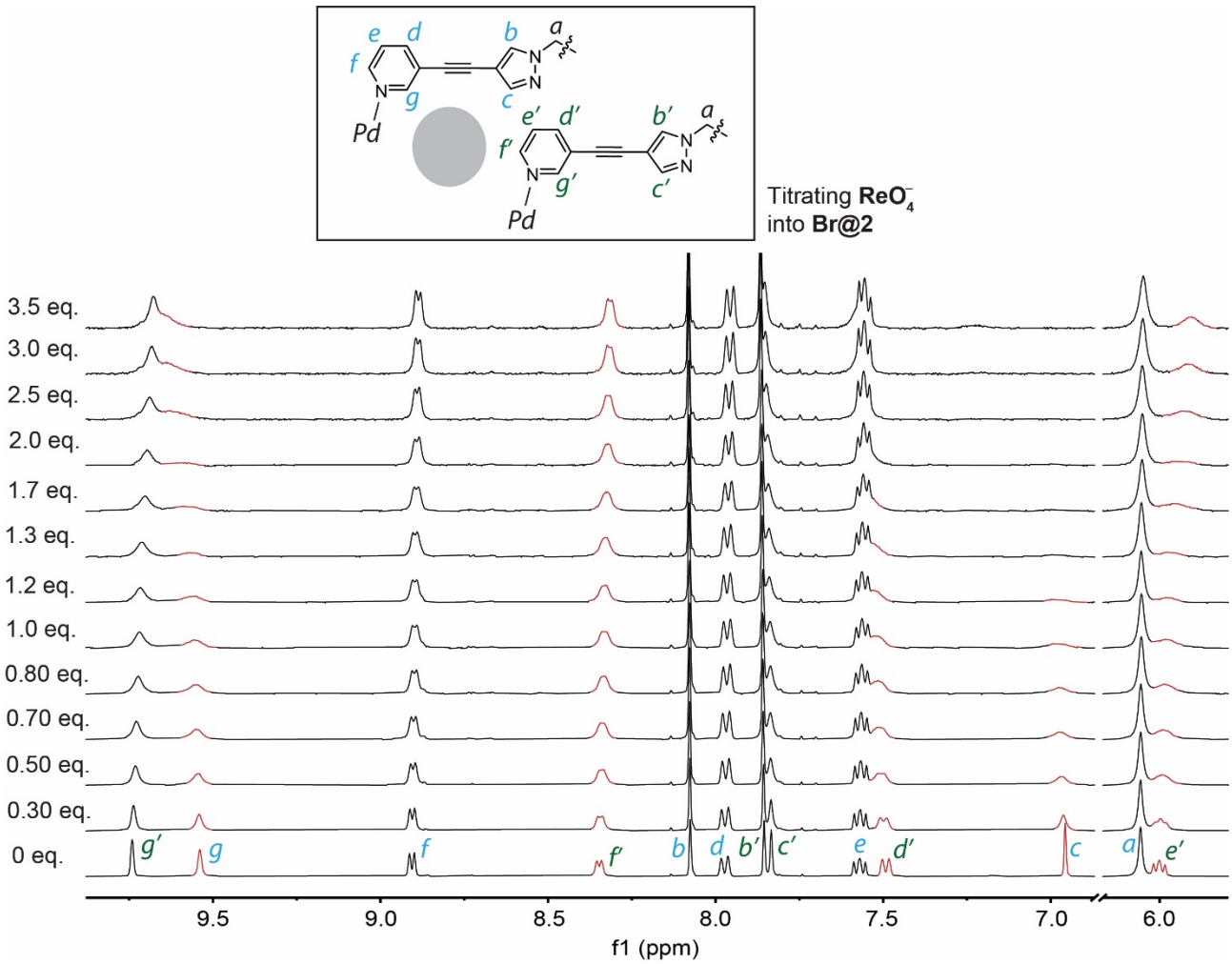

Figure S41. ^{1}H NMR spectra (600 MHz, CD_3CN, 25 °C): titration of TBAReO_4 into a 0.30 mM solution of Br@**2**. Shifts in g, f', d', e' and c (inside pointing protons) are observed, indicating ReO_4^- binds inside of the cage cavity (grey). Whilst, shifts in f, c', and e (outside pointing protons) are observed indicating that ReO_4^- binds not directly between the Pd(II) centers.

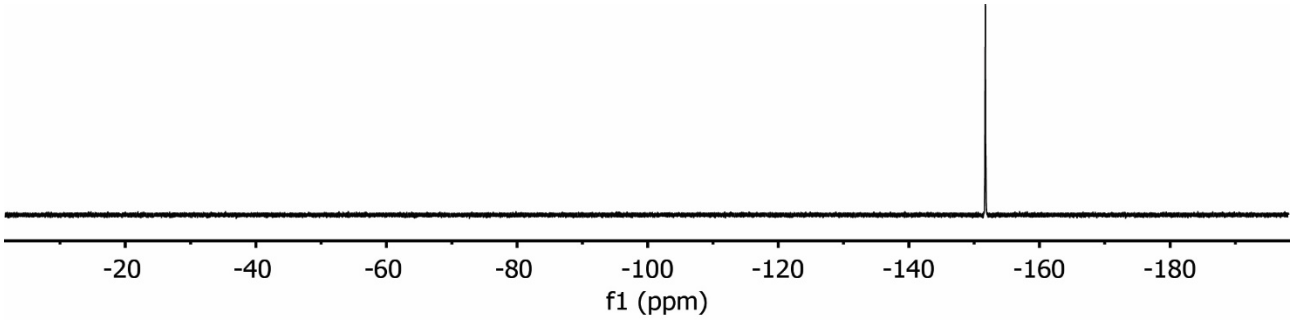

Figure S42. ^{19}F NMR spectrum (565 MHz, CD_3CN, 25 °C) titration of TBAReO_4 (14 equiv.) into Br@**2**. Only free BF_4^- (-151.5 ppm) was observed.

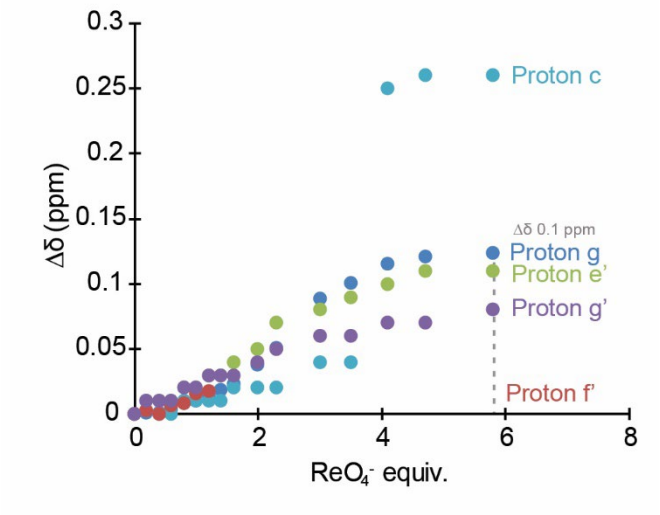

Figure S43. $TBAReO_4$ change in chemical shift graph following Br@**2** protons g, f' e' and c (inside pointing protons, outer pocket) and g' (inside pointing proton, inner pocket). g has an overall change in chemical shift of 0.1 ppm.

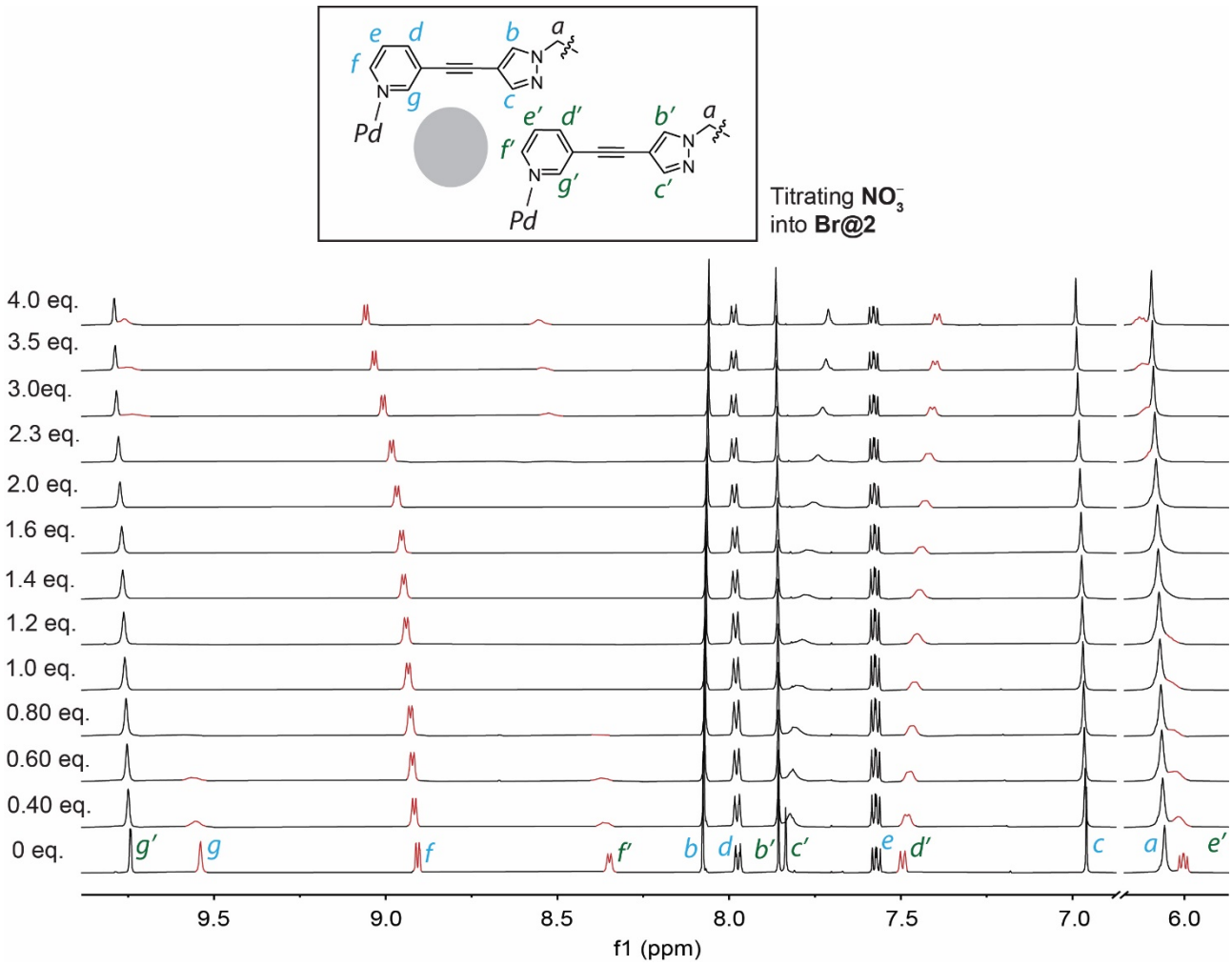

Figure S44. ^{1}H NMR spectra (600 MHz, CD_3CN, 25 °C): titration of $TBANO_3$ into a 0.35 mM solution of Br@**2**. Shifts in g, f', d' and e' (inside pointing proton) are observed, indicating NO_3^- binds inside of the cage cavity (grey). Shifts in f indicate NO_3 may also bind on the outside of the cage cavity (grey).

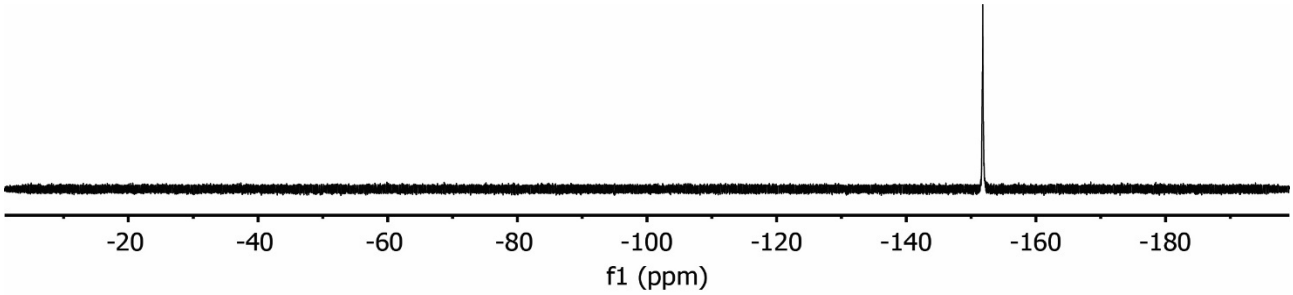

Figure S45. ^{19}F NMR spectrum (565 MHz, CD_3CN, 25 °C) titration of $TBANO_3$ (8 equiv.) into Br@**2**. Only free BF_4^- (-151.5 ppm) was observed.

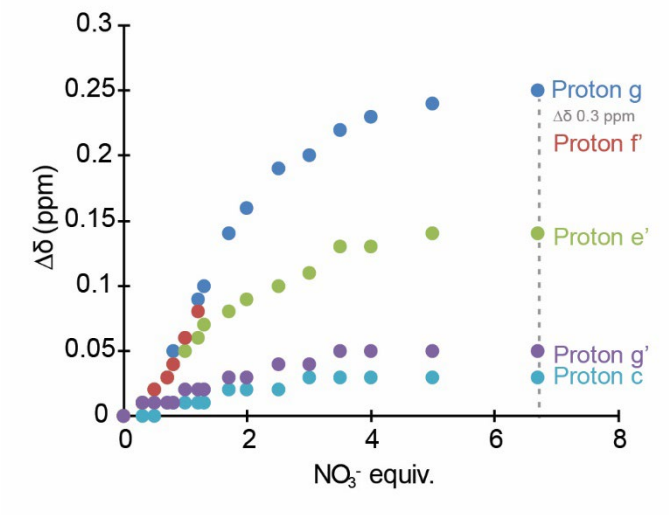

Figure S46. $TBANO_3$ change in chemical shift graph following Br@**2** protons g, f' e' and c (inside pointing protons, outer pocket) and g' (inside pointing proton, inner pocket). g has an overall change in chemical shift of 0.3 ppm.

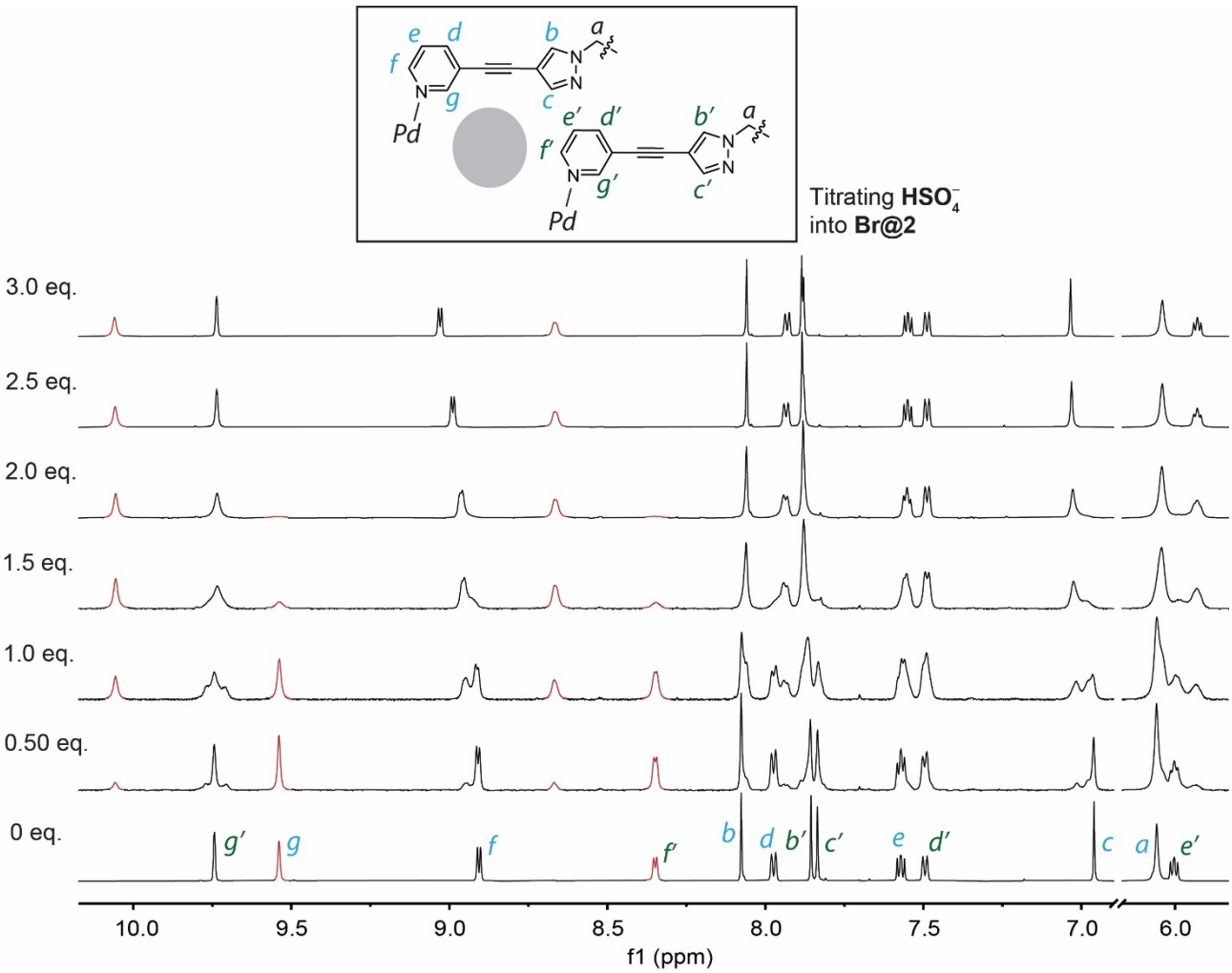

Figure S47. ^{1}H NMR spectra (600 MHz, CD_3CN, 25 °C): titration of $TBAHSO_4$ into a 0.35 mM solution of Br@**2**. Shifts in g and f' (inside pointing protons) are observed in slow exchange and indicate HSO_4^- binds inside of the cage cavity (grey). Precipitation was observed at 3.0 equivalents.

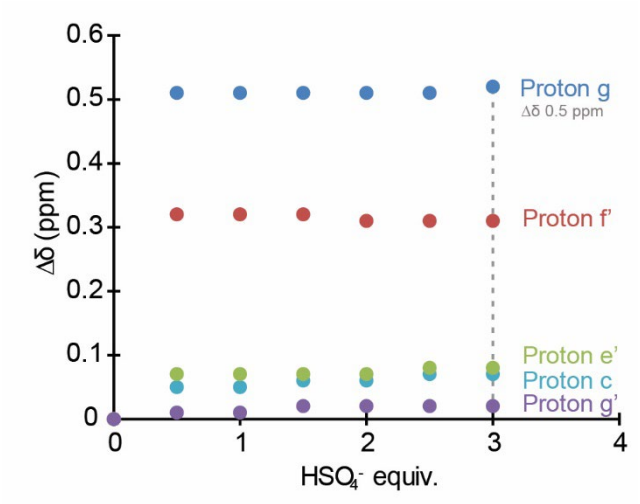

Figure S48. $TBAHSO_4$ change in chemical shift graph following Br@**2** protons g, f' e' and c (inside pointing protons, outer pocket) and g' (inside pointing proton, inner pocket). g has an overall change in chemical shift of 1.0 ppm.

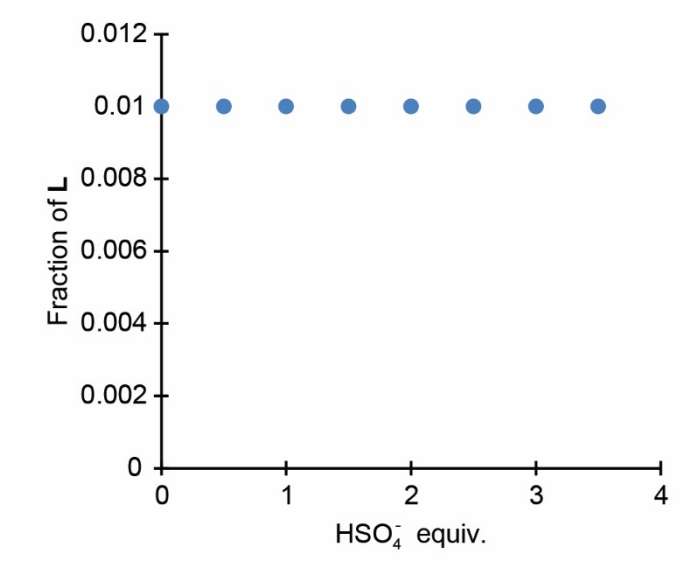

Figure S49. Fraction of residual **L** based on Br@**2** proton a integration. The integration of residual **L** does not increase with higher equivalents of $TBAHSO_4$ indicating no presence of Br@**2** decomposition.

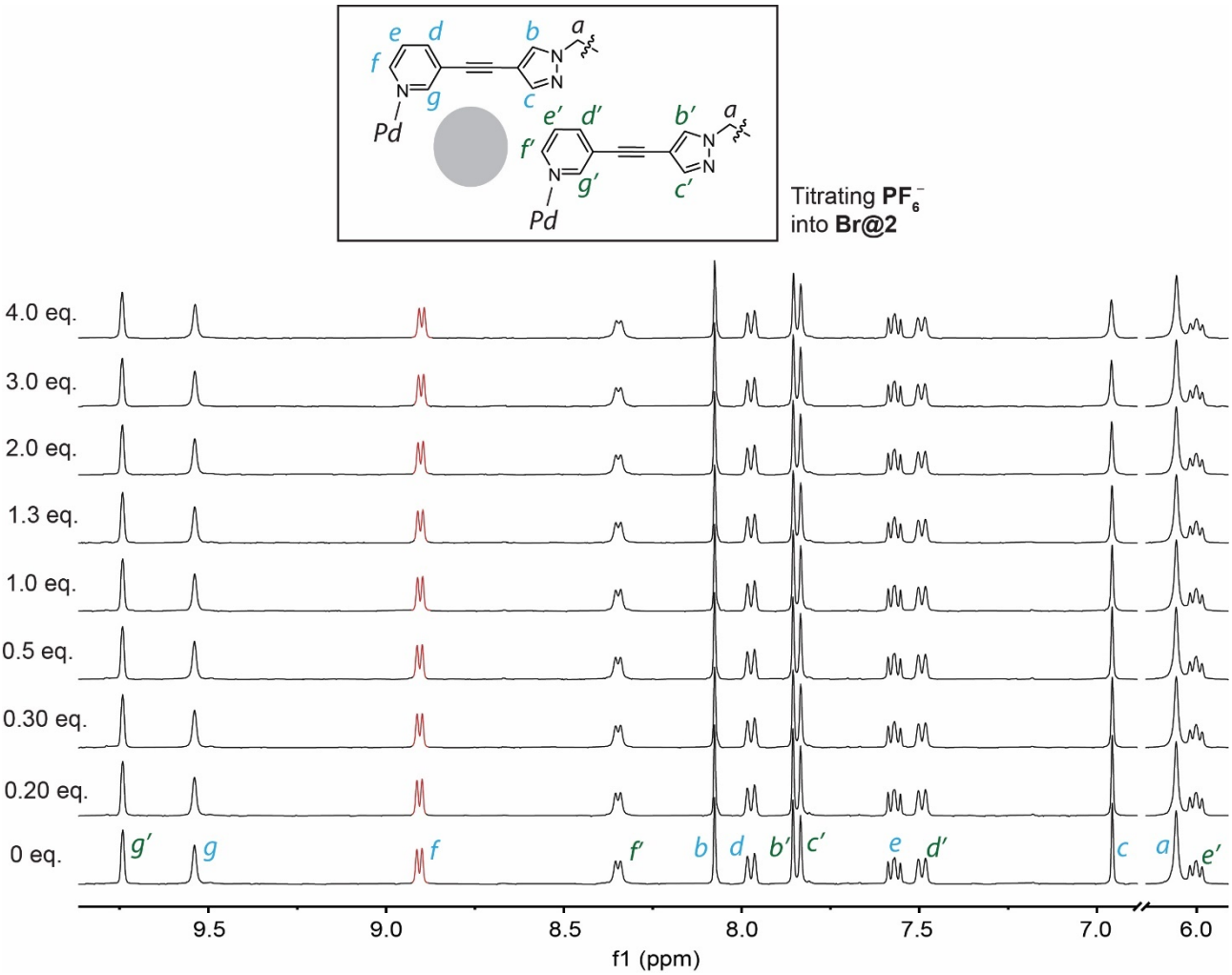

Figure S50. ^1H NMR spectra (600 MHz, CD_3CN, 25 °C): titration of $TBAPF_6$ into a 0.35 mM solution of Br@**2**. Shifts in f (outside pointing proton) are observed, and at higher equivalents. As protons g and f' (which point directly into the cavity) do not shift, the data indicates PF_6^- binds outside of the cage cavity (grey).

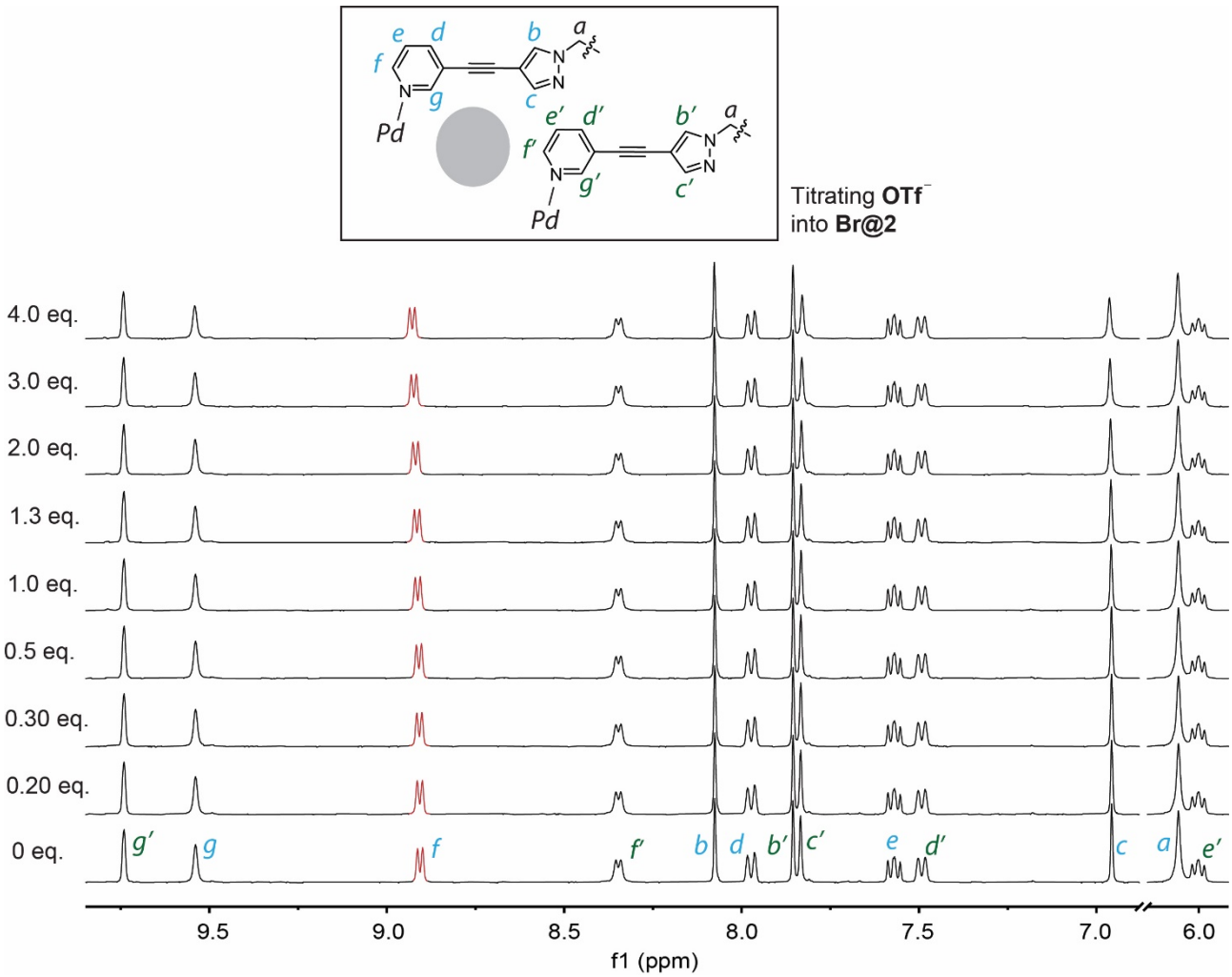

Figure S51. ^{1}H NMR spectra (600 MHz, CD_3CN, 25 °C): titration of TBAOTf into a 0.35 mM solution of Br@**2**. Shifts in f (outside pointing proton) are observed, and at higher equivalents. As protons g and f' (which point directly into the cavity) do not shift, the data indicates OTf^- binds outside of the cage cavity (grey).

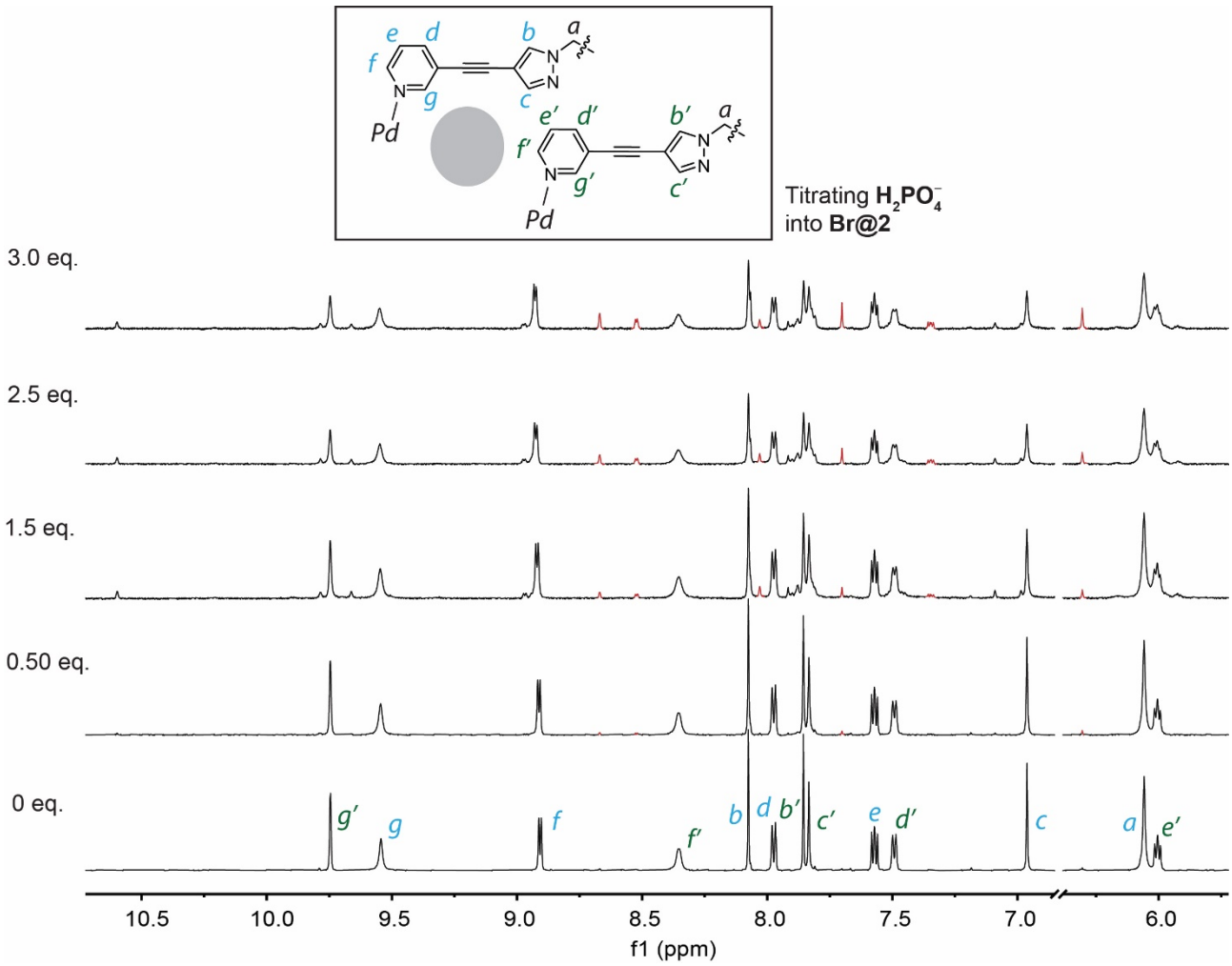

Figure S52. ^{1}H NMR spectra (600 MHz, CD_3CN, 25 °C): titration of $TBAH_2PO_4$ into a 0.35 mM solution of Br@**2**. No prominent proton shifts indicate no binding. At higher equivalents cage decomposition occurs as ligand peaks (red) increase in intensity. Precipitation was observed at 1.5 equivalents.

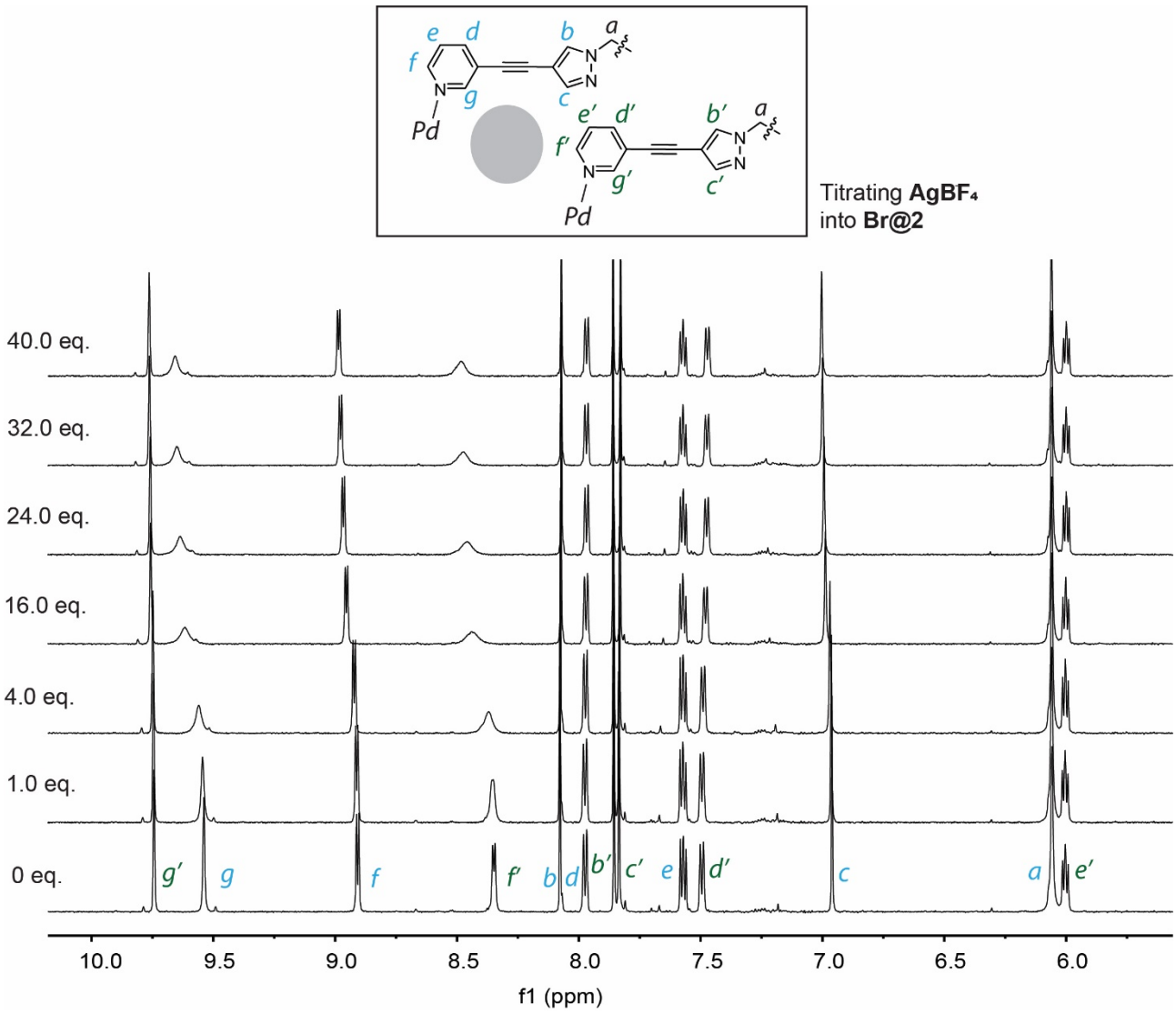

Figure S53. ^{1}H NMR spectra (600 MHz, CD_3CN, 25 °C): titration of $AgBF_4$ into a 0.35 mM solution of Br@**2**. Shifts in g (inside pointing proton) are observed, indicating a shift toward the $(BF4)_2$Br@**2** cage complex. Precipitation of AgBr was observed at 24 equivalents, which is assumed to correspond to AgBr and monomeric cage **1**.

2.3 Cl@2 and Br@2 comparison

Table S1. Guest binding experiments with Cl@**2**.

Guest[a]	Result[b]
ClO_4^-	strong inside binding K_1 = 34200±8200 M^{-1} K_2 = 1500±30 M^{-1}
ReO_4^-	strong inside binding K_1 = 11500±3900 M^{-1} K_2 = 3800±200 M^{-1}
NO_3^-	weak non-specific binding[c] K_1 = 5800±300 M^{-1} K_2 = 2100±40 M^{-1}
HSO_4^-	inside binding
PF_6^-	outside binding[d]
OTf^-	outside binding
$H_2PO_4^-$	no binding[e]
Br^-	Cage decomposition[f]
I^-	Cage decomposition

[a] Host-guest titrations were performed inside an NMR tube by titrating increasing equivalents of anion solution (as their tetra-n-butyl ammonium salts in CD_3CN, 17.5 mM) into 600 µL of a 0.27-0.32 mM solution of $[2BF_4+Cl@Pd_4L_8]^{5+}$ in CD_3CN at 25 °C.

[b] Inside binding was expressed by the shifts of the ^1H NMR signals which point into the outer cavities (H_g, $H_{f'}$, $H_{d'}$, H_c, $H_{e'}$). Proton g (points directly into the outer cavities) was used to determine values K_1 and K_2.

[c] Non-specific binding was expressed by concordant shifts of the ^1H NMR signals which point inside and outside the cage cavities.

[d] Outside binding was expressed by the shifts of the ^1H NMR signals which point outside the cage cavities (H_f, H_d, $H_{c'}$, H_e).

[e] No binding was expressed by no observable shifts in the ^1H NMR signals.

[f] Cage decomposition resulted as the intensity of free ligand ^1H NMR signals increased.

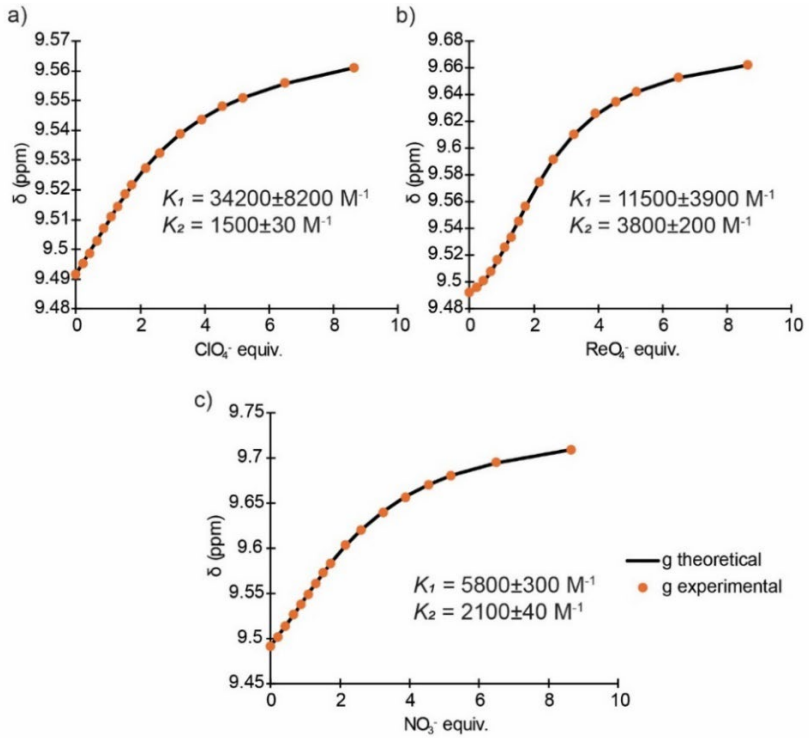

Figure S54. Bindfit 1:2 binding models of a) Cl@**2** and $TBAClO_4$, b) $TBAReO_4$ and c) $TBANO_3$ following proton g. [1,2]

Table S2. Comparison of $TBAClO_4$ guest binding between Cl@**2** and Br@**2**.

ClO_4^-	Result[a]
Cl@**2**	strong inside binding[b] K_1 = 28600±3700 M^{-1} K_2 = 1200±20 M^{-1}
Br@**2**	inside binding K_1 = 8000±2200 M^{-1} K_2 = 1700±100 M^{-1}

[a] Host-guest titrations were performed inside an NMR tube by titrating increasing equivalents of tetra-n-butyl ammonium perchlorate in CD_3CN, 17.5 mM into 600 µL of a 0.27 mM solution of $[2BF_4+Cl@Pd_4L_8]^{5+}$ in CD_3CN and a 0.35 mM solution of $[2BF_4+Br@Pd_4L_8]^{5+}$ in CD_3CN, 25 °C respectively.

[b] Inside binding was expressed by the shifts of the ^1H NMR signals which point inside the two outer cavities (H_g, $H_{f'}$, $H_{d'}$, H_c, $H_{e'}$). Proton c (points into the outer cavities) was used to determine values K_1 and K_2.

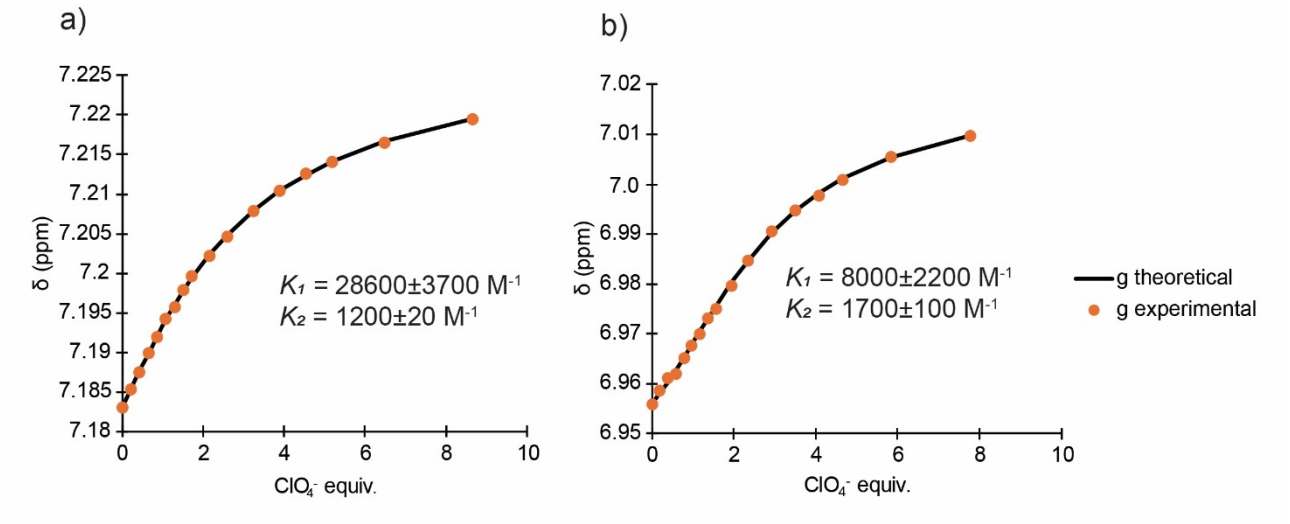

Figure S55. Bindfit 1:2 binding models of a) Cl@**2**; b) Br@**2** with $TBAClO_4$ following proton c.

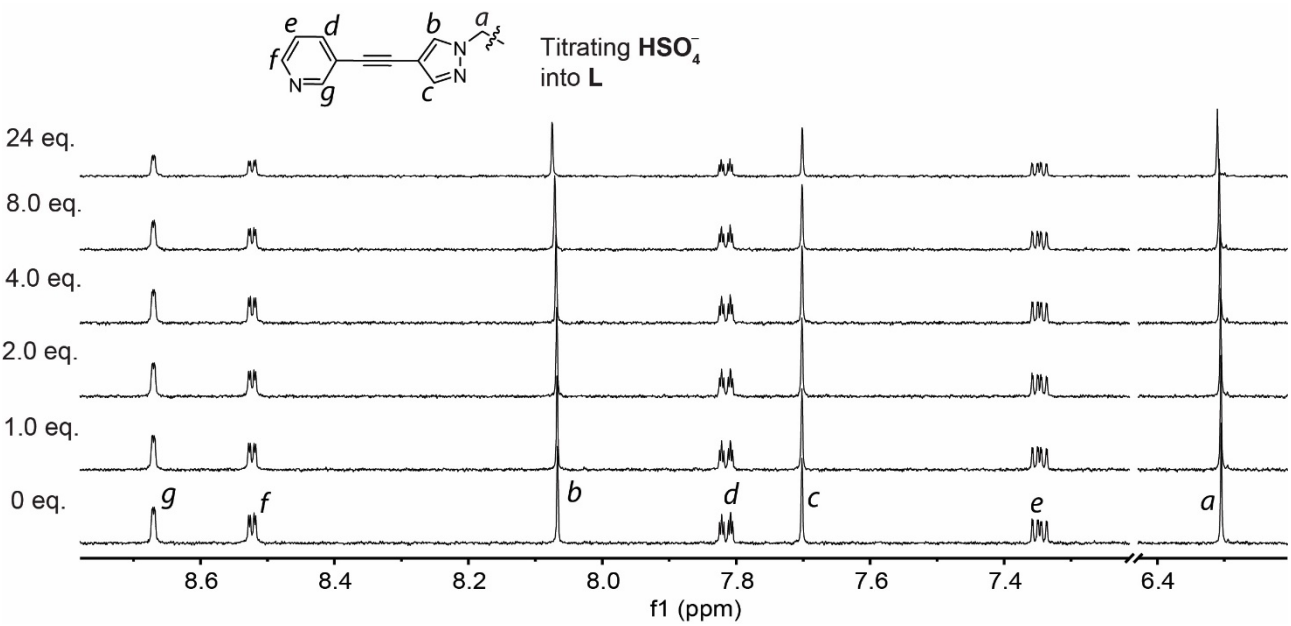

Figure S56. ^1H NMR spectra (600 MHz, CD_3CN, 25 °C): titration of $TBAHSO_4$ into a 0.35 mM solution of **L**. No prominent proton shifts indicate no protonation of the free ligand.

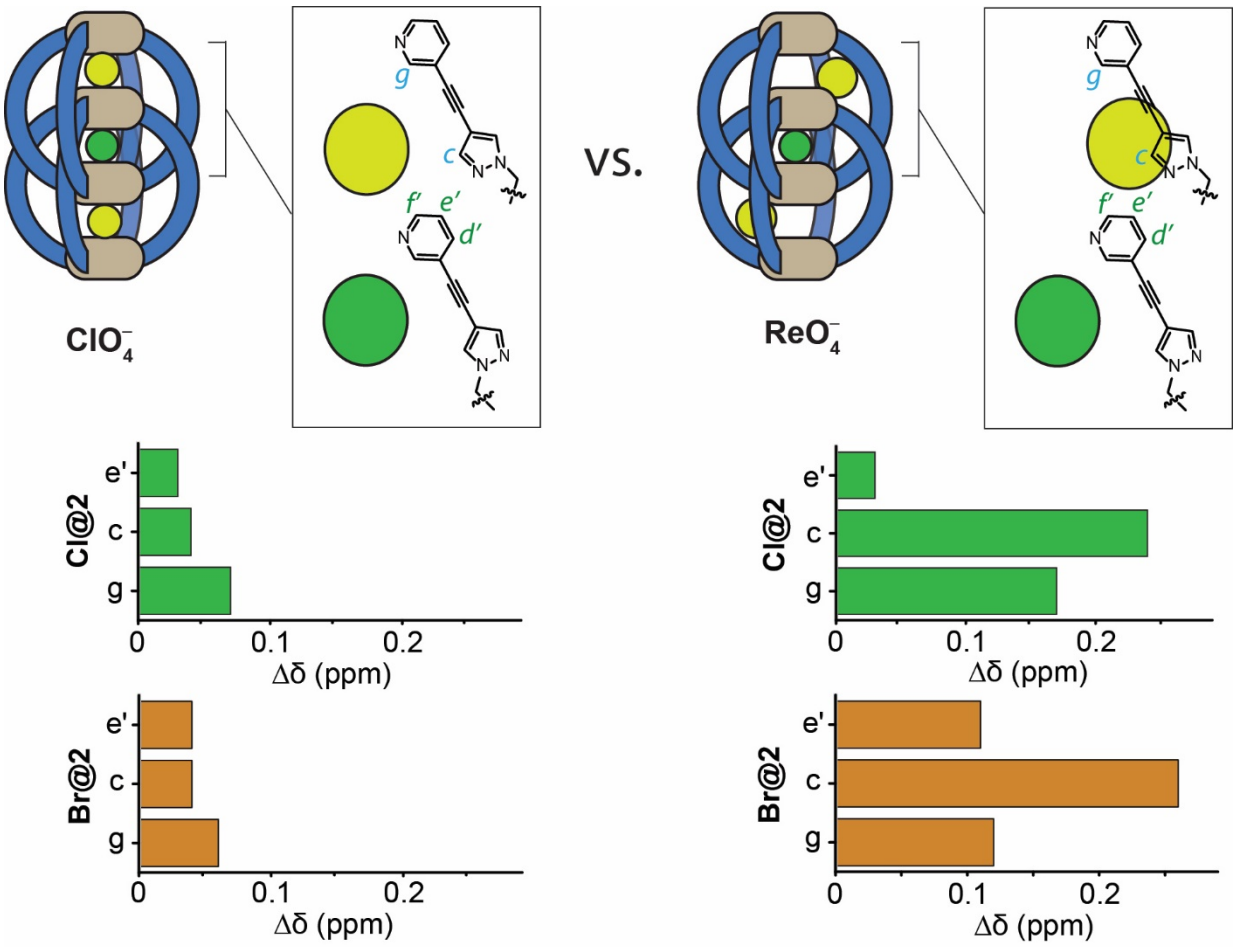

Figure S57. Anion binding modes of X@**2** with $TBAClO_4$ and $TBAReO_4$. By following the difference in chemical shift of protons g, c and e', ClO_4^- is shown to bind directly under the Pd^{II} center, whilst ReO_4^- binds towards the side of the pocket. Moreover, the later guest is expected to exchange between all four corners of the cavity, which may explain its intermediate exchange relative to the ^1H NMR timescale. With the smaller cavity offered by the Br^- template, ReO_4^- and ClO_4^- anions move even further away from proton g and affect protons c and e'.

2.4 Cl@2 and Br@2 competition studies

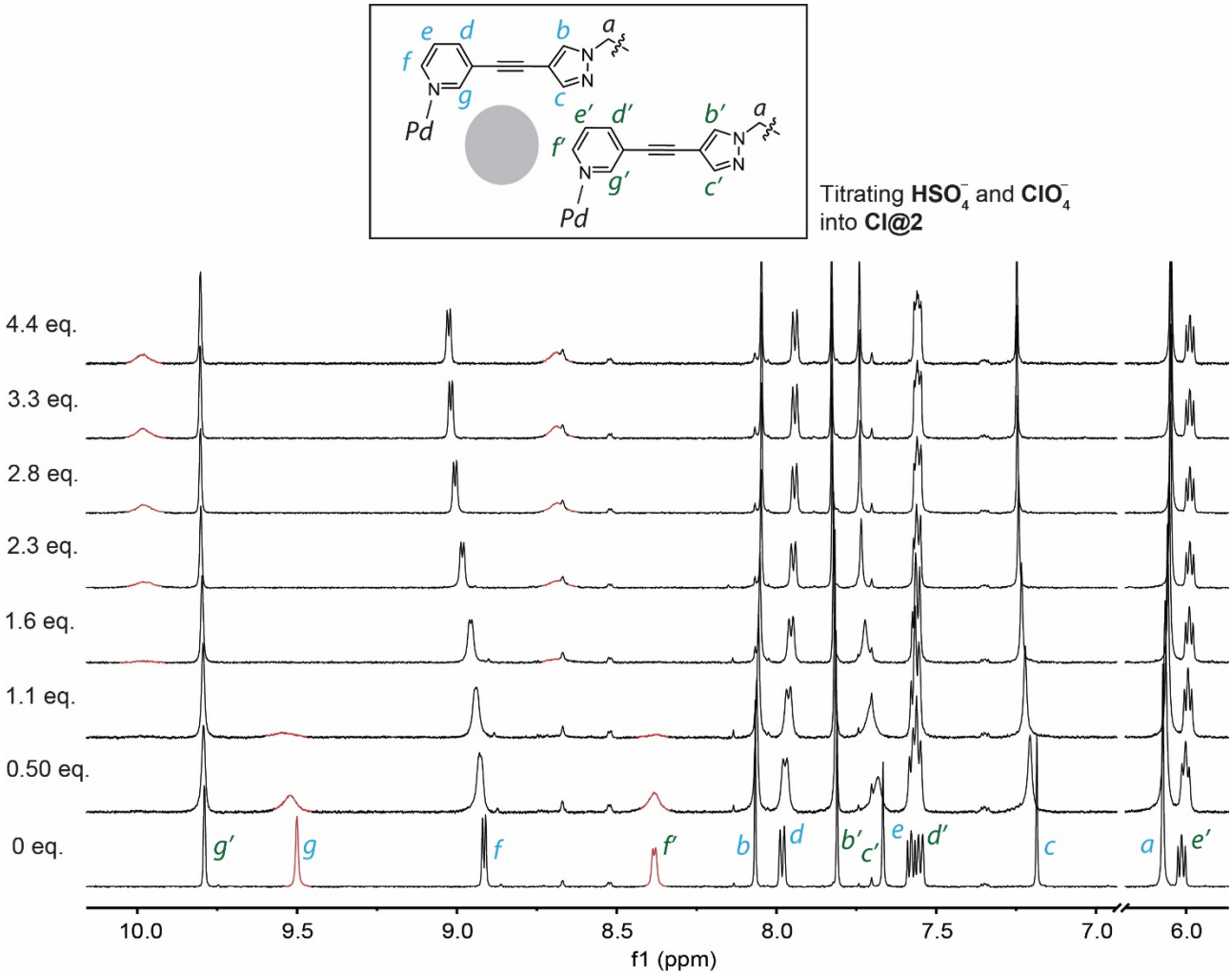

Figure S58. ^{1}H NMR spectra (600 MHz, CD_3CN, 25 °C): titration of $TBAHSO_4$ and $TBAClO_4$ into a 0.27 mM solution of Cl@**2**. Shifts in g and f' (inside pointing proton) are observed in slow exchange and indicate there is a selectivity preference for HSO_4^- over ClO_4^- as it binds inside of the cage cavity (grey).

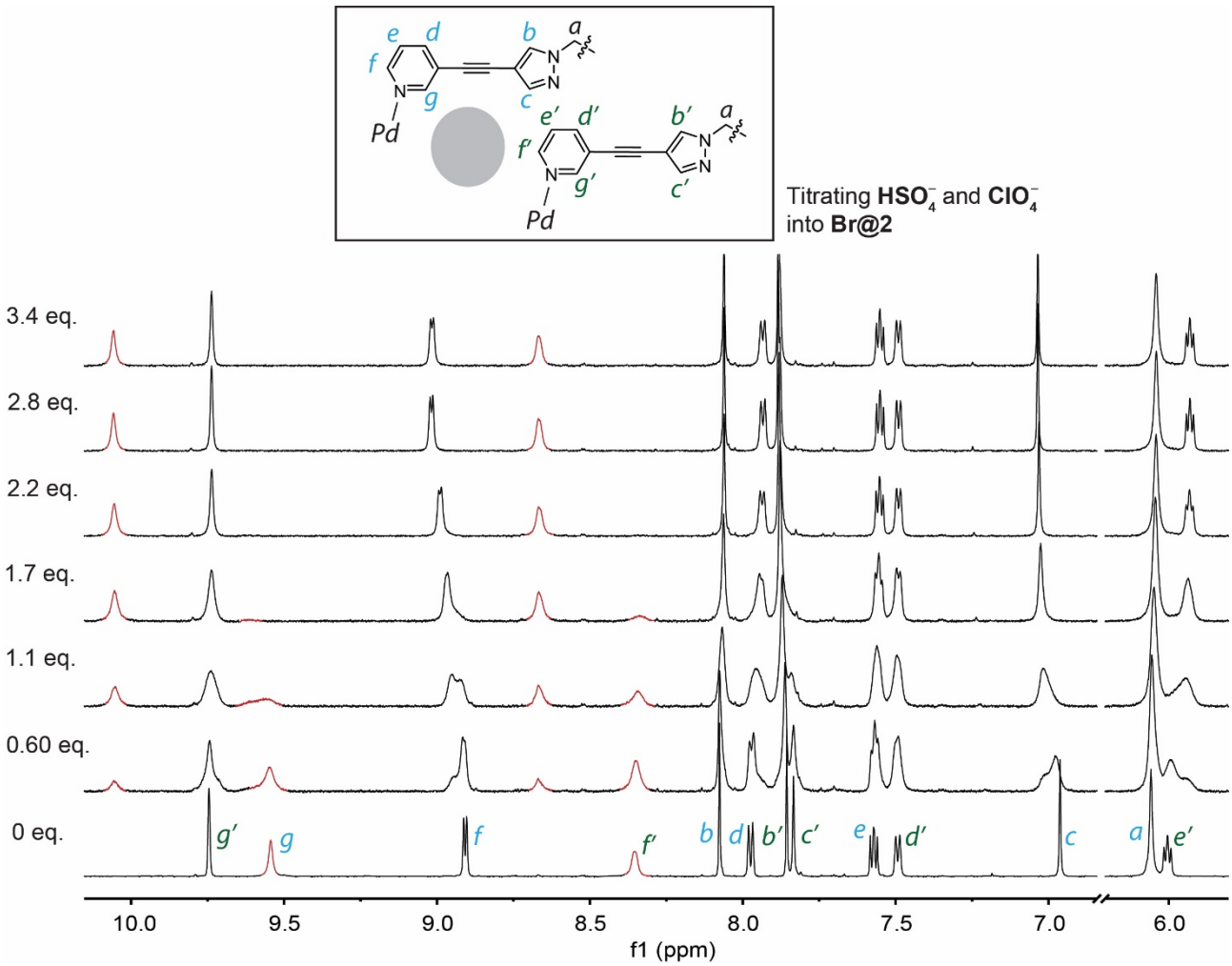

Figure S59. ^{1}H NMR spectra (600 MHz, CD_3CN, 25 °C): titration of $TBAHSO_4$ and $TBAClO_4$ into a 0.31 mM solution of Br@**2**. Shifts in g and f' (inside pointing proton) are observed in slow exchange and indicate there is a selectivity preference for HSO_4^- over ClO_4^- as it binds inside of the cage cavity (grey).

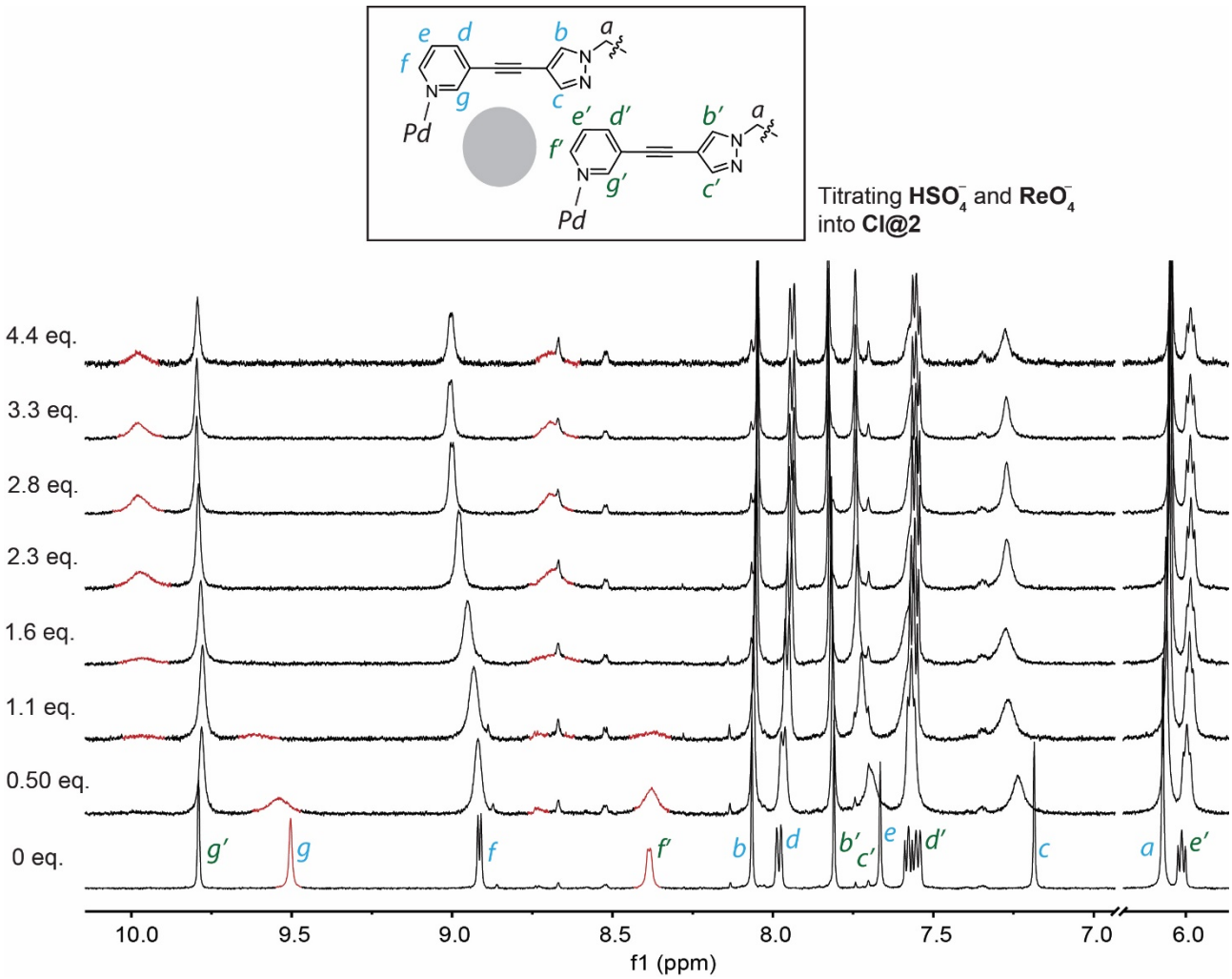

Figure S60. ^{1}H NMR spectra (600 MHz, CD_3CN, 25 °C): titration of $TBAHSO_4$ and $TBAReO_4$ into a 0.27 mM solution of Cl@**2**. Shifts in g and f' (inside pointing proton) are observed in slow exchange and indicate there is a selectivity preference for HSO_4^- over ReO_4^- as it binds inside of the cage cavity (grey).

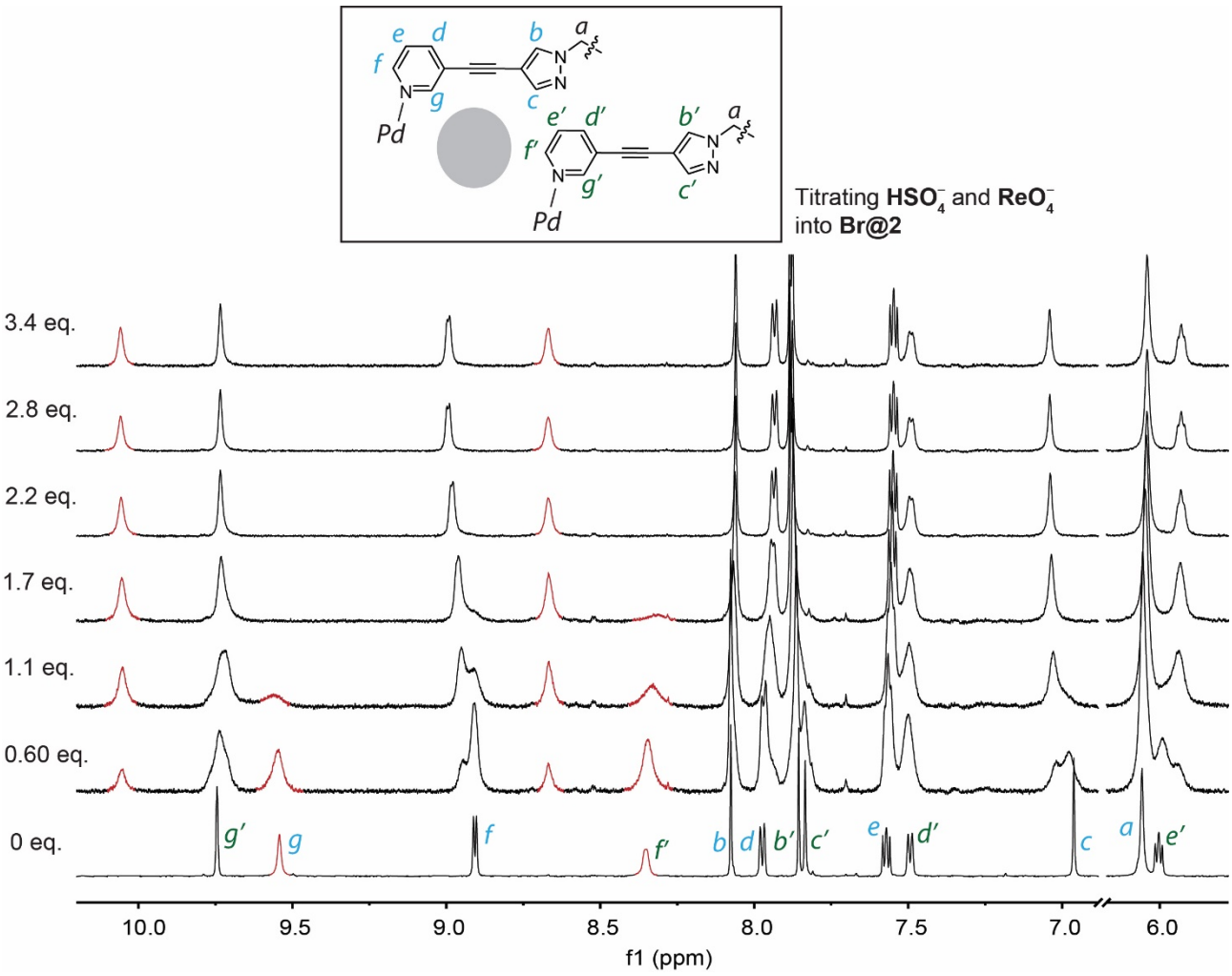

Figure S61. ^{1}H NMR spectra (600 MHz, CD_3CN, 25 °C): titration of $TBAHSO_4$ and $TBAReO_4$ into a 0.31 mM solution of Br@**2**. Shifts in g and f' (inside pointing proton) are observed in slow exchange and indicate there is a selectivity preference for HSO_4^- over ReO_4^- as it binds inside of the cage cavity (grey).

2.5 Electrospray ionization mass spectrometry (ESI-MS)

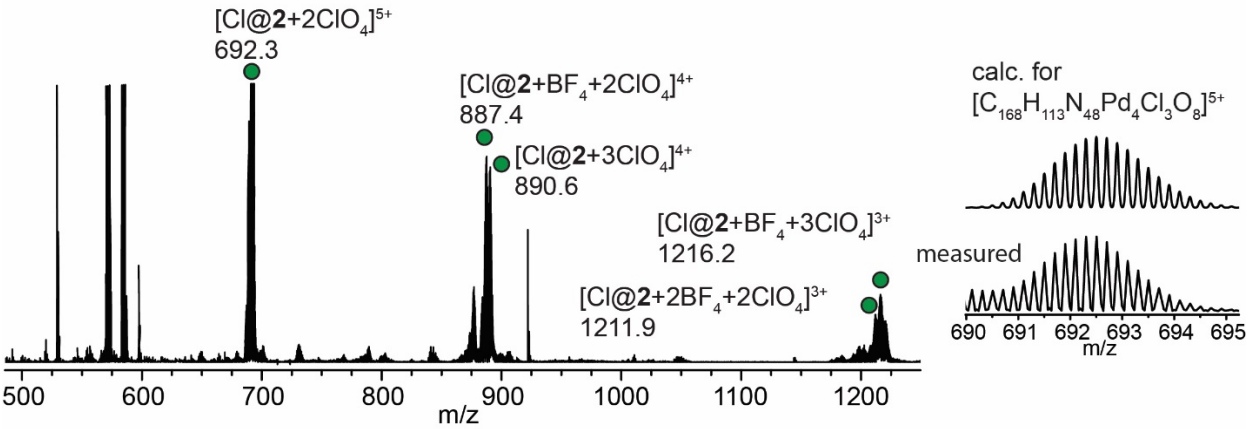

Figure S62. ESI mass spectrum of [Cl@**2**+*n*BF_4+*n*ClO_4]$^{7-n+}$ with *n* = 0–3 (green spheres).

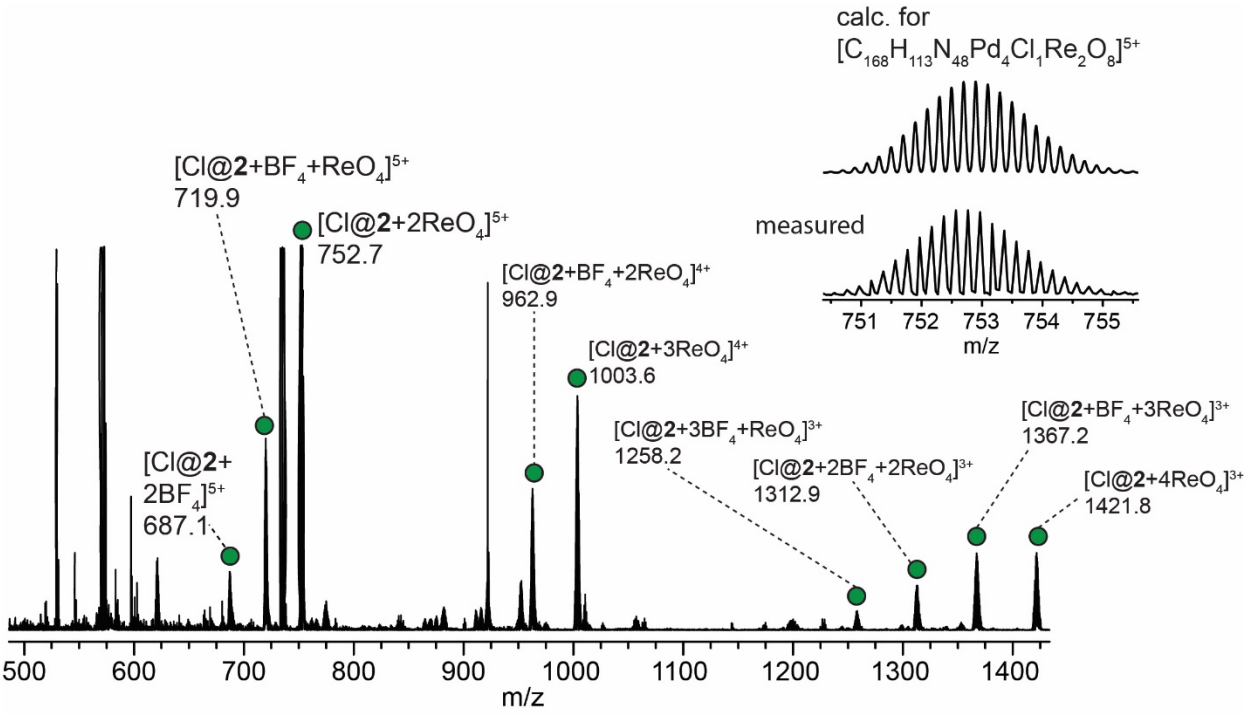

Figure S63. ESI mass spectrum of [Cl@**2**+*n*BF_4+*n*ReO_4]$^{7-n+}$ with *n* = 0–4 (green spheres).

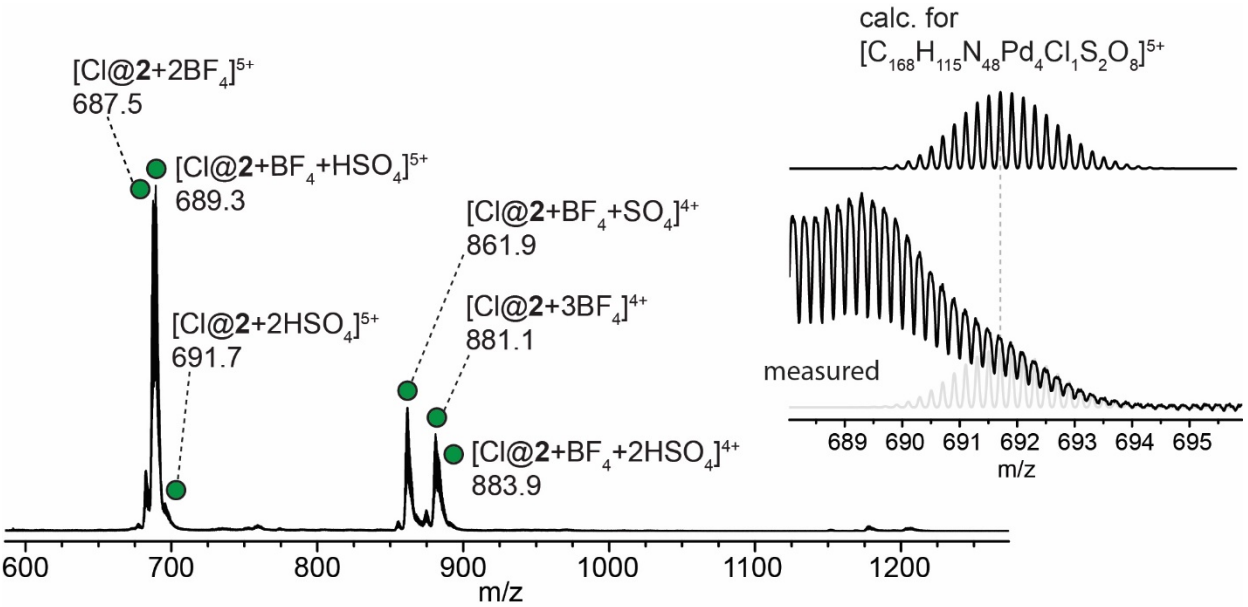

Figure S64. ESI mass spectrum of [Cl@**2**+*n*BF_4+*n*HSO_4]$^{7-n+}$ with *n* = 0–3 (green spheres).

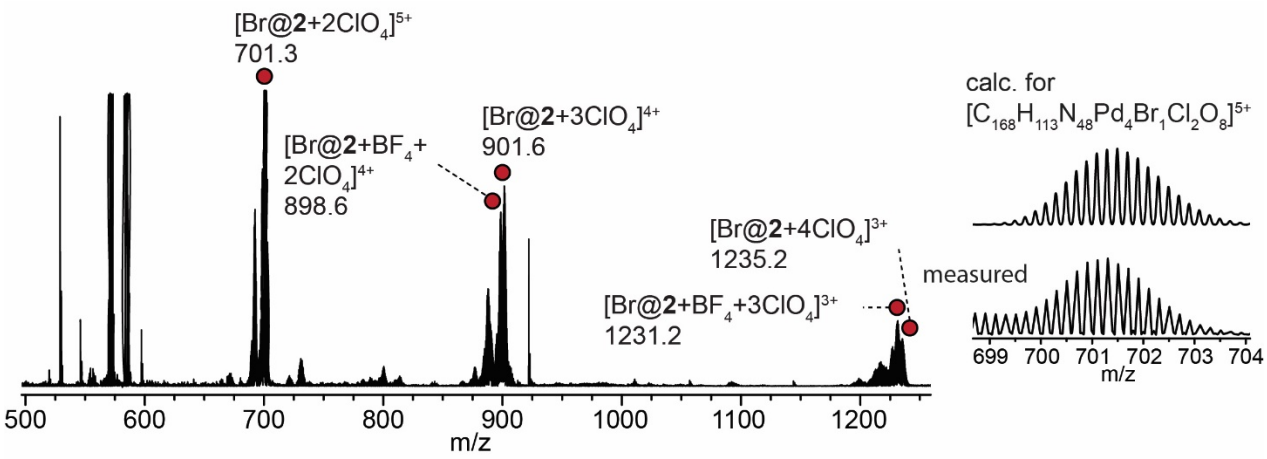

Figure S65. ESI mass spectrum of [Br@**2**+*n*BF_4+*n*ClO_4]$^{7-n+}$ with *n* = 0–4 (red spheres).

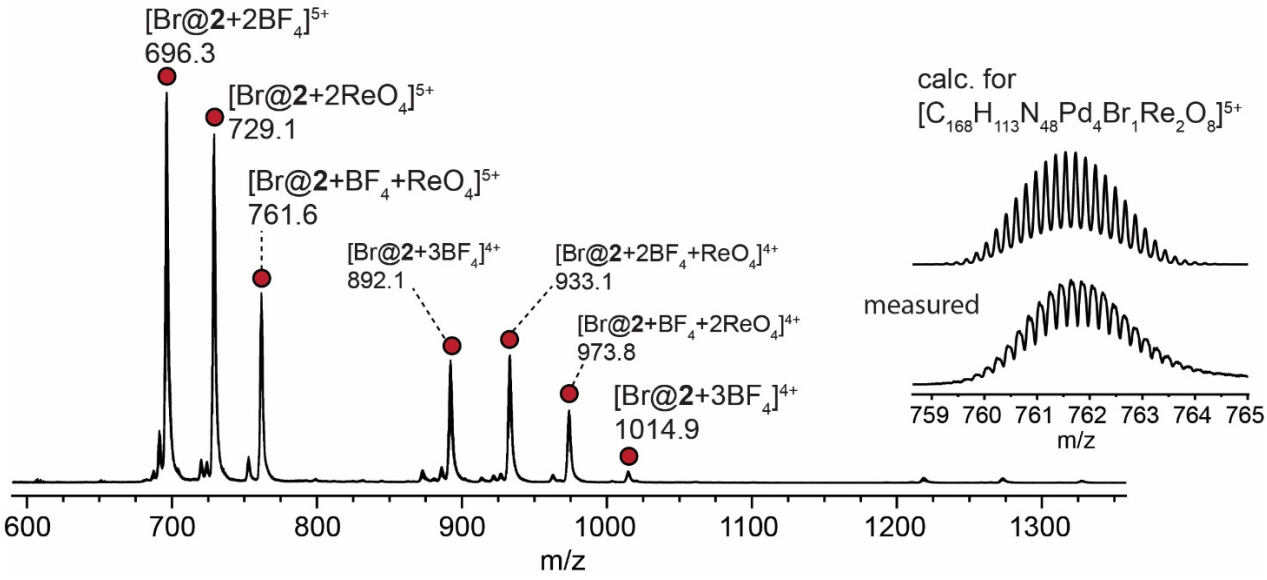

Figure S66. ESI mass spectrum of [Br@**2**+*n*BF_4+*n*ReO_4]$^{7-n+}$ with *n* = 0–3 (red spheres).

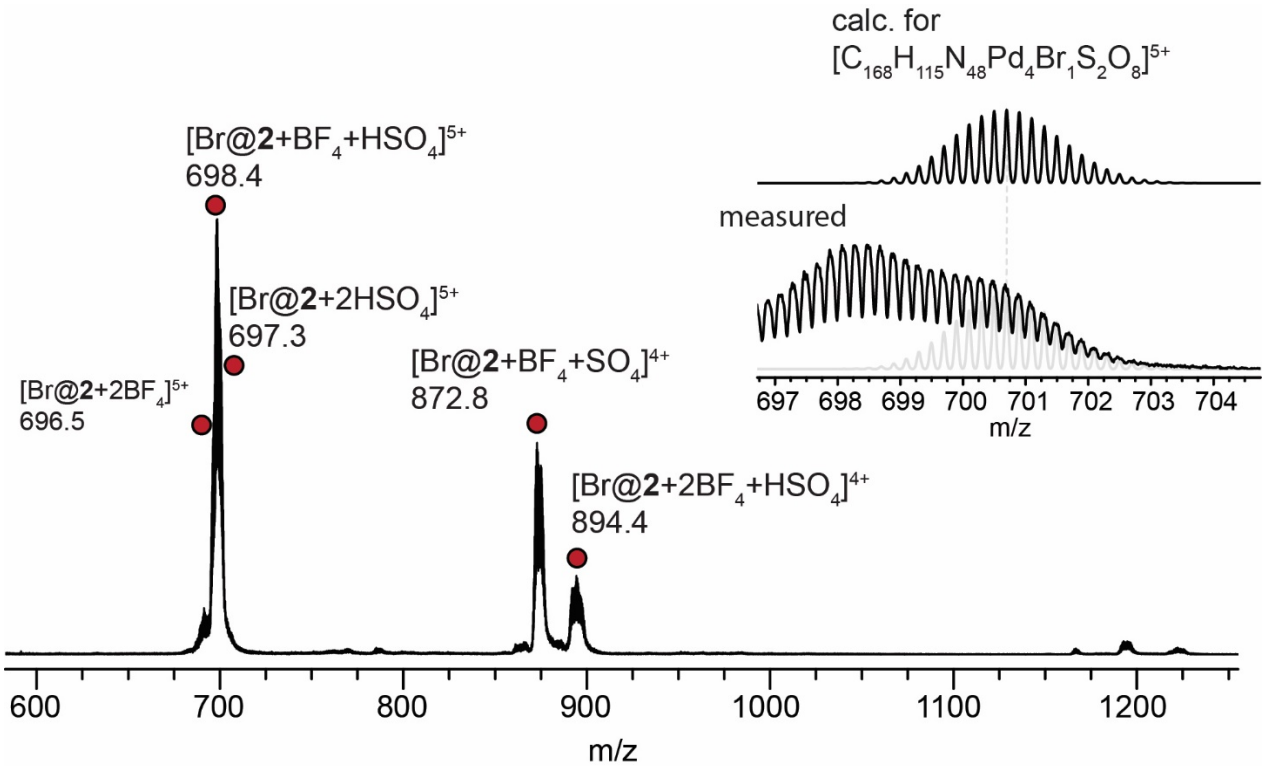

Figure S67. ESI mass spectrum of [Br@**2**+*n*BF_4+*n*HSO_4]$^{7-n+}$ with *n* = 0–2 (red spheres).

3. Isothermal titration calorimetry (ITC)

ITC analysis was performed using a TA Nano ITC instrument. Experiments were performed at 25 °C with a stirring rate of 275 rpm. 50 µL of a 2.5 mM solution of tetrabutylammonium HSO_4^- was titrated into a 250 µL of solution of X@**2** (0.21 mM). The titration comprised of 20 × 2.2 µL aliquots of the guest, with an equilibration time of 280 seconds between each point. Heats of dilution were determined in similar experiments, but 250 µL of MeCN (without X@**2** in the cell). This data was subtracted from each data set.

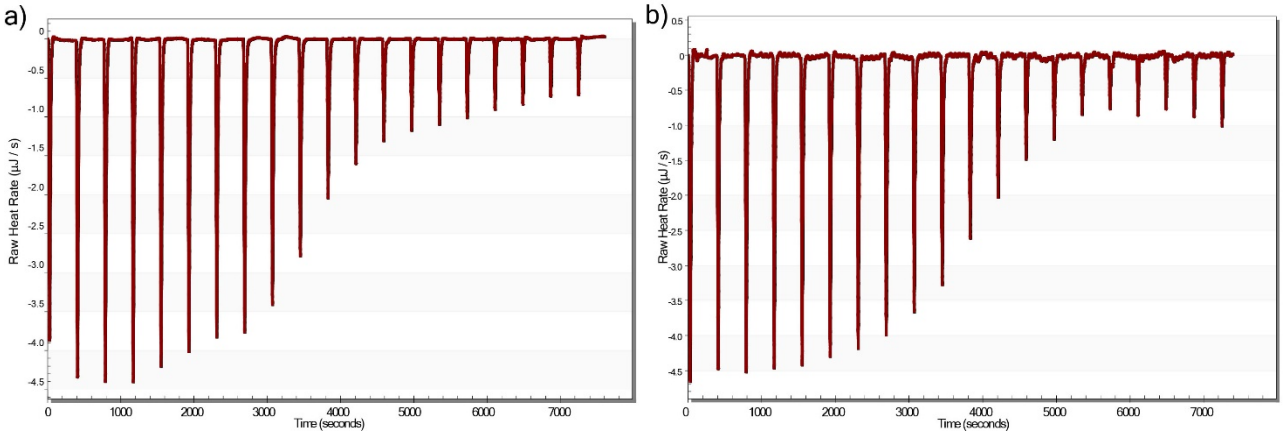

Raw ITC data for 20 injections of HSO_4^- (guest) to a) Cl@**2** and b) Br@**2**.

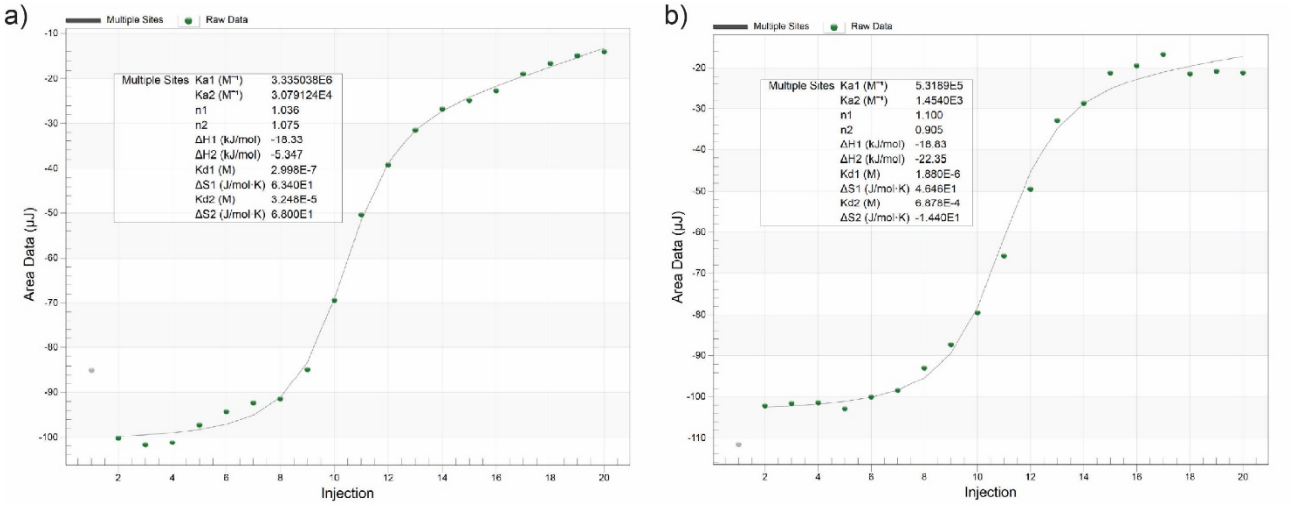

Figure S68. Cumulative heat (area) of the injectant (HSO_4^-) and fitting results for a) Cl@**2** and b) Br@**2**. The line represents the best fit resulting from fitting using the multiple-sites model.

4. X-ray crystallography

4.1 X-ray data

Crystals of **L** and cage **1** were obtained by allowing a 0.7 mM CD_3CN solution to stand for 3 days. Crystals of Cl@**2**, Br@**2** and $(ClO_4)_2$Cl@**2** were obtained by slow-vapor diffusion of chloroform into a 0.35 mM CD_3CN solution of the cage. Single crystals were mounted in paratone-N oil on a plastic loop. X-ray diffraction data for **L**, **1**, Cl@**2**, Br@**2** and $(ClO_4)_2$Cl@**2** were collected at 100(2) K on the MX-1 or MX-2 beamline of the Australian Synchrotron (λ = 0.7107 Å).[3,4]

For **1**, Cl@**2**, Br@**2** and $(ClO_4)_2$Cl@**2**, a series of macromolecular refinement techniques were carefully adapted and employed to facilitate structure refinement and molecular model building. These methods have already proved successful in previous cases involving large and complicated supramolecular structures with high solvent content.[5,6] Where applicable, Organic ligands, anions and solvents were grouped into residues to enable addressing all of the atoms of repeating structural fragments with a single command. Stereochemical restraint dictionaries were generated using GRADE.[7] GRADE is part of BUSTER and was accessed via the GRADE Web Server. Its dictionaries for SHELXL contain target values and standard deviations for 1,2-distances (DFIX) and 1,3-distances (DANG), as well as restraints for planar groups (FLAT).

All structures were solved by direct methods using SHELXT[8] and refined with SHELXL[9] and ShelXle[10] as a graphical user interface. All non-hydrogen atoms were refined anisotropically and hydrogen atoms were included as invariants at geometrically estimated positions. The refinement of ADP's for carbon, nitrogen and oxygen atoms was supported by similarity restraints (SIMU) and and enhanced rigid bond restraints (RIGU) in the SHELXL program.[11] X-ray experimental data is given in Table S3 and S4.

*4.1.1. Special refinement details for **1***

The ligands, tetrafluoroborate anions and MeCN solvent molecules were grouped into residues to address all of the atoms of repeating structural fragments with a single command. Stereochemical restraint dictionaries for the BF_4^- (BF4) anions and MeCN (ACN) molecules were generated using GRADE.[7] In general, the disorder of the BF_4^- and MeCN molecules was modelled over two positions. The contribution of the electron density from disordered, pore-bound solvent molecules, which could not be adequately modelled with discrete atomic positions were handled using the SQUEEZE[12] routine in PLATON,[13] which strongly improved all figures of merit (FOM). A combined platon_squeeze_void_count_electrons of 482 was assigned to 11 MeCN molecules of solvent content per formula unit.

The data was originally integrated in the triclinic unit cell 16.859, 16.883, 16.870, 88.10, 60.18, 60.26 and later transformed into higher metric symmetry using xprep. The chosen unit cell was monoclinic C2/m, achieved with the following transformation matrix: 0.0000, 1.0000 1.0000 0.0000 1.0000 -1.0000 -1.0000 0.0000. After inspection of the data with PLATON, the following unit cell was recommended by the ADDSYMM function: 16.859, 23,453, 17.529, 90, 90.35, 90. This unit cell produced a more stable refinement. However, re-integration of the raw data with this unit cell was not possible due to the loss of the raw data set and difficulties in reproducing the growth of crystal single-crystals large enough for re-collecting the data".

*4.1.2. Special refinement details for Cl@**2***

Organic ligands, anions and solvents were grouped into residues to address all of the atoms of repeating structural fragments with a single command. Stereochemical restraint dictionaries for the ligand (LIG), chloroform (CHL) and BF_4^- (BF4) anions were generated using GRADE.[7] The disorder of the pyridine rings of the ligand was modelled over two positions. The disorder of the BF_4^- anions was modeled over two or four positions. The contribution of the electron density from disordered, pore-bound solvent molecules, which could not be adequately modelled with discrete atomic positions were handled using the SQUEEZE[12] routine in PLATON,[13] which strongly improved all figures of merit (FOM). A combined platon_squeeze_void_count_electrons of 2766 was assigned to 20 $CHCl_3$ + 10 MeCN molecules of solvent content per formula unit.

As a result of the poor data quality, some BF_4^- anions possess bond lengths short bond lengths (e.g., B1_5 F2_5 = 1.33 Å), despite the application of restraints. Despite the poor quality data, we have attempted to model as many of the disordered BF_4^- and chloroform molecules as possible. This has resulted in a GoF of 1.605 which is not ideal in small molecule terms, but density maps suggest a good agreement of the observed electron density and the molecular model.

*4.1.3. Special refinement details for Br@**2***

Organic ligands, anions, and solvents were grouped into residues to address all of the atoms of repeating structural fragments with a single command. Stereochemical restraint dictionaries for the ligand (LIG), chloroform (CHL) and BF_4^- (BF4) anions were generated using GRADE.[7] The disorder of the pyridine rings of the ligand was modelled over two positions. The disorder of the BF_4^- anions was modeled over two or four positions. The contribution of the electron density from disordered, pore-bound solvent molecules, which could not be adequately modelled with discrete atomic positions were handled using the SQUEEZE[12] routine in PLATON,[13] which strongly improved all figures of merit (FOM). A combined platon_squeeze_void_count_electrons of 1596 was assigned to 5 $CHCl_3$ + 5 MeCN molecules of solvent content per formula unit.

*4.1.4. Special refinement details for $(ClO_4)_2Cl$@**2***

Organic ligands and ClO_4^- and BF_4^- anions were grouped into residues to enable addressing all of the atoms of repeating structural fragments with a single command. Stereochemical restraint dictionaries for the ligand (LIG) and ClO_4^- (CLO) and BF_4^- (BF4) anions were generated using GRADE.[7] The disorder of the pyridine rings of the ligand was modelled over two positions. The disorder of 3 of the 4 oxygen atoms of one ClO_4^- was modelled over two positions. Another ClO_4^-, was found to be partially occupied with the second part being a BF_4^- anion. Since the compound was obtained by anion exchange of the BF_4^- cage with ClO_4^-, this model is entirely reasonable. The contribution of the electron density from disordered, pore-bound solvent molecules, which could not be adequately modelled with discrete atomic positions were handled using the SQUEEZE[12] routine in PLATON,[13] which strongly improved all figures of merit (FOM). A combined platon_squeeze_void_count_electrons of 1016 was assigned to 3.5 $CHCl_3$ + 3 MeCN + 0.25 H_2O molecules of solvent content per formula unit.

Table S3. Crystallographic information for **L**, **1** and Cl@**2**.

Compound	**L**	**1**	Cl@**2**
CCDC number	2372761	2372762	2372764
Empirical formula	$C_{21}H_{14}N_6$	$C_{122}H_{113}B_3F_{12}N_{43}Pd_2$	$C_{379}H_{277}B_{14}Cl_{71}F_{56}N_{106}Pd_8$
Formula weight	350.38	2654.78	10899.54
Crystal system	Monoclinic	Monoclinic	Orthorhombic
Space group	C2/c	I2/m	Pbcn
a (Å)	20.740(4)	16.859(3)	14.916(3)
b (Å)	4.4250(9)	23.453(5)	27.009(5)
c (Å)	18.376(4)	17.529(10)	58.190(12)
α (º)	90	90	90
β (º)	94.79(3)	90.35(3)	90
γ (º)	90	90	90
Volume (Å^3)	1680.5(6)	6931(4)	23443(8)
Z	4	2	2
Density (calc.) (Mg/m^3)	1.385	1.272	1.544
Absorption coefficient (mm^{-1})	0.088	0.337	0.790
F(000)	728	2722	10884

Crystal size (mm^3)	0.17 x 0.05 x 0.04	0.18 x 0.10 x 0.04	0.06 x 0.05 x 0.02
θ range for data collection (º)	1.971 to 31.902	1.450 to 29.004	1.400 to 25.093
Reflections collected	13396	41441	231293
Observed reflections [R(int)]	2449 [0.1128]	7114 [0.0549]	20739 [0.1053]
Goodness-of-fit on F^2	1.093	0.984	1.605
R_1 [$I>2\sigma(I)$]	0.0608	0.0534	0.1212
wR_2 (all data)	0.1800	0.1629	0.4229
Largest diff. peak and hole (e.Å-3)	0.366 and -0.333	1.530 and -0.875	1.115 and -1.132
Data / restraints / parameters	2410 / 0 / 124	7114 / 730 / 515	20739 / 3935 / 1557

Table S4. Crystallographic information for Br@**2** and $(ClO_4)_2Cl$@**2.**

Compound	Br@**2**	$(ClO_4)_2Cl$@**2**
CCDC number	2372763	2386148
Empirical formula	$C_{187}H_{136}B_7BrCl_{27}F_{28}N_{53}Pd_4$	$C_{182}H_{130}BCl_{27}F_4N_{51.5}O_{20.25}Pd_4$
Formula weight	5195.81	4831.93
Crystal system	Orthorhombic	Orthorhombic
Space group	Ccc2	Pbcn
a (Å)	14.864(3)	14.977(3)
b (Å)	57.355(12)	27.843(6)
c (Å)	27.051(5)	49.372(10)
α (º)	90	90
β (º)	90	90
γ (º)	90	90
Volume ($Å^3$)	23062(8)	20588(7)
Z	4	4
Density (calc.) (Mg/m^3)	1.496	1.559
Absorption coefficient (mm^{-1})	0.876	0.773
F(000)	10376	9714
Crystal size (mm^3)	0.18 x 0.11 x 0.08	0.17 x 0.13 x 0.04
θ range for data collection (º)	0.710 to 23.256	1.463 to 26.373
Reflections collected	108068	240907
Observed reflections [R(int)]	16236 [0.0415]	20587 [0.1310]
Goodness-of-fit on F^2	1.073	1.039
R_1 [$I>2\sigma(I)$]	0.0797	0.0949
wR_2 (all data)	0.2540	0.3166
Largest diff. peak and hole (e.Å-3)	1.695 and -0.583	1.519 and -1.032
Data / restraints / parameters	16236 / 4161 / 1733	20587 / 2919 / 1369

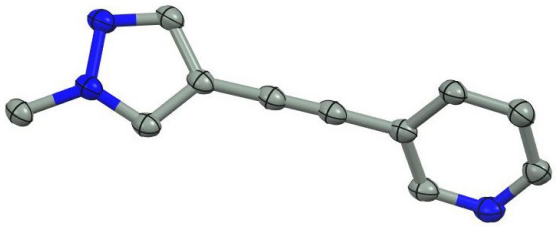

Figure S69. The asymmetric unit of the X-ray structure of **L** with all non-hydrogen atoms shown as ellipsoids at the 50% probability level.

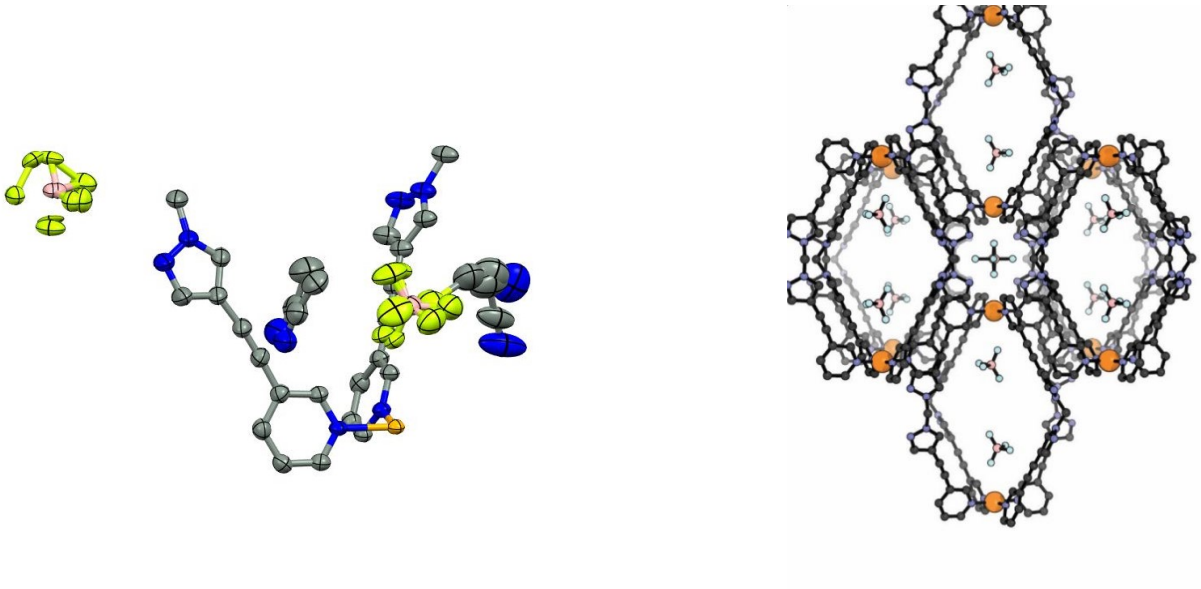

Figure S70. Left: The asymmetric unit of the X-ray structure of **1** with all non-hydrogen atoms shown as ellipsoids at the 50% probability level; right: crystal packing of **1**.

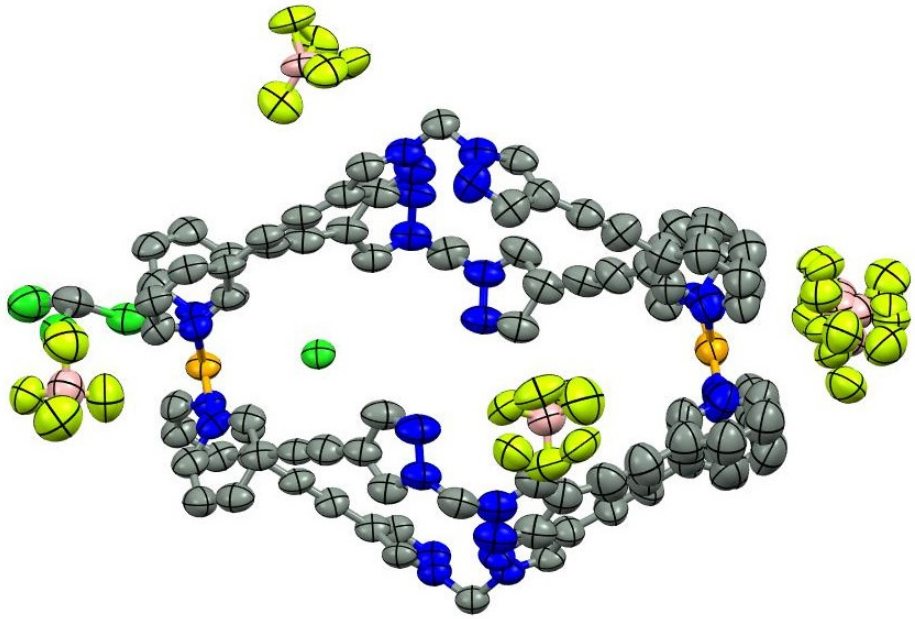

Figure S71. The asymmetric unit of the X-ray structure of Cl@**2** with all non-hydrogen atoms shown as ellipsoids at the 50% probability level.

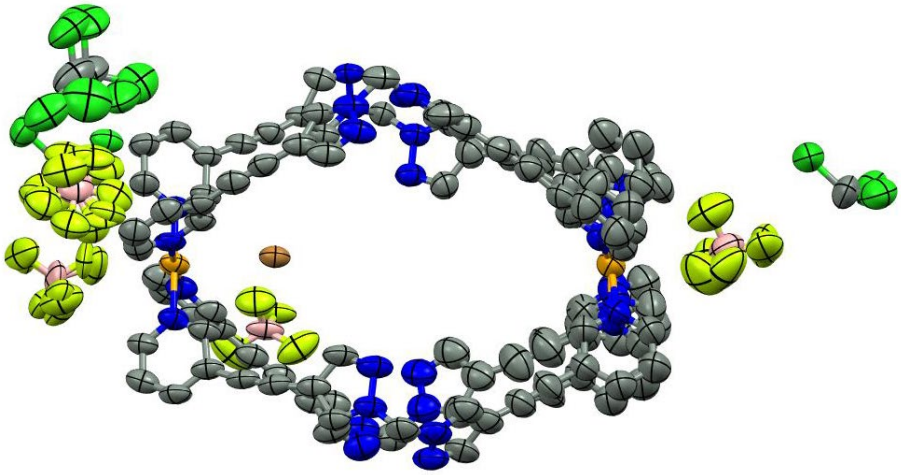

Figure S72. The asymmetric unit of the X-ray structure of Br@**2** with all non-hydrogen atoms shown as ellipsoids at the 50% probability level.

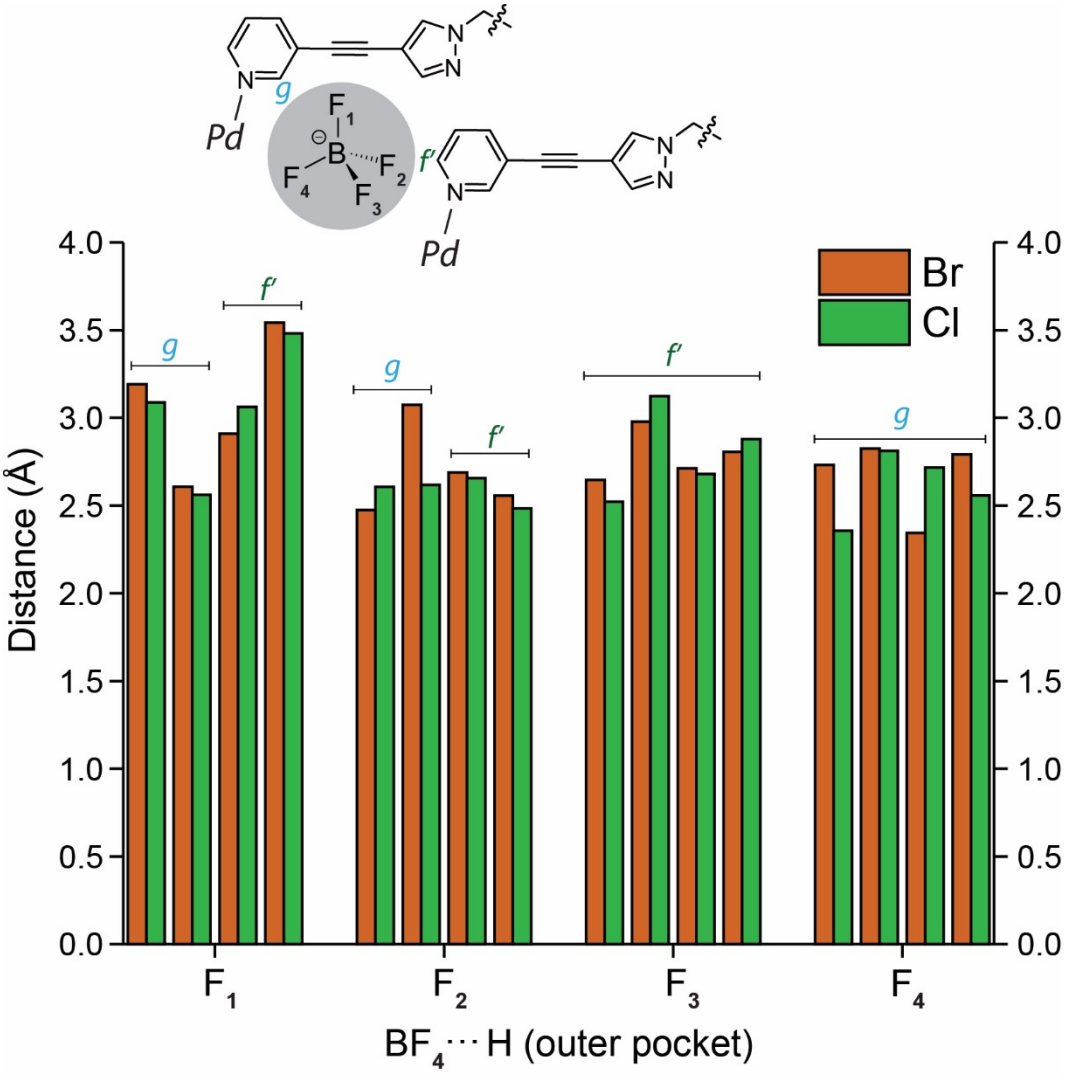

Figure S73. Cl@**2** and Br@**2** X-ray structure comparative analysis of bound BF_4^- measured distances of $F_{1\text{-}4}$ to protons g and f' (inside outer pocket). Whilst BF_4^- is oriented towards protons g and f' there is no significant difference in measured distances between each dimeric cage. Therefore, the relative BF_4^- binding strength is more dependent on ionic interactions, as dictated by the $Pd^{II}\cdots Pd^{II}$ separation.

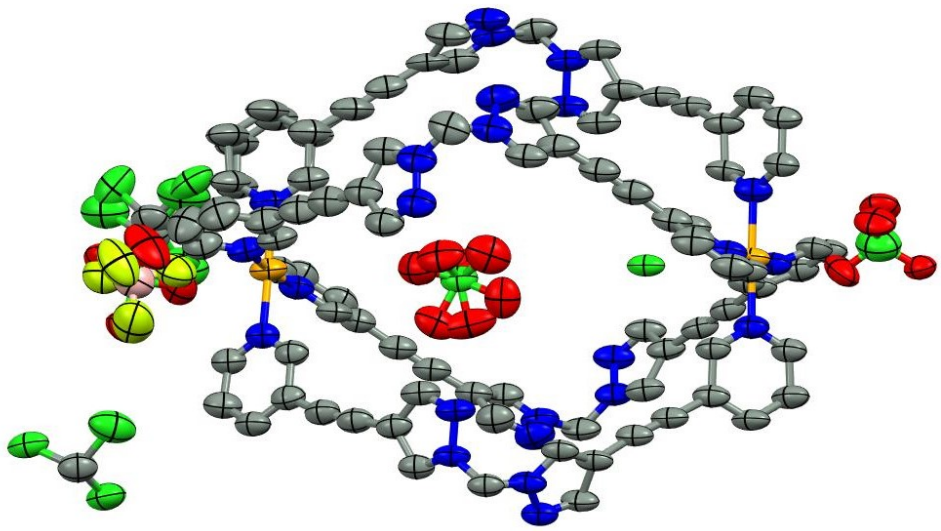

Figure S74. The asymmetric unit of the X-ray structure of $(ClO_4)_2$Cl@**2** with all non-hydrogen atoms shown as ellipsoids at the 50% probability level.

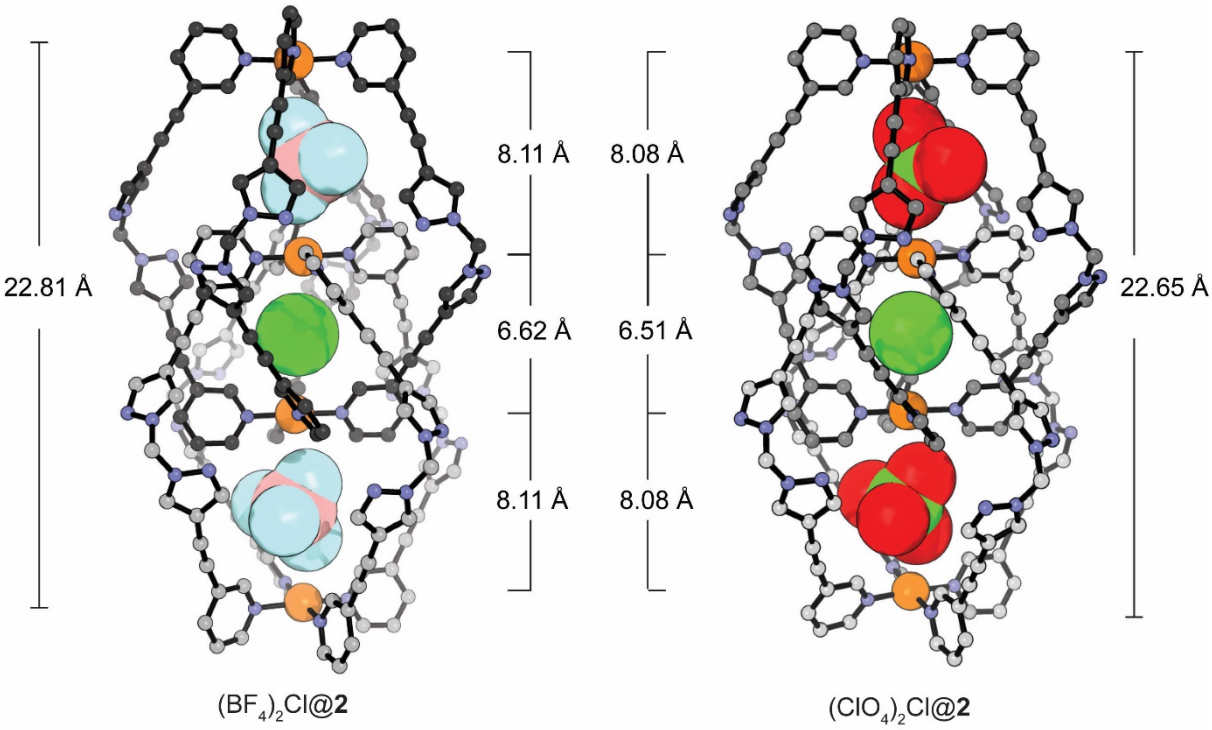

Figure S75. A comparison of the X-ray structure of Cl@**2** (left, which possesses weakly bound BF_4^- anions in the outer cavity) with the X-ray structure of $(ClO_4)_2$Cl@**2** (right). The X-ray data gives direct evidence for the 1:2 host-guest stoichiometry. Structural compression along the Pd-Pd axis can be observed, which highlights the flexibility of the bis-pyrazole ligand backbone.

4.2 Voidoo calculations

In order to determine the size of the inner cavities, VOIDOO calculations based on the crystal structure of **1** and X@**2** were performed. The calculations were performed with a 1.4 Å radius virtual probe, using default settings, apart from the maximum volume-refinement cycles set to 40. Due to the open pore apertures of **1** and X@**2**, naphthalene molecules were placed over the pores to prevent the probe from "falling out" of the inner sphere. They were placed in such a way that the van der Waals radii of their atoms touched the outermost edge of the van der Waals radii of the atoms of **1** or X@**2** lining the cavities.

Table S5. Calculated VOIDOO volumes[a] and packing coefficients for **1** and X@**2**.

Compound	Cavity	Cavity volume (Å^3)	Anion volume	Packing coefficient (BF_4^-)
1	-	596.4	54.85	9.2%
Cl@**2**	Outer	128.5	54.85	42%
	Inner	12.70	23.70	187%

Br@**2**	Outer	108.5	54.85	51%
	Inner	15.8	28.08	178%

[a] Unless otherwise stated, the volumes were obtained with a 1.4 Å probe.
[b] The volume was obtained with a 1.2 Å probe.

Table S6. Anion volumes obtained by DFT calculations (R3BLYP; B, O, F, Cl, P, S: 6-31g(d); Re: LANL2DZ.

Anion	NO_3^-	BF_4^-	ClO_4^-	HSO_4^-	ReO_4^-	$H_2PO_4^-$	PF_6^-	OTf^-
Volume Å^3	40.73	54.85	55.44	58.86	59.10	63.07	74.88	85.37

Note: anions > 60 Å^3 (e.g., $H_2PO_4^-$, PF_6^-, etc.) were not bound by X@**2**

5. References

1 P. Thordarson, *Chem. Soc. Rev.*, 2011, **40**, 1305–1323.

2 No Title, http://supramolecular.org.

3 N. P. Cowieson, D. Aragao, M. Clift, D. J. Ericsson, C. Gee, S. J. Harrop, N. Mudie, S. Panjikar, J. R. Price, A. Riboldi-Tunnicliffe, R. Williamson and T. Caradoc-Davies, *J. Synchrotron Radiat.*, 2015, **22**, 187–190.

4 D. Aragao, J. Aishima, H. Cherukuvada, R. Clarken, M. Clift, N. P. Cowieson, D. J. Ericsson, C. L. Gee, S. Macedo, N. Mudie, S. Panjikar, J. R. Price, A. Riboldi-Tunnicliffe, R. Rostan, R. Williamson and T. T. Caradoc-Davies, *J. Synchrotron Radiat.*, 2018, **25**, 885–891.

5 W. M. Bloch, J. J. Holstein, W. Hiller and G. H. Clever, *Angew. Chemie Int. Ed.*, 2017, **56**, 8285–8289.

6 M. L. Schneider, J. A. Campbell, A. D. Slattery and W. M. Bloch, *Chem. Commun.*, 2022, **58**, 12122–12125.

7 http://grade.globalphasing.org., No Title.

8 G. M. Sheldrick, *Acta Crystallogr. Sect. A*, 2015, **71**, 3–8.

9 G. M. Sheldrick, *Acta Crystallogr. Sect. C*, 2015, **71**, 3–8.

10 C. B. Hubschle, G. M. Sheldrick and B. Dittrich, *J. Appl. Crystallogr.*, 2011, **44**, 1281–1284.

11 A. Thorn, B. Dittrich and G. M. Sheldrick, *Acta Crystallogr. Sect. A*, 2012, **68**, 448–451.

12 A. Spek, *Acta Crystallogr. Sect. C*, 2015, **71**, 9–18.

13 A. Spek, *Acta Crystallogr. Sect. D*, 2009, **65**, 148–155.